

# Nonlinear light generation in disordered assemblies of nanoparticles

**Doctoral Thesis**

**Author(s):**

Morandi, Andrea

**Publication date:**

2023-01-30

**Rights / license:**

In Copyright - Non-Commercial Use Permitted

Diss. ETH No. 29074

# **Nonlinear light generation in disordered assemblies of nanoparticles**

A thesis submitted to attain the degree of

DOCTOR OF SCIENCES of ETH ZURICH  
(Dr. sc. ETH Zurich)

presented by

**Andrea Morandi**

MSc Università di Pisa, Dipartimento di fisica

born on 16.10.1993  
in Cremona, Italy

accepted on the recommendation of:

Prof. Dr. Rachel Grange, examiner  
Prof. Dr. Sylvain Gigan, co-examiner  
Prof. Dr. Frank Scheffold, co-examiner

2023



# Contents

<b>1</b>	<b>Introduction</b>	<b>7</b>
1.1	Nonlinear light generation . . . . .	7
1.2	Photonics in disordered materials . . . . .	9
1.3	Nonlinear and disordered photonics . . . . .	11
1.4	Goals of this thesis . . . . .	12
<b>2</b>	<b>Theoretical overview of light interaction with particles</b>	<b>15</b>
2.1	Scattering from a single particle . . . . .	16
2.1.1	Mie theory . . . . .	16
2.1.2	Scattering cross section . . . . .	20
2.1.3	The interaction of light with small particles . . . . .	21
2.1.4	The internal field . . . . .	22
2.2	Multiple scattering . . . . .	24
2.2.1	Diffusive regime . . . . .	25
2.2.2	Beyond diffusion . . . . .	27
2.3	Second-harmonic generation . . . . .	29
2.3.1	Phase matching . . . . .	30
2.4	Random quasi-phase-matching . . . . .	32
<b>3</b>	<b>Materials and Fabrication</b>	<b>37</b>
3.1	Lithium niobate and barium titanate . . . . .	37
3.2	Synthesis of the nanoparticles . . . . .	40
3.3	Emulsion-templated assembly . . . . .	40
3.3.1	Microspheres of BaTiO <sub>3</sub> nanoparticles . . . . .	41
3.3.2	Microspheres of LiNbO <sub>3</sub> nanocubes . . . . .	43
3.3.3	Microspheres of TiO <sub>2</sub> nanoparticles and nanodiamonds . . . . .	44
3.3.4	Spin coated nanodiamonds . . . . .	46
3.3.5	Monodisperes TiO <sub>2</sub> microspheres with microfluidics . . . . .	46
3.4	Slabs assembly . . . . .	48
3.5	Measurement of the filling fraction . . . . .	50
3.5.1	Effective refractive index with the Maxwell-Garnett mixing rule . . . . .	52
3.6	Declaration of personal contribution . . . . .	52
<b>4</b>	<b>Mie driven random quasi-phase-matching in BaTiO<sub>3</sub> microspheres</b>	<b>55</b>
4.1	State of the art . . . . .	56
4.2	Linear effective medium Mie scattering . . . . .	57
4.2.1	Analytical model and FEM simulations . . . . .	59
4.3	Nonlinear generation from the BaTiO <sub>3</sub> microspheres . . . . .	62
4.3.1	Nonlinear Speckle and polarization . . . . .	68

4.4	SHG coupled with the Mie resonances . . . . .	68
4.4.1	Efficiency comparison . . . . .	73
4.5	Summary and perspectives . . . . .	74
4.6	Declaration of personal contribution . . . . .	76
<b>5</b>	<b>Multiple scattering and random quasi-phase-matching in LiNbO<sub>3</sub> assemblies</b>	<b>77</b>
5.1	State of the art . . . . .	78
5.2	Linear scattering measurements . . . . .	79
5.3	Second-harmonic and scattering trend . . . . .	84
5.3.1	Second-harmonic in disordered LiNbO <sub>3</sub> microspheres	86
5.4	Summary and perspectives . . . . .	87
5.5	Declaration of personal contribution . . . . .	89
<b>6</b>	<b>Modulated fluorescence of nanodiamonds in bottom-up dielectric microspheres</b>	<b>91</b>
6.1	Optically active NV centers in diamond . . . . .	92
6.1.1	Single photon emission . . . . .	93
6.2	State of the art . . . . .	94
6.3	Fluorescence modulation . . . . .	96
6.4	Thermal shift of the resonances . . . . .	98
6.4.1	Lifetime measurements . . . . .	100
6.4.2	Temperature dependent lifetime . . . . .	102
6.5	Single photon emission . . . . .	103
6.6	Summary and perspectives . . . . .	106
6.7	Declaration of personal contribution . . . . .	107
<b>7</b>	<b>Conclusion and Outlook</b>	<b>109</b>
7.1	Outlook . . . . .	111
7.1.1	Disordered quantum sources . . . . .	111
7.1.2	Nonlinear generation and localization . . . . .	112
7.1.3	Nonlinear generation and wavefront shaping . . . . .	112
<b>A</b>	<b>Modeling of random quasi-phase-matching</b>	<b>113</b>
	<b>Bibliography</b>	<b>121</b>

*To Camilla, Alessandro, Annachiara e Fabio*



# Abstract

The primary source of coherent light at wavelengths not available with common laser sources are nonlinear processes such as second-harmonic generation (SHG), optical parametric oscillation (OPO), and spontaneous parametric down-conversion (SPDC). Noncentrosymmetric crystals are the conventional platform to implement optical frequency conversion. However, their use is limited by optical dispersion, which imposes strict phase-matching conditions to achieve efficient nonlinear conversion. Many methods have been developed for phase-matching control, such as phase-matching in birefringent crystals or quasi-phase-matching in periodically poled materials. These methods produce nonlinear generation that grows quadratically with the volume of the crystal. At the micro- or nanoscale it is also possible to exploit resonant mechanism to enhance the nonlinear light-matter interaction. In all these cases, the optimal nonlinear conversion is achieved in a narrow wavelength range, and it requires to control the temperature and the polarization of the pump beam as well. Disordered photonic materials, consisting of a random assembly of nonlinear optical crystals, provide an alternative platform to bulk crystals. In fact, it is possible to generate broadband coherent nonlinear light with a mechanism called random quasi-phase-matching (RQPM). It allows to circumvent the phase-matching conditions and to generate SHG proportional to the volume of the disordered material. The disadvantage of RQPM is its lower efficiency than more conventional phase-matching schemes. RQPM has been mostly implemented in polycrystals with micrometer-sized domains (10-100  $\mu\text{m}$ ). The nonlinear generation in micron-size  $\chi^{(2)}$  structures with nanostructured disorder is completely unexplored.

In this thesis we present bottom-up assembled microspheres made of nonlinear nanocrystals of barium titanate ( $\text{BaTiO}_3$ ) and lithium niobate ( $\text{LiNbO}_3$ ) as our disordered photonic material. The fabrication ensures that the nanocrystals that constitute the microspheres are randomly placed and oriented in the spherical assembly, and that the volume is known or easy to measure. Our goal is to use them to show second-harmonic generation with the RQPM at the microscale. They can achieve frequency conversion from the near-ultraviolet to the infrared ranges, are low-cost, and can cover large surface areas. Moreover, we propose different solutions to enhance the nonlinear emission from the microspheres.

In a first part, we combine the Mie resonances stemming from the spherical geometry to increase the SHG from microspheres made of  $\text{BaTiO}_3$  nanocrystals of 50 nm of size. The measured second-harmonic generation shows a combination of broadband and resonant wave mixing, in which Mie resonances enhance the second-harmonic generation, while the disorder keeps



the phase-matching conditions relaxed. We support our findings with analytical models and simulations. Our assemblies provide new opportunities for tailored phase-matching at the microscale, beyond the coherence length of the bulk crystal.

In a second part, we use  $\text{LiNbO}_3$  nanocubes of 100 nm to 400 nm as building blocks of disordered microspheres and slabs of variable thickness. Bigger domains are the most direct way to increase the efficiency of the SHG. At the same time, this introduces multiple light scattering in the assemblies. They display a remarkable strong light scattering, evidenced by a subwavelength transport mean free path ( $l^*$ ). We show that RQPM is robust to scattering and that the SHG grows linearly with the thickness of the slabs and the volume of the microspheres. These assemblies represent a promising platform to investigate the interplay between disorder and nonlinear effects.

In a third part, we bottom-up assemble spherical dielectric resonators with embedded diamond nanoparticles with nitrogen vacancy centers (NV). Those assemblies can exploit two phenomena: the photonic nanojet to focus the excitation field into a small volume, and the Mie resonances to enhance the emission at the resonant wavelength. We show that we can modulate the fluorescence thanks to the Mie modes and that we can control it with the temperature.

This work proposes bottom-up disordered assemblies of nonlinear crystals as a platform for nonlinear light generation. We illustrate the advantages of the scalable fabrication and the flexibility of the nonlinear generation from the disorder. Furthermore, we propose strategies to improve the nonlinear emission and to investigate the physics of a complex nonlinear medium.

# Sommario

La fonte principale di luce coerente a lunghezze d'onda non disponibili con le comuni sorgenti laser sono i processi non lineari come la generazione di seconda armonica (SHG), l'oscillazione parametrica ottica (OPO) e la down-conversion parametrica spontanea (SPDC). I cristalli non centrosimmetrici sono la piattaforma convenzionale per implementare la conversione ottica di frequenza. Tuttavia, il loro uso è limitato dalla dispersione ottica, che impone rigorose condizioni di phase-matching per ottenere una conversione non lineare efficiente. Sono stati sviluppati molti metodi per il controllo del phase-matching, come il phase-matching in cristalli birifrangenti o il quasi-phase-matching in materiali polarizzati periodicamente. Questi metodi producono una generazione non lineare che cresce quadraticamente con il volume del cristallo. Su scala micro o nanometrica è anche possibile sfruttare un meccanismo di risonanza per migliorare l'interazione non lineare luce-materia. In tutti questi casi, la conversione non lineare ottimale si ottiene in un intervallo di lunghezze d'onda ristretto e richiede il controllo della temperatura e della polarizzazione della luce di pompa. I materiali fotonici disordinati, costituiti da un cristalli ottici non lineari assemblati in modo casuale, forniscono una piattaforma alternativa ai cristalli monolitici. Infatti, è possibile generare luce non lineare coerente a banda larga con un meccanismo chiamato random quasi-phase matching (RQPM). Esso consente di aggirare le condizioni di phase-matching e di generare SHG proporzionalmente al volume del materiale disordinato. Lo svantaggio del RQPM è la sua minore efficienza rispetto agli schemi di phase-matching più convenzionali. Il RQPM è stata implementato principalmente in policristalli con domini di dimensioni micrometriche (10-100  $\mu\text{m}$ ). La generazione non lineare in strutture di dimensioni micrometriche con disordine nanostrutturato è, invece, completamente inesplorata.

In questa tesi presentiamo microsfere assemblate con nanocristalli non lineari di titanato di bario ( $\text{BaTiO}_3$ ) e niobato di litio ( $\text{LiNbO}_3$ ) come materiali fotonici disordinato. La fabbricazione garantisce che i nanocristalli che costituiscono le microsfere siano disposti e orientati in modo casuale nell'insieme sferico e che il volume sia noto o facilmente misurabile. Il nostro obiettivo è usarle per mostrare la generazione di seconda armonica con l'RQPM su microscala. Possono ottenere una conversione di frequenza dal vicino ultravioletto all'infrarosso, sono a basso costo e possono coprire ampie superfici. Inoltre, proponiamo diverse soluzioni per migliorare l'emissione non lineare delle microsfere.

In una prima parte, combiniamo le risonanze Mie derivanti dalla geometria sferica per aumentare la SHG da microsfere fatte di nanocristalli di  $\text{BaTiO}_3$  di 50 nm di dimensione. La generazione di seconde armoniche misurata mostra

una combinazione di generazione a banda larga e risonanti, in cui le risonanze di Mie aumentano la generazione di seconde armoniche, mentre il disordine mantiene rilassate le condizioni di phase-matching. I nostri risultati sono supportati da modelli analitici e simulazioni. I nostri assemblaggi offrono nuove opportunità per phase-matching adattabile su microscala, oltre la lunghezza di coerenza del puro cristallo.

In una seconda parte, utilizziamo nanocubi di  $\text{LiNbO}_3$  da 100 a 400 nm come elementi costitutivi di microsfer e lastre disordinate di spessore variabile. I domini più grandi sono il modo più diretto per aumentare l'efficienza della SHG. Allo stesso tempo, questo introduce uno scattering multipla della luce negli assemblaggi. Essi mostrano una notevole diffusione della luce, evidenziata da un percorso libero medio di trasporto ( $l^*$ ) inferiore alla lunghezza d'onda. Dimostriamo che il RQPM non è soppresso dalla diffusione della luce e che la SHG cresce linearmente con lo spessore delle lastre e il volume delle microsfer. Questi materiali rappresentano una piattaforma promettente per studiare l'interazione tra disordine ed effetti non lineari.

In una terza parte, abbiamo assemblato risuonatori dielettrici sferici di diossido di titanio con nanoparticelle di diamante. Questi nanodiamanti sono fluorescenti poiché presentano centri di vacanza di azoto (NV) che possono essere utilizzati come biomarker o generatori di single photons. Queste microsfer possono sfruttare due fenomeni: il photonic nanojet per focalizzare il campo di eccitazione in un piccolo volume e le risonanze di Mie per aumentare l'emissione alla lunghezza d'onda risonante. Dimostriamo che possiamo modulare la fluorescenza grazie ai modi Mie e che possiamo controllarla con la temperatura.

Questo lavoro propone assemblaggi disordinati bottom-up di cristalli non lineari come piattaforma per la generazione di luce non lineare. Illustriamo i vantaggi della fabbricazione scalabile e della flessibilità della generazione non lineare dal disordine. Inoltre, proponiamo strategie per migliorare l'emissione non lineare e per studiare la fisica di un mezzo non lineare complesso.

# Chapter 1

## Introduction

The beginning of the field of nonlinear optics is usually considered the discovery of the second-harmonic generation from Franken *et al.* in 1961 [1], right after the invention of the laser by Maiman *et al.* in 1960 [2]. In their seminal work, the red light from a ruby laser was frequency doubled to ultraviolet light passing through a quartz crystal. However, there was evidence of optical nonlinearities dating back to 1896 with the discovery of the Pockels effect [3], which consists in the change of the refractive index of a material when an external electric field is applied. Another remarkable example was the prediction of two-photon absorption in 1931 [4]. Nonetheless, it is clear that the field of nonlinear optics gained relevance when the high intensity of the laser sources became available in the 60s. Since then, nonlinear optics has played a key role in the development of laser technology. A nonlinear optical element combined with a laser allowed to change the wavelength of the generated light with processes such as second-harmonic generation or optical parametric oscillation, or to modify the spatial and temporal properties of the light with Q-switching and mode locking [5]. Nonlinear optics has also fundamental applications in a variety of different fields such as telecommunication, sensors, bioimaging and quantum technologies [6]. In particular second-harmonic generation is relevant for ultra-short pulse measurements, SHG microscopy and the characterization of materials. Moreover, spontaneous parametric down-conversion (SPDC), which is its inverse process, is nowadays one of the key phenomenon to generate entangled photon pairs and single photons, which are the backbone of optical quantum technologies [7], [8].

### 1.1 Nonlinear light generation

Optical nonlinearities can be found in many different materials such as crystals, amorphous materials, polymers, liquids or organic compounds. One of the main platforms is constituted by noncentrosymmetric crystals, which have a non zero second-order nonlinear susceptibility  $\chi^{(2)}$  [9]. Many properties of a nonlinear material can be relevant for applications such as the magnitude of the coefficient of the  $\chi^{(2)}$  tensor, that regulates the strength of the nonlinear interaction, the chromatic dispersion and the birefringence properties, that determine the phase-matching bandwidth, and the transparency

window. For these listed criteria barium titanate ( $\text{BaTiO}_3$ ) and lithium niobate ( $\text{LiNbO}_3$ ) have attracted a lot of interest. They display strong nonlinearities, a wide transparency window from the near ultra violet to the infrared and a high chemical robustness. More information on their properties are given in Chapter 3. Their application for SHG and SPDC is limited by the phase-matching conditions which means that a proper phase relationship between the pump and the generated light has to be maintained in the crystal to achieve optimal nonlinear generation. Otherwise, the signal generated in the crystal may interfere destructively during propagation, causing little or no emission. Phase-matching can be obtained with different techniques. One of the most widely used is phase-matching in birefringent crystals, achieved by positioning the crystal at a specific angle to the pump beam. The different refractive indices and the optical dispersion can compensate to achieve the optimal phase relation between the pump and the generated light. Depending on the pump wavelength, the specific crystal structure and refractive index there can be cases in which no angle fulfills the phase-matching conditions. Moreover, this process works for a specific polarization and also the temperature of the material has to be kept constant. Another widespread technique is the quasi-phase-matching in which the crystal is engineered to periodically reverse its crystal structure to compensate the phase mismatch given by the optical dispersion. There are several techniques to implement this periodic poling, such as pulsed electric field, electron bombardment and thermal pulsing [10]. Quasi-phase-matching has the advantage that it can be implemented for essentially any nonlinear process within the transparency window of the crystal. In waveguides the refractive index depends on the mode of the propagation, therefore for nonlinear generation modal phase-matching has to be imposed. This means that the waveguides have to be engineered such that the fundamental mode and the generated mode respect the correct phase relationship. All of the above mentioned techniques can lead to efficient nonlinear conversion, the common drawback that they share is that they operate at narrow bandwidth. If we want to change the wavelength of operation we have to reorient the crystal to a specific angle for perfect phase-matching or change the temperature and the polarization of the pump light. While modal and quasi-phase-matching are not usable for broadband or tunable applications. Moreover, the robustness of the nonlinear generation is limited, because a small variation in the experimental conditions (for example in the incident angle or fabrication imperfection in the waveguide or in the period of the poled crystal) will result in big variation of the generated field. So far, the optimal conversion in nonlinear crystals has been obtained by controlling carefully many properties of the system, from the crystal structure, to the orientation, to the polarization of the pump beam, or the precise patterning of the device. All of these approaches rely in a broad sense to the concept of order and we have seen that small imperfection on the system can heavily affect the nonlinear emission. A possible route to overcome these limitations can be found increasing the complexity of the nonlinear crystal structure [11]. Other possibilities open up if we loosen the order of the system and insert some disorder. In this case, we

can replace the non-linear crystal with a disordered assembly of non-linear nanocrystals. By disorder, we mean that their size, position and orientation are random. What can be the advantages of using such a material? We need to introduce the field of disordered photonics here, and then we will show how the cross-fertilization of non-linear optics with disorder can be fruitful for the generation of nonlinear light.

## 1.2 Photonics in disordered materials

In the field of photonics, the most recurrent manifestation of disorder is light scattering. The scattering of electromagnetic waves stems from the heterogeneity of the system that interacts with the light [12]. Scattering is responsible for many optical phenomena that we see every day. The blue color of the sky is the result of the Rayleigh scattering of the light of the sun by the atmosphere, and the white color of a cloud on a summer day is the result of the multiple scattering of the light [13]. Disorder in science is most often considered undesirable and avoided. However, there is a host of interesting phenomena happening in a disordered photonic material [14]. First of all, the light that is multiply scattered in a material interferes with itself but does not lose any information. It is only scrambled into a "speckle pattern" [15], that is a granular texture of bright and dark spots. This pattern is the result of the interference of the light in the disordered material and can be seen, for example, if we shine light from a coherent source onto a white wall. In principle it is possible to descramble the speckle to retrieve some information of the propagating beam or to focus the light into a specific target [16], [17]. This concept can be applied to imaging through the fog or across a white marble wall [18], or to do bioimaging through skin or bones [19], or to focus the light on a specific spot in depth in the tissue [20]. It is also known that many colors that can be seen in nature in birds or insects, arise from the light interaction with disordered or partially ordered structures [21], [22]. Another famous application of disorder in photonics is the random laser [23], in which the cavity of the lasing system is replaced with a multiple scattering material. The emission of such a system is also surprisingly coherent and shows narrow spikes in the emission spectra [24]. There is also a lot of interesting physics in the properties of the light propagation in a disordered material. One famous example is constituted by light localization. When the strength of a scattering material is particularly intense it is possible that the light stays trapped in the material and it is not able to diffuse out of it. This concept, known as Anderson localization for light [25], [26], has been shown in 1D and 2D structures [27], while its demonstration in 3D is still a debated topic in the field [28][29].

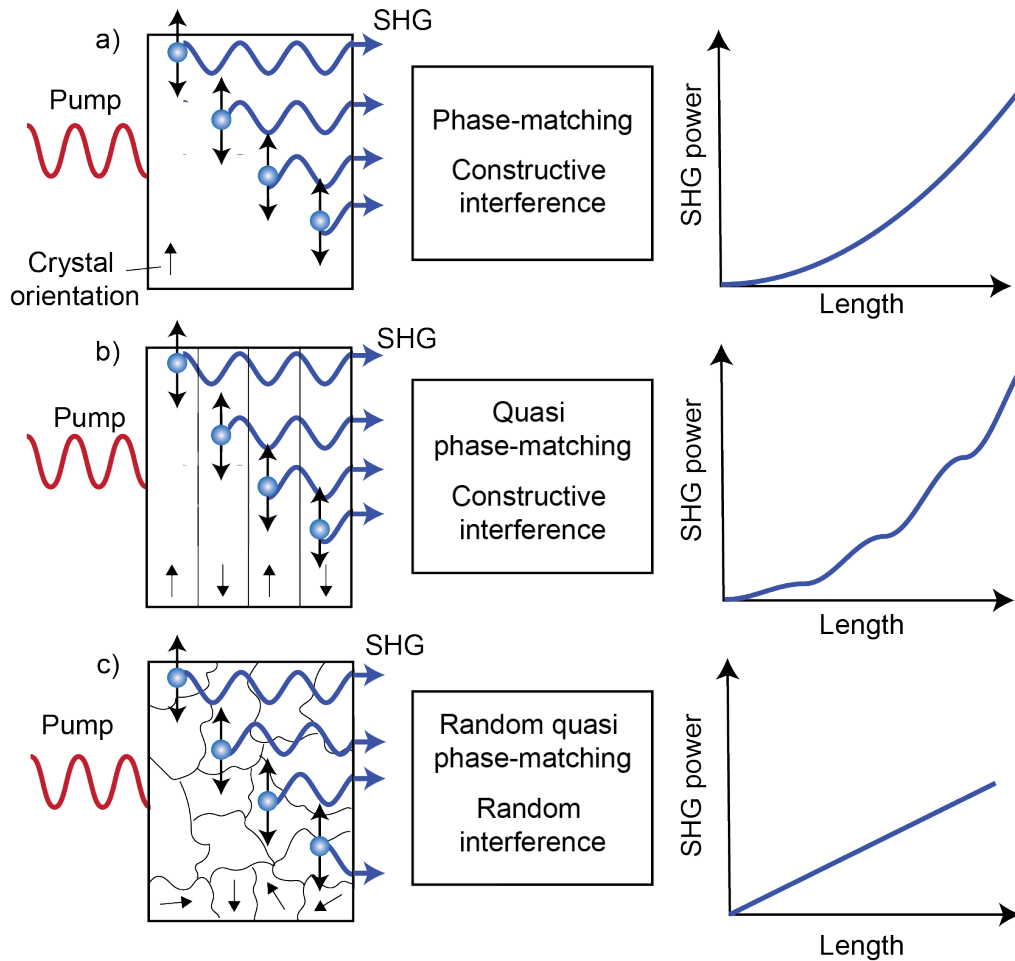


FIGURE 1.1: Phase-matching schemes. A fundamental beam impinges on nonlinear crystal and produces SHG as it proceeds in the material. a) The material is a phase-matched single crystal: the SHG adds up in phase resulting in a signal that scales quadratically with the sample length or the number of domains. b) The material is quasi-phase-matched crystal, in which the orientation is periodically reversed to maintain the correct phase relation, and the SHG grows again with the square of the length. c) The material is a disordered polycrystal, the SHG interferes with a random phase leading to a linear growth with the length.

## 1.3 Nonlinear and disordered photonics

All the phenomena described in the previous section are the result of the light interacting with a material which is heterogeneous in the linear refractive index. Typical examples are the suspended particles that form a cloud or a complex system composed by a mixture of two materials of different refractive indices. However, if the particles in the disordered material have also a second-order nonlinear susceptibility ( $\chi^{(2)}$ ) this allows for the combination of nonlinear generation and disorder. We refer to a material constituted by a collection of nonlinear crystalline domains that are randomly oriented and polydispersed in size as a nonlinear disordered photonic material (NDPM). Under illumination with a pump beam each domain produces SHG. The global signal generated by the NDPM is the result of the interference of the light generated by each domain. Counter-intuitively, the interference does not destruct the signal. On the contrary, it generates a signal that scales linearly with the number of domains of the NDPM. This approach is called random quasi-phase-matching (RQPM) since it relies on the random orientation of the domains rather than their order. This process is less efficient than the SHG obtained through phase-matching or quasi-phase-matching for which the converted SHG scales quadratically with the number of domains, as it is sketched in Fig. 1.1. However, the RQPM has the great advantages of being completely broadband, circumventing the phase-matching conditions. It works for every polarization of the impinging beam, every temperature, and every angle of incidence. Moreover it is robust to imperfections since it does not require precise orientation or size of single parts. Similarly to the light that is multiply scattered, the global SHG comes from the interference of all the sources in the material. Therefore, it is a nonlinear speckle, with bright spots where the interference is more constructive and dark spot where the interference is more destructive. The basic physics of linear and nonlinear speckles is discussed in Chapter 2.

The combination of nonlinear optical properties with disordered material is still an under-explored field. It has been shown that with wavefront shaping it is possible to manipulate the nonlinear speckle after a disordered material made of grains of  $\text{LiNbO}_3$  [30]. The light trapped in a multiple scattered material can exploit disordered modes to enhance the nonlinear emission (similarly to a random laser but for SHG) [31]. The properties of linear and nonlinear speckle [32], [33], or its polar dependence [34], have been studied to understand some properties of the light propagation [35]. A promising route is represented by optical computing. Optical computing has already benefited from the linear disordered photonics to implement some algorithms [36]. They exploited the fact that light propagating in a scattering material can be used to compute matrix multiplication at the speed of light. The possibilities offered by nonlinearity, which could implement more complex calculations, have only recently been studied [37], [38]. However, the potential of nonlinear disordered photonic material is still unrealized.

Random quasi-phase-matching has been so far employed mostly in disordered polycrystals with domains of several tens of micron [39]. They have



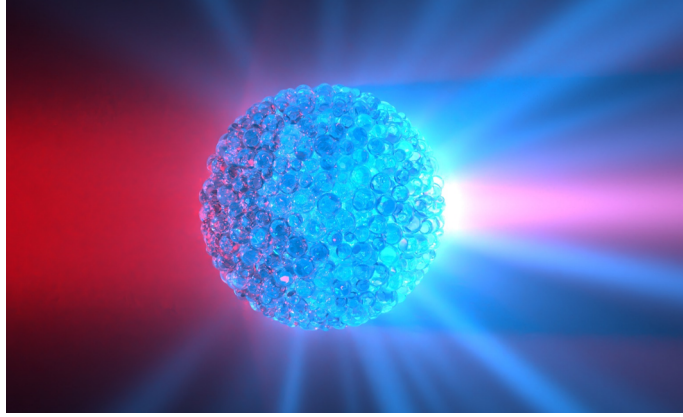


FIGURE 1.2: Sketch of a disordered assembled microspheres illuminated with a pump beam that generates second-harmonic light. Image by J. Müller.

been used to implement mode-locked lasers [40], and optical parametric oscillators [41] in millimeter-sized devices. The aspect that we investigate in this thesis is the use of noncentrosymmetric crystalline nanodomains to assemble micro-disordered structures with a controlled geometry. We fabricate well-shape microspheres that are composed by a disordered distribution of nonlinear nanoparticles. We employ a bottom-up method that allows to control directly the domain size distribution and the volume of the assembly.

## 1.4 Goals of this thesis

In this work, we propose nonlinear and disordered material fabricated with bottom-up technique as a platform for nonlinear optical generation (see sketch in Fig. 1.2). The material chosen are barium titanate ( $\text{BaTiO}_3$ ) and lithium niobate ( $\text{LiNbO}_3$ ). Their properties and the fabrication used are presented in Chapter 3. The goal of this thesis is to demonstrate possible routes to increase the efficiency of the second-harmonic generation via random quasi-phase-matching. In Chapter 4 we show how it is possible to combine the nonlinear generation through the disorder with optical Mie resonances. We do that by implementing random quasi-phase-matching in Mie resonant spheres made by bottom-up assembly of  $\text{BaTiO}_3$  nanoparticles. In Chapter 5 we combine RQPM with multiple scattering in assemblies of  $\text{LiNbO}_3$  nanocubes. We show that the SHG grows linearly with the number of domains, even in the presence of strong scattering and in different geometries. These  $\text{LiNbO}_3$  NDPM present strong nonlinearity and scattering that can be used to further study the interplay of nonlinear generation and disorder. In Chapter 5 we study the fluorescence properties of nitrogen vacancy (NV) centers of diamond assembled in  $\text{TiO}_2$  microspheres. The idea is to exploit the Mie modes of the spheres to enhance the generation of photons from the assemblies.

A broader scope of this work is to illustrate that disordered nonlinear materials based on  $\text{BaTiO}_3$  and  $\text{LiNbO}_3$  and assembled with bottom-up techniques are a promising platform for nonlinear light generation. We pinpoint some of the goals of this thesis:

- show that the fabrication through emulsion-templated assembly is a robust and scalable way to manufacture resonant microstructures with different materials;
- give evidence of the broadband second-harmonic generation that can be achieved via random quasi-phase-matching;
- show that the efficiency of RQPM SHG can be enhanced with the Mie modes of the resonators. Consequently that it is possible to couple a nonlinear signal coming from disorder with a resonance due to the spherical shape;
- prove that the power of the SHG with random quasi-phase-matching scales linearly with the volume of the assembly. This happens both for transparent and resonant spheres and for multiple scattering materials;
- show that  $\text{LiNbO}_3$  assemblies of nanocubes are a strongly scattering and nonlinear material that can be used to further study the combination of SHG with disorder;
- give evidence that the Mie resonances from the assembled microspheres can drive the emission from active materials such as NV centers.



## Chapter 2

# Theoretical overview of light interaction with particles

In this chapter we present the theory of the light interaction with particles. We focus first on the linear scattering of light by a spherical object, a problem that was solved analytically in the early years of the 20<sup>th</sup> century by the German physicist Gustav Mie<sup>1</sup>[42]. We summarize the key aspects of his derivation and we review two useful applications: the calculation of the scattering cross section and of the internal electric field. We also show that, when the particle is much smaller than the wavelength of the impinging light, the solution converges to the Rayleigh scattering<sup>2</sup>[43][13].

Afterwards, we extend the concepts from single scattering to the interaction of light with an ensemble of scatterers, which are usually referred to as turbid or opaque media. In such an environment the light does not propagate as a straight ray but rather is deflected many times by the particles. We discuss how the scattering strength of a material is characterized and define the measured quantities that are used in the context of the diffusion approximation. This theory has certain limitations, we discuss them briefly and we introduce the concept of localization.

In the final part of the chapter, we present the basis of the light interaction with nonlinear media focusing our attention on the nonlinear light generation. We introduce the  $\chi^{(2)}$  tensor and present the equations that describe the second-harmonic generation. We then discuss the concept of coherence length and how the phase-matching conditions can be met with the perfect phase-matching and quasi phase-matching scheme. In the last section, we present how a disordered distribution of crystals can be exploited to generate second harmonic. This mechanism is called random quasi-phase matching. We explain its working principle and specify its advantages and disadvantages compared to the more conventional phase-matching schemes.

---

<sup>1</sup>The original publication from 1908 can be found in the *Annalen der Physik* with the title: “*Beiträge zur Optik trüber Medien speziell kolloidaler Goldlösungen*” (“*Contributions to the optics of turbid media, particularly of colloidal metal solutions*”)

<sup>2</sup>Named after Lord Rayleigh, author of the two founding works at the end of the XIX century “*On the electromagnetic theory of light*” and “*On the transmission of light through an atmosphere containing small particles in suspension, and on the origin of the blue of the sky*”.

## 2.1 Scattering from a single particle

When light impinges on objects much bigger than its wavelength, the interaction can be explained using ray optics. This means that the physics of the ray of light can be described in terms of reflection, refraction and transmission. In particular, the direction and intensity of the light can be derived through the Fresnel coefficients [12]. When the light impinges on structures with features of sizes comparable to its wavelength or smaller, these concepts are inapplicable. The light-matter interaction at the nano- or micro scale is described by the concepts of scattering and absorption.

### 2.1.1 Mie theory

In 1908 Mie solved the problem of absorption and scattering of a plane wave impinging on a sphere of arbitrary radius and refractive index immersed in an homogeneous medium. This theory also provides a good first-order approximation for small non-spherical particles. It consists of the explicit calculation of the solution of Maxwell's equations (see Eq. (2.1)) in every point of the space inside and outside the sphere [44].

$$\begin{aligned}
 \nabla \cdot \mathbf{E} &= 0, \\
 \nabla \cdot \mathbf{H} &= 0, \\
 \nabla \times \mathbf{E} &= i\omega\mu\mathbf{H}, \\
 \nabla \times \mathbf{H} &= -i\omega\varepsilon\mathbf{E},
 \end{aligned} \tag{2.1}$$

Where  $\mathbf{E}$  and  $\mathbf{H}$  are the electric and magnetic field,  $\omega$  is the angular frequency of oscillation of the field.  $\mu$  and  $\varepsilon$  are the permeability and the permittivity of the medium in which the electromagnetic wave is propagating. Since the space is homogeneous, we can recast the Maxwell's equation in the form of two wave equations for the electric and magnetic field. They are valid both in the space inside the sphere and outside (Eq. (2.2))

$$\nabla^2\mathbf{E} + k^2\mathbf{E} = 0, \quad \nabla^2\mathbf{H} + k^2\mathbf{H} = 0 \tag{2.2}$$

where  $k$  is the wavevector. The solution to the problem can be found by imposing the following boundary conditions on the air-sphere interface:

$$\begin{aligned}
 [\mathbf{E}_2(\mathbf{r}) - \mathbf{E}_1(\mathbf{r})] \times \hat{\mathbf{n}} &= 0, \\
 [\mathbf{H}_2(\mathbf{r}) - \mathbf{H}_1(\mathbf{r})] \times \hat{\mathbf{n}} &= 0,
 \end{aligned} \tag{2.3}$$

Next, we present a brief summary of the calculation of Mie. Further details and examples are given in Chapter 4 of the book from Craig F. Bohren "Absorption and scattering of light by small particles" [12]. As depicted in Fig. 2.1,  $(\mathbf{E}_1, \mathbf{H}_1)$  refer to the fields inside the sphere and  $(\mathbf{E}_2, \mathbf{H}_2)$  for the fields in the surrounding medium, which are the superposition of the incident fields

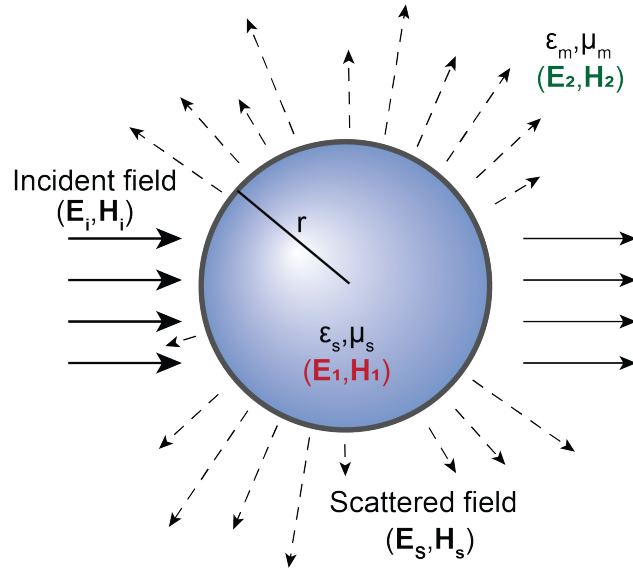


FIGURE 2.1: Sketch of a sphere with permittivity  $\epsilon_s$  and permeability  $\mu_s$  in a uniform medium  $(\epsilon_m, \mu_m)$  interacting with a plane wave. The field inside the sphere is  $(\mathbf{E}_1, \mathbf{H}_1)$  and outside is  $(\mathbf{E}_2, \mathbf{H}_2)$ .

$(\mathbf{E}_s, \mathbf{H}_s)$  and the scattered fields  $(\mathbf{E}_i, \mathbf{H}_i)$ . Two important quantities are the *size parameter*  $x$  and the *relative refractive index*  $m$ :

$$x = ka = \frac{2\pi Na}{\lambda}, \quad m = \frac{k_1}{k} = \frac{N_1}{N} \quad (2.4)$$

where  $a$  is the sphere radius and  $N_1$  and  $N$  are the refractive indices of the particle and the medium, respectively. It can be shown that if the scalar function  $\psi$  is a solution of the scalar wave equation:

$$\nabla^2 \psi + k^2 \psi = 0. \quad (2.5)$$

Then, the two vectors defined by Eq. (2.6)

$$\begin{aligned} \mathbf{M} &= \nabla \times (\mathbf{r}\psi), \\ \mathbf{N} &= \frac{\nabla \times \mathbf{M}}{k}, \end{aligned} \quad (2.6)$$

are a solution of the wave equation. Therefore, we can solve the scalar wave equation for  $\psi$  and substitute the solution in Eq. (2.6). The electric and magnetic field will be a combination of  $\mathbf{M}$  and  $\mathbf{N}$  with the appropriate weights. To compute the weights we have to decompose the impinging plane wave in spherical harmonics. We retrieve the coefficients by applying the boundary conditions at the surface of the sphere.

$$\nabla^2 = \frac{1}{r^2} \frac{\partial}{\partial r} \left( r^2 \frac{\partial}{\partial r} \right) + \frac{1}{r^2 \sin \theta} \frac{\partial}{\partial \theta} \left( \sin \theta \frac{\partial}{\partial \theta} \right) + \frac{1}{r^2 \sin \theta} \frac{\partial^2}{\partial \phi^2} \quad (2.7)$$

We look for solutions  $\psi(r, \theta, \phi) = R(r)\Theta(\theta)\Phi(\phi)$  for Eq. (2.5) that are the product of three scalar functions. We insert  $\psi(r, \theta, \phi)$  in Eq. (2.5) and we use Eq. (2.7). We obtain three separate equations  $r, \theta$  and  $\phi$ :

$$\frac{d^2\Phi}{d\phi^2} + m^2\Phi = 0, \quad (2.8)$$

$$\frac{1}{\sin\theta} \frac{d}{d\theta} \left( \sin\theta \frac{d\Theta}{d\theta} \right) + \left[ n(n+1) - \frac{m^2}{\sin^2\theta} \right] \Theta = 0, \quad (2.9)$$

$$\frac{d}{dr} \left( r^2 \frac{dR}{dr} \right) + \left[ k^2 r^2 - n(n+1) \right] R = 0. \quad (2.10)$$

These give for  $\psi$  the following form:

$$\begin{aligned} \psi_{emn} &= \cos(m\phi) P_n^m(\cos\theta) z_n(kr), \\ \psi_{omn} &= \sin(m\phi) P_n^m(\cos\theta) z_n(kr), \end{aligned} \quad (2.11)$$

where  $m$  and  $n$  are integers,  $e$  and  $o$  indicate the even or odd solutions and  $P_n^m$  and  $z_n$  are the Legendre functions of the first kind and the Bessel functions. With this, we can compute  $\mathbf{M}_{emn}, \mathbf{M}_{omn}, \mathbf{N}_{emn}$  and  $\mathbf{N}_{omn}$ .

$$\begin{aligned} \mathbf{M}_{emn} &= \frac{-m}{\sin(\theta)} \sin(m\phi) P_n^m(\cos\theta) z_n(kr) \mathbf{e}_\theta \\ &\quad - \cos(m\phi) \frac{dP_n^m(\cos\theta)}{d\theta} z_n(kr) \mathbf{e}_\phi, \end{aligned} \quad (2.12)$$

$$\begin{aligned} \mathbf{M}_{omn} &= \frac{m}{\sin(\theta)} \cos(m\phi) P_n^m(\cos\theta) z_n(kr) \mathbf{e}_\theta \\ &\quad - \sin(m\phi) \frac{dP_n^m(\cos\theta)}{d\theta} z_n(kr) \mathbf{e}_\phi, \end{aligned} \quad (2.13)$$

$$\begin{aligned} \mathbf{N}_{emn} &= \frac{z_n(kr)}{kr} \cos(m\phi) n(n+1) P_n^m(\cos\theta) \mathbf{e}_r \\ &\quad + \cos(m\phi) \frac{dP_n^m(\cos\theta)}{d\theta} \frac{1}{kr} \frac{d}{d(kr)} \left[ (kr) z_n(kr) \right] \mathbf{e}_\theta \\ &\quad - m \sin(m\phi) \frac{P_n^m(\cos\theta)}{\sin(\theta)} \frac{1}{kr} \frac{d}{d(kr)} \left[ (kr) z_n(kr) \right] \mathbf{e}_\phi, \end{aligned} \quad (2.14)$$

$$\begin{aligned}
\mathbf{N}_{omn} = & \frac{z_n(kr)}{kr} \sin(m\phi) n(n+1) P_n^m(\cos\theta) \mathbf{e}_r \\
& + \sin(m\phi) \frac{dP_n^m(\cos\theta)}{d\theta} \frac{1}{kr} \frac{d}{d(kr)} \left[ (kr) z_n(kr) \right] \mathbf{e}_\theta \\
& + m \cos(m\phi) \frac{P_n^m(\cos\theta)}{\sin(\theta)} \frac{1}{kr} \frac{d}{d(kr)} \left[ (kr) z_n(kr) \right] \mathbf{e}_\phi,
\end{aligned} \tag{2.15}$$

The electromagnetic field inside the sphere and scattered outside can be found as a series of these vectors.

$$\begin{aligned}
\mathbf{E}_1 = & \sum_{n=1}^{\infty} i^n E_0 \frac{2n+1}{n(n+1)} \left( c_n \mathbf{M}_{o1n}^{(1)} - i d_n \mathbf{N}_{e1n}^{(1)} \right), \\
\mathbf{H}_1 = & -\frac{k_s}{\omega \mu_s} \sum_{n=1}^{\infty} i^n E_0 \frac{2n+1}{n(n+1)} \left( d_n \mathbf{M}_{e1n}^{(1)} + i c_n \mathbf{N}_{o1n}^{(1)} \right).
\end{aligned} \tag{2.16}$$

$$\begin{aligned}
\mathbf{E}_s = & \sum_{n=1}^{\infty} i^n E_0 \frac{2n+1}{n(n+1)} \left( i a_n \mathbf{N}_{e1n}^{(3)} - b_n \mathbf{M}_{o1n}^{(3)} \right), \\
\mathbf{H}_s = & \frac{k_m}{\omega \mu_m} \sum_{n=1}^{\infty} i^n E_0 \frac{2n+1}{n(n+1)} \left( i b_n \mathbf{N}_{o1n}^{(3)} + a_n \mathbf{M}_{e1n}^{(3)} \right).
\end{aligned} \tag{2.17}$$

Where the coefficients  $a_n, b_n, c_n, d_n$  are:

$$c_n = \frac{\mu_1 j_n(x) [x h_n^{(1)}(x)]' - \mu_1 h_n^{(1)}(x) [x j_n(x)]'}{\mu_1 j_n(mx) [x h_n^{(1)}(x)]' - \mu_1 h_n^{(1)}(x) [m x j_n(mx)]'} \tag{2.18}$$

$$d_n = \frac{\mu_1 m j_n(x) [x h_n^{(1)}(x)]' - \mu_1 m h_n^{(1)}(x) [x j_n(x)]'}{m^2 j_n(mx) [x h_n^{(1)}(x)]' - \mu_1 h_n^{(1)}(x) [m x j_n(mx)]'} \tag{2.19}$$

$$a_n = \frac{m^2 j_n(mx) [x j_n(x)]' - \mu_1 j_n(x) [m x j_n(mx)]'}{m^2 j_n(mx) [x h_n^{(1)}(x)]' - \mu_1 h_n^{(1)}(x) [m x j_n(mx)]'} \tag{2.20}$$

$$b_n = \frac{\mu_1 j_n(mx) [x j_n(x)]' - j_n(x) [m x j_n(mx)]'}{\mu_1 j_n(mx) [x h_n^{(1)}(x)]' - h_n^{(1)}(x) [m x j_n(mx)]'} \tag{2.21}$$

It can be noted that the solution of the problem is expressed solely in function of the size parameter and the relative refractive index that that we have previously defined in Eq. 2.4. This means that, when we discuss scattering from a spherical object, a duality exists between the wavelength of the



impinging beam and the radius of the sphere. Increasing the wavelength or decreasing the size of the sphere have the same effect on the calculation of the fields. Alternatively, doubling both  $\lambda$  and  $a$  does not affect the result of the calculation (in the assumption that the refractive index does not depend on  $\lambda$ , which is not true in most cases)<sup>3</sup>. At this point, the calculation of the fields is complete. There is a nice quote from Bohren: *“The reader who has painstakingly followed this derivation, and thereby acquired virtue through suffering, may derive some comfort from the knowledge that it is relatively clear sailing from here on.”* Indeed after having derived the coefficients  $a_n, b_n, c_n, d_n$  and the vectors  $\mathbf{M}_{emn}, \mathbf{M}_{omn}, \mathbf{N}_{emn}$  and  $\mathbf{N}_{omn}$ , the calculation is straightforward and it is just a matter of computing power, and of deciding where to stop the series. This is clearer when applied to practical examples as it is done in the next sections.

## 2.1.2 Scattering cross section

The scattering cross section of a single particle is

$$\sigma_s = \int_{4\pi} |S(u)|^2 d\Omega \quad Q_s = \frac{\sigma_s}{\pi a^2} \quad (2.22)$$

where  $S(u)$  represents the Poynting vector,  $\Omega$  is the solid angle and  $Q_s$  is the scattering cross section normalized by the physical cross section of the sphere. When light undergoes a scattering event with a sphere of radius  $a$ , the interaction can be described in terms of cross section  $Q$  normalized to the physical cross section of the sphere  $\pi a^2$ . If the scattering is elastic (i.e. energy conservation holds) then we have that the extinction of the impinging beam is given by the sum of the absorption and the scattering.

$$Q_{ext} = Q_{sca} + Q_{abs} \quad (2.23)$$

In the case of negligible absorption, the extinction (which represents the amount of energy that is removed from the original beam), coincides with the scattering cross section. The scattering cross section can be computed from Mie theory with the following formula:

$$Q_{sca} = \frac{2}{x^2} \sum_{n=1}^{\infty} (2n+1) (|a_n|^2 + |b_n|^2) \quad (2.24)$$

We can calculate Eq. 2.24 directly with a MATLAB code<sup>4</sup>.

We compute  $Q_{sca}$  for a sphere of radius 200 nm with a refractive index of 2.3 in a medium of refractive index 1 (air) for different wavelengths of the impinging light. The peaks that are visible in the plot in Fig. 2.2 are a consequence of the Mie resonances in the sphere: the electric dipole, the magnetic

<sup>3</sup>The refractive index is in principle also dependent on the size of the nanoparticle. However, in most cases the bulk value of the material is taken, since practically it can be very hard to measure accurately the refractive index of a single nanoparticle.

<sup>4</sup>This code was written together with Jolanda Müller extending an original code from C. Mätzler [45]. The code is available publicly on GitHub at this link: <https://github.com/Nayunis/MieEfield>.

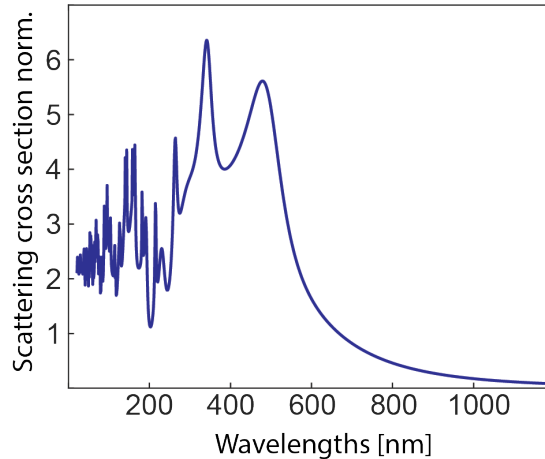


FIGURE 2.2: Scattering cross section computed for a sphere of radius 200 nm and a refractive index 2.3. The plot is generated computing explicitly the Eq. 2.24. This plot and the following ones are obtained with the code which is an extension to the code originally developed by C. Mätzler *et al.*[45].

dipole, the electric quadrupole etc... We can see also that the scattering is stronger when  $\lambda \approx nr$ , which is the usual rule of thumb that is given to identify the regime of “Mie scattering”. For shorter wavelengths the  $Q_{sca}$  presents some oscillations which tend roughly to the value of 2. This phenomenon is called the *extinction paradox* [12], because one would naively expect to see the scattering cross section converging to the physical one (i.e. normalized cross section around 1). This is not the case, the extinction paradox is a textbook example of fallacious intuition from geometrical optics. A detailed explanation of this phenomenon was given by L. Brillouin [46], who explained that the discrepancy lies in the interpretation of the Poynting’s flux theorem and in the role played by the scattered radiation in the shadow of the body. For longer wavelengths we see that the scattering cross section drops rapidly [47]. This is the regime known as Rayleigh scattering.

### 2.1.3 The interaction of light with small particles

When the particle that is scattering the light is much smaller than the wavelength, the scattering cross section drops with  $\frac{1}{\lambda^4}$ . This limit is known as Rayleigh regime. The expression for the scattering cross section is the following:

$$\sigma = \frac{\alpha^2 \omega^4}{6\pi \epsilon_0^2 c^4} \quad (2.25)$$

Where  $\alpha$  is the polarizability of the particle. This equation can be derived considering the particle as dipole oscillating in response to an external electromagnetic wave [13]. In Fig. 2.3 we report a plot of the scattering cross section for a sphere of 5 nm in the Rayleigh regime, computed with Mie theory.

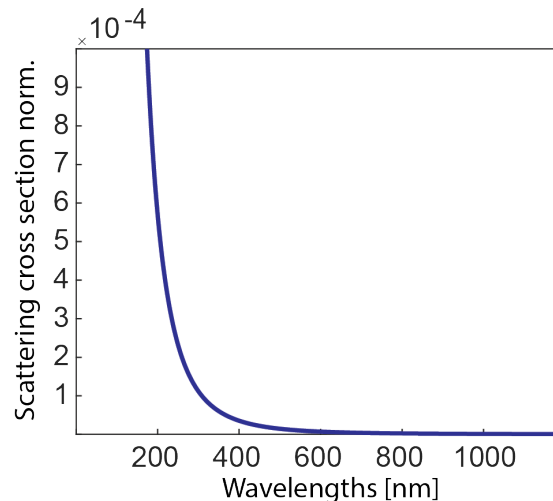


FIGURE 2.3: Scattering cross section computed for a sphere of radius 5 nm and a refractive index 2.3. Comparing the y axis in this plot to Fig. (2.2) we can see 4 orders of magnitude of difference compared to the case before.

This simple formula tells us that small particles scatter effectively the short wavelength part (i.e. the blue) and less the red/ near-infrared. This explains why we see the sky blue<sup>5</sup>. Since this formula is derived by approximating the particle with a dipole, it works pretty well for every shape much smaller than the wavelength.

#### 2.1.4 The internal field

Another important quantity that can be derived from Mie theory is the internal field in the sphere. In the range where  $\lambda \approx nr$  we have the low order modes of interaction ( electric dipole, magnetic dipole, etc... ) sometimes this ones are referred to as Mie modes. A host of seemingly different phenomena can be in fact explained as Mie modes and computed by Mie theory [48]. One recent example are resonant structures used for “Mie-resonant metaphotonics” [49][50], in which dielectric nano or microstructures are used to control the light at the nanoscale designing low losses nano-antennas. Another very famous example are the whispering gallery modes [51], in which the light travels around in a concave surface (they are supported by microspheres, as well as by microdisks)<sup>6</sup> These modes are typically used for lasers and sensing given their high quality factors [52][53][54]. A less known phenomenon is the photonic nanojet. It consists of the focusing that happens if the light is impinging on a sphere with refractive index close to 2 [55][56]. In Fig. 2.4 we show four examples of the internal field calculated with Mie theory, with a plane wave impinging on a microsphere of radius 1  $\mu\text{m}$ . We see that for wavelengths bigger than the radius we have an interaction similar to a

<sup>5</sup>It is not purple because our eyes has a very low sensitivity in the violet.

<sup>6</sup>Another discovery from Lord Rayleigh in 1878, who explained it for sound waves in St. Paul’s cathedral.

dipole. For shorter wavelength we have a superposition of the modes which gradually shifts to a focus on the rear part of the sphere. If the wavelength is much smaller than the radius we have a strong focusing of the electric field, which means a high concentration of energy in a small volume. The lateral confinement of photonic nanojet can be exploited to do hyperresolution imaging breaking the diffraction limit [57][58].

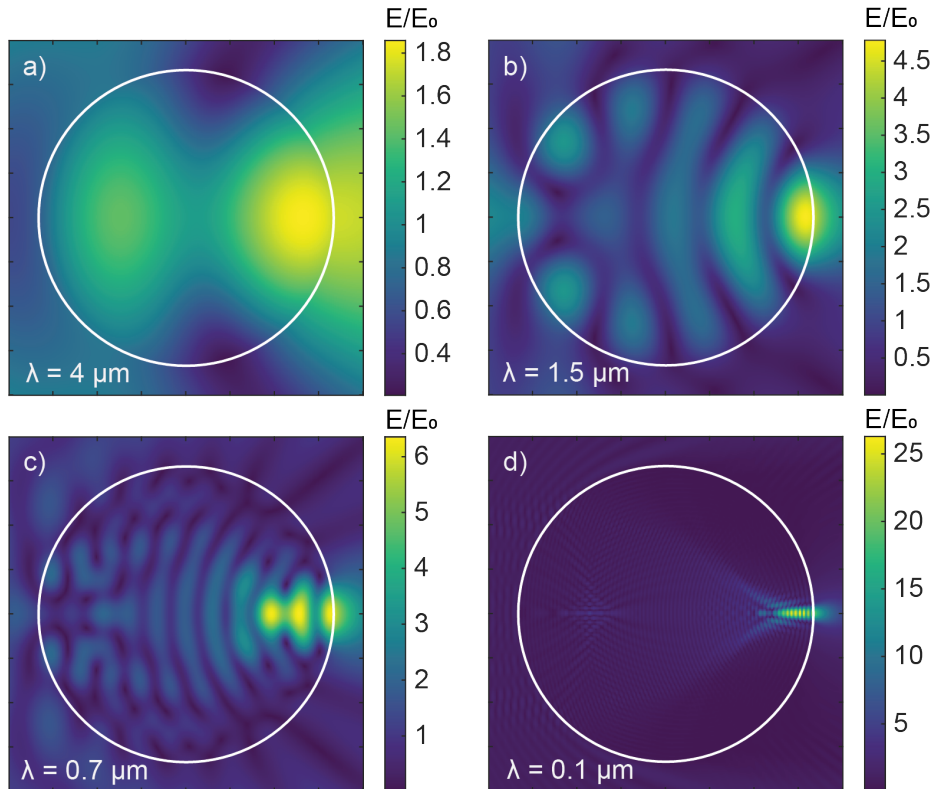


FIGURE 2.4: Internal field calculated with Mie theory for a sphere of  $1 \mu\text{m}$  of radius and refractive index 1.7. The displayed values is  $\frac{E}{E_0}$  where  $E_0$  is the amplitude of the impinging plane wave (coming from left to right). As we can see from a) the internal field distribution is similar to a dipole. By decreasing the wavelength in images b) and c) we see that the distribution of the electric field in the spheres becomes more complex and that a high intensity spot on the rear part starts to be evident. In figure d) the formation of a very strong focusing is very pronounced. This feature is the photonic nanojet. The electric field is concentrated in a small volume at the interface between the dielectric sphere and the air. For refractive index below 2 it lies more outside the sphere while for  $n > 2$  it is located in the inner part of the sphere. The increase in the electric field can be consistent. In the displayed case up to a 25 increase compared to the plane wave (and this is squared for the energy density).

Mie theory is very useful because it provides a theoretical framework valid from the Rayleigh regime to spheres much bigger than the wavelength like in the case of the photonic nanojet. Furthermore it constitutes a useful tool since it can be use to analytically compute the solution of the modes in

a microspheres without resorting to finite element methods, which are much more computationally demanding.

## 2.2 Multiple scattering

Mie theory and, when applicable, Rayleigh scattering can provide the solution of an individual scattering event. In many real occurrences there is not a single nanostructure that interacts with the light. A more frequent phenomenon is the scattering of the light on many particles and the propagation of electromagnetic radiation in a turbid medium. In such a material it would be possible to calculate the scattered field with Mie theory and the superposition principle. However, in practice the number of scattering events is so big that the problem becomes computationally heavy [59]. The field of light propagation in multiple scattering media is vast, well explored and it can not be treated fully in this chapter. Here, we give an overview of some important aspects and provide the key definitions that can help the readers get their orientation. A more thorough treatment can be found elsewhere [60][61]. The simplest representation of a scattering media is a binary system: a medium composed by two materials of different refractive indices  $n_1$ ,  $n_2$ , the classic case is air with some scatterers. A binary system composed of spherical particles of refractive index  $n_2$  in air (refractive index  $n_1$ ) is schematically represented in Fig. 2.5. The scattering strength depends on the arrangements and sizes of the particles, the refractive index ratio [62]. In particular, if we model the scattering as a sequence of individual scattering events, the scattering would be the strongest if the sizes of the particles and the voids are of the same order as the wavelength [63]. The scattering of a coherent wave by such a disordered material results in a complex spatial distribution of intensity both in reflection and transmission. This pattern is called speckle [64][65] and a typical example of speckle is shown in Fig. 2.5. While a single realization of a speckle pattern may be not particularly interesting, most often its statistical properties are of a great importance [14][66].

How can we quantify the scattering strength of a material? In literature two quantities are found [67][68]:

- the scattering mean free path  $l_s$  which is defined as the average distance between two scattering events.

$$l_s = \frac{1}{\rho\sigma_s} \quad (2.26)$$

where  $\rho$  is the density of the scatterers in the medium.

- the transport mean free path  $l^*$  that is the average distance that a photon travels in the turbid medium before his directions is completely randomized. The two quantities are different because often a single scattering event is not enough to randomize the direction of the scattered light. In fact the two quantities are linked with the following:

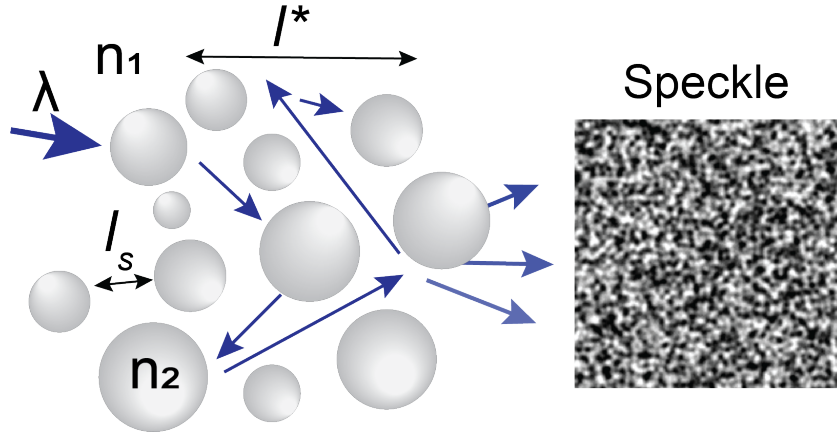


FIGURE 2.5: Sketch of multiple scattering in a binary material composed by air of refractive index  $n_1$  and polydisperse spherical particles of refractive index  $n_2$ . The scattering mean free path  $l_s$  and the transport mean free path  $l^*$  are also indicated. On the right side a speckle pattern is displayed. We can see the typical appearance with dark and bright spots given by the interference of the light scattered in the material.

$$l^* = \frac{l_s}{1 - g} \quad (2.27)$$

where  $g$  is the anisotropy factor, i.e.  $g = 0$  for isotropic scattering and  $g \approx 1$  is mostly forward scattering. As can be seen in the equation above,  $l^* > l_s$  because in most cases it takes more than a single scattering event to completely change the direction of propagation of the light. The scattering mean free path  $l_s$  and the transport mean free path  $l^*$  are schematically represented in Fig. 2.5.

### 2.2.1 Diffusive regime

If a multiple scattering material is much thicker than the transport mean free path, then the light does not propagate in straight rays and the direction of the light is deflected several times in the medium. The diffusion theory is applicable in the following range:

$$l_s \ll L \quad kl_s > 1 \quad (2.28)$$

The first requirement is rather clear: the sample has to be thick enough to allow the light to undergo an adequate number of scattering events to randomize its direction. The second one states that the scattering mean free path has to be bigger than the wavelengths of the material [28]. A typical scenario in optics takes place upon propagation of visible light in a material constituted by a dense assembly of high refractive index nanoparticles (for example  $\text{TiO}_2$ ). For example, in a layer 1 mm thick with a transport mean free path of  $10 \mu\text{m}$  the direction of the light is randomized every  $l^*$ . In such

a system, the unscattered light is exponentially suppressed in the material. This corresponds to the part of the light which is not deflected and it is called ballistic light in Fig. 2.6. The light that is scattered is called diffused light and it is linearly attenuated with the propagation depth.

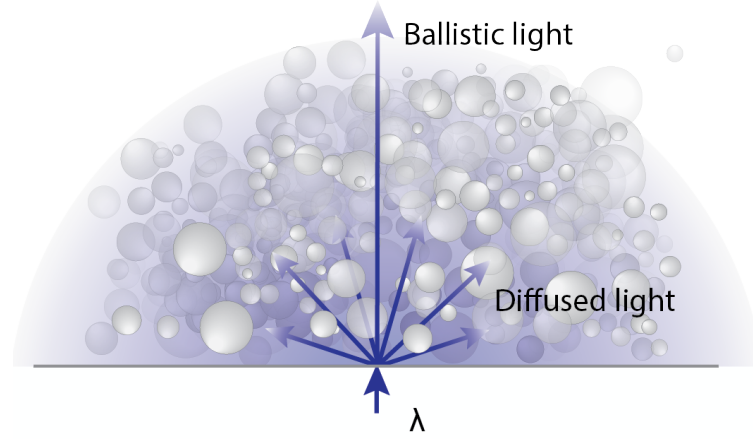


FIGURE 2.6: Sketch of light propagating in a multiple scattering medium composed by a polydisperse distribution of spheres. The light which stays in the original beam is called ballistic light and its intensity decreases exponentially with the depth of the material. The remaining optical power, which belong to the diffused light, is deflected in the material.

Apart from the conditions in Eq. 2.28, there are some assumptions on the multiple scattering process, that allow us to describe it as a diffusion process. First of all, every scattering event has to be independent from the previous one. Therefore, the direction and length of a each light step is memoryless, allowing us to use the framework of the random walk to describe the motion of light the in the material. Secondly, the scattering strength of the material should be homogeneous which means that distribution of the step lengths has to have finite moments. Based on these hypothesis, one can use the central limit theorem and derive a diffusion equation for the energy density of the light [69].

$$D\nabla^2\rho(\mathbf{r}) + S(\mathbf{r}) = 0 \quad (2.29)$$

where  $D$  represents the diffusion constant  $\rho$  the energy density and  $S$  is a source term. This equation tells us that the energy density of light in a multiple scattering medium diffuses from a point to another, similarly to what happens during Brownian motion of particles suspended in a liquid [70]. In practice, an individual ray of light is subjected to a random walk in the medium. We can use the diffusion equation in the case of light impinging on a slab to compute the total transmission.

$$T = \frac{l^*(\lambda) + z_0}{L + 2z_0}, \quad z_0 = \frac{2}{3}l^*(\lambda)\frac{1 + R_i}{1 - R_i} \quad (2.30)$$

where  $L$  is the thickness of the sample,  $z_0$  is the extrapolation length, and  $R_i$  is the internal reflectivity calculated with Fresnel laws [71][72]. In the limit of  $L \gg l^*$ ,  $L \gg 2z_0$  this equation can be rewritten

$$T = \frac{l^*}{L} \left( 1 + \frac{2}{3} \frac{1 + R_i}{1 - R_i} \right) \quad (2.31)$$

This equation is sometimes referred as Ohm's law for light [73]. This is in contrast to what happens in non-scattering materials, in which the attenuation is governed by Beer-Lambert law<sup>7</sup> and the light is exponentially suppressed in the medium [74]. In a multiple scattering material only a tiny fraction of the light is non-scattered (the ballistic light) and obeys Beer-Lambert law, however the total transmitted power which is constituted also by the light that is diffused in the sample decreases linearly with the thickness, following the Ohm's law for light (Eq. 2.31). The biggest limitation of the diffusion approximation is that by considering the light as a stream of energy density, completely disregards the wave nature of the light. In fact, it can not explain coherent effects, i.e. the interference of the light with itself during the propagation in the random medium [75]. One clear example of this is given by the coherent backscattering [76][77]. This phenomenon is the peak of intensity observed in the direction of the backscattering when the light impinges on a multiple scattering medium.

### 2.2.2 Beyond diffusion

Let us consider again the second condition expressed by Eq. 2.28. It states that the scattering mean free path of the material has to be bigger than the wavelength of the light [28]. When the wavelength is comparable to the  $l_s$ , we can no longer consider every scattering event as independent (see paragraph above) and this breaks one of the founding assumption of the diffusive regime. In other words, for  $kl_s < 1$  (known as Ioffe-Regel criterion) we enter a regime in which the interference effects are dominant in the scattering process [78]. The light is scattered before it can do one full oscillation. This condition is so different compared to usual wave optics that it is hard to develop a physical intuition of it. We can rewrite the Ioffe-Regel criterion using the Eq. 2.26, and using the duality of wavelength and radius of the sphere we can write

$$\sigma > \frac{k}{\rho} \gtrsim \frac{R}{\rho} \quad (2.32)$$

This toy model has a lot of limitations since it uses dilute scatterers to evaluate strong scattering regimes. However, we can use it to understand what size of nanoparticle would be the ideal to create a material whose mean free path length would be short enough to break the diffusion regime. In the graph on Fig. 2.7 we see that the Ioffe-Regel criterion is fulfilled when the scattering cross section is greater than the radius of the nanoparticles over

<sup>7</sup>The first formulation of the law can be attributed to Pierre Bouguer in 1729, but it is usually attributed to Johann Heinrich Lambert and August Beer in late 18th early 19th century



the density. The red line is plotted with an arbitrary  $\rho$  to illustrate the spectral window where Anderson localization<sup>8</sup> could take place [79].

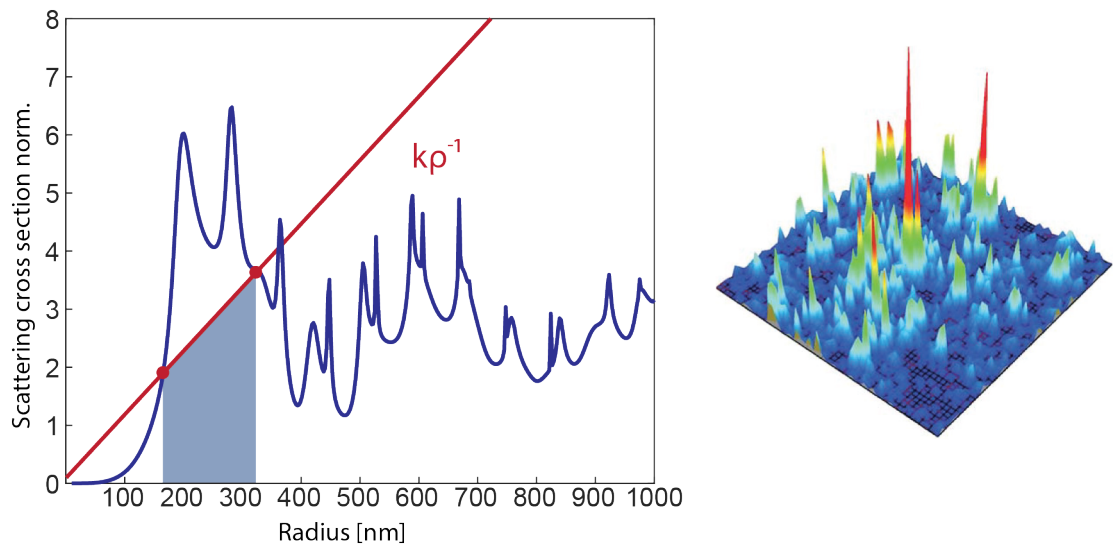


FIGURE 2.7: Spectral window for Anderson Localization. Scattering cross section of a sphere illuminated by a plane wave with wavelength 800 nm. On the right figure of the cover of the book "50 Years of Anderson localization" to testify that this is a long-lasting field of research (in this case it refers to localization of electrons) [80].

Thereby, an assembly constituted by scatterers with high refractive index and size of the order of  $r \approx n\lambda$ . Under these conditions, we would have the breaking of the diffusion approximation and the propagation of the light would be hampered by self interference, a phenomenon called localization. The localization is sometimes referred as Anderson Localization from the physicist G.L. Anderson that wrote the first seminal work on electrons in 1958. After that, researchers fostered localization of photons in disordered media in various geometries. 1D and 2D systems the localization is always possible provided that the material is bigger than the localization length [27], and has been experimentally measured [81][82]. This stems from the reduced complexity that random walks have in 1D and 2D structures. For dimensions  $d > 2$  localization should occur only over a critical level of disorder. This started the quest for the material with the shortest transport mean free path that would enable a disorder driven phase transition from diffusion to localization [25][83]. The existence and understanding of 3D Anderson localization of light is still heavily debated nowadays [84][85][86].

<sup>8</sup>Anderson localization, which is also known as strong localization, is the absence of diffusion in a disordered medium. It was first introduced by P.W. Anderson who applied this concept to electrons moving in a semiconductor with impurities and disorder.

## 2.3 Second-harmonic generation

When a light beam of frequency  $\omega$  impinges on crystal with dielectric properties, the electric field induces a polarization that is a nonlinear function of the field. To describe this process it is necessary to introduce the polarization field beyond the linear approximation [9].

$$\mathbf{P}(t) = \epsilon_0 \chi^{(1)} \mathbf{E}(t) \quad (2.33)$$

$$\mathbf{P} = \mathbf{P}^{(1)} + \mathbf{P}^{(NL)}. \quad (2.34)$$

$$\begin{aligned} \mathbf{P} &= \mathbf{P}^{(1)} + \mathbf{P}^{(2)} + \mathbf{P}^{(3)} + \dots \\ &= \epsilon_0 \left[ \chi^{(1)} \mathbf{E} + \chi^{(2)} \mathbf{E}^2 + \chi^{(3)} \mathbf{E}^3 + \dots \right], \end{aligned} \quad (2.35)$$

The parameters  $\chi^{(2)}, \chi^{(3)}$  etc. are the second- and third-order non-linear susceptibilities. In the general case, they are second-rank tensors and they are wavelength dependent. While all materials have the odd number susceptibilities, only a certain class of crystals display the even number tensors. In fact, the even number tensor are present only when there is the breaking of the inversion symmetry of the crystals. This happens in noncentrosymmetric crystals, i.e. in crystals without an inversion center. Another important case is given by the surfaces, in fact the interface between two media constitutes a symmetry breaking that allows for second order effects [87]. The  $\chi^{(2)}$  tensor, which has 27 components, can be contracted into a  $6 \times 3$  matrix and this allows us to rewrite  $\mathbf{P}^{(2)}$  in vectorial form:

$$\begin{pmatrix} P_x^{(2)}(2\omega) \\ P_y^{(2)}(2\omega) \\ P_z^{(2)}(2\omega) \end{pmatrix} = 2\epsilon_0 \begin{pmatrix} d_{11} & d_{12} & d_{13} & d_{14} & d_{15} & d_{16} \\ d_{21} & d_{22} & d_{23} & d_{24} & d_{25} & d_{26} \\ d_{31} & d_{32} & d_{33} & d_{34} & d_{35} & d_{36} \end{pmatrix} \cdot \begin{pmatrix} E_x^2(\omega) \\ E_y^2(\omega) \\ E_z^2(\omega) \\ 2E_y(\omega)E_z(\omega) \\ 2E_x(\omega)E_z(\omega) \\ 2E_x(\omega)E_y(\omega) \end{pmatrix}, \quad (2.36)$$

Then can be contracted into:

$$\mathbf{P}(2\omega) = 2\epsilon_0 d_{eff} \mathbf{E}^2(\omega) \quad (2.37)$$

This nonlinear response is responsible the conversion of some of the energy of the fundamental field into different frequencies. The most common application of this phenomenon is second-harmonic generation (SHG) in which a fraction of the light is converted into an output beam with twice the original frequency  $2\omega$ . In the quantum mechanical picture two photons impinge on the material exciting it into a virtual state, and the system relaxes back in the ground state emitting a photon of  $2\omega$ .

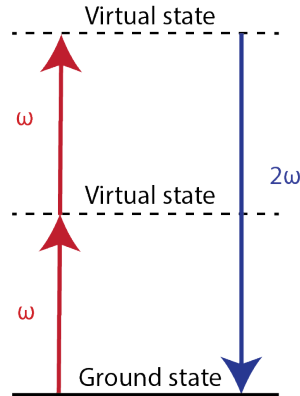


FIGURE 2.8: Energy diagram of the SHG. Thanks to the mediation of the  $\chi^{(2)}$  the two red photons are combined into a blue one.

This process is used to generate light at frequencies not easily available with a conventional laser, in SHG microscopy and it is unique tool to characterize crystalline materials. Another key application is spontaneous parametric down-conversion (SPDC) in which the pump generates radiation at two lower frequencies  $\omega_1$  and  $\omega_2$  such that  $\omega = \omega_1 + \omega_2$ . This process is sometimes called optical parametric generation and it is a key process in quantum optics since it is used to produce entangled photon pairs and also constitutes an excellent method to produce single photons. The outgoing photons are called the “signal” and “idler”. SPDC is said to be *spontaneous* because there is no input signal or idler field to stimulate the process. It is *parametric* because it depends on the electric fields (and not just their intensities), implying that there exists a phase relationship between input and output fields. *Down-conversion* refers to that fact that the signal and idler fields always have a lower frequency than the pump.

Assuming the undepleted pump approximation, following the calculation detailed in Boyd [9] we arrive to the result:

$$I_{2\omega} = \frac{8\omega^3 d_{eff}^2 I_{\omega}^2 L^2}{n^3 \epsilon_0 c^2} \text{sinc}\left(\frac{\Delta k L}{2}\right) \quad (2.38)$$

From Eq. 2.38 we learn that the intensity of the second harmonic grows quadratically with the intensity of the pump. Also it is quadratically proportional to the length of the crystal in which it is propagating. The last factor in the equation accounts for the wavevector mismatch and it will be discussed in the next section.

### 2.3.1 Phase matching

A key concept in the generation of SH is the phase-matching. When a laser beam is propagating through a nonlinear crystal the second harmonic will be generated along the propagation of the beam. In most material the refractive index decreases monotonically with the wavelength (normal dispersion) and

this means that the pump beam and the SHG travel with different speed and they acquire a phase mismatch while propagating in the crystal.

$$\Delta k = 2k_1 - k_2 = \frac{\omega}{c}(n(\omega) - n(2\omega)) \quad (2.39)$$

This phase shift embodies the different velocities at which the fundamental and the SHG travel in the crystal. This leads to a phase difference between the SHG generated in two different points in the crystal. If not properly addressed, this can result in destructive SHG interference at the crystal end.

The length at which the phase shift is  $\frac{\pi}{2}$  is called coherence length. After this distance, the SHG starts destructively interfere and it completely cancels out when the crystal is two coherence length long. This means that, in such conditions, there is a maximum second harmonic that can be extracted from the material, after one coherence length.

$$L_{coh} = \frac{\pi}{\Delta k} \quad (2.40)$$

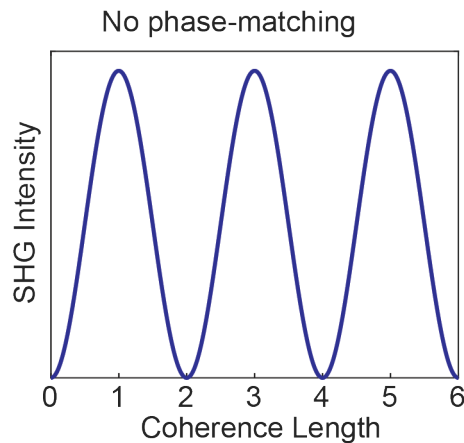


FIGURE 2.9: Non phase matched SHG calculated for a crystal with  $\Delta k \neq 0$ .

In most crystals that are isotropic  $\Delta k$  is only given by the wavelength dependence of the refractive index of the material. Therefore, in most cases,  $\Delta k \neq 0$ . This means that in a crystal the signal only grows over a certain length and after that it just goes back. (This still preserves the energy, simply the SHG destructively interferes and the energy flows back in the fundamental). This is scenario is plotted in Fig. 2.9. The simplest solution to counteract this phenomenon is to minimize (or if better to nullify  $\Delta k$ ). This is usually done in birefringent materials when operated at a specific angle and a specific polarization. As it can be seen in Fig. 2.10,  $\Delta k = 0$  means that the coherence length diverges and this allows the SHG to grow monotonously in the crystal. This is commonly done using, for example, barium borate crystals (BBO).

In many materials it is impossible to obtain the phase matching because simply there is no solution of the equation  $\Delta k = 0$ , i.e. no angle can cancel  $\Delta k$ .

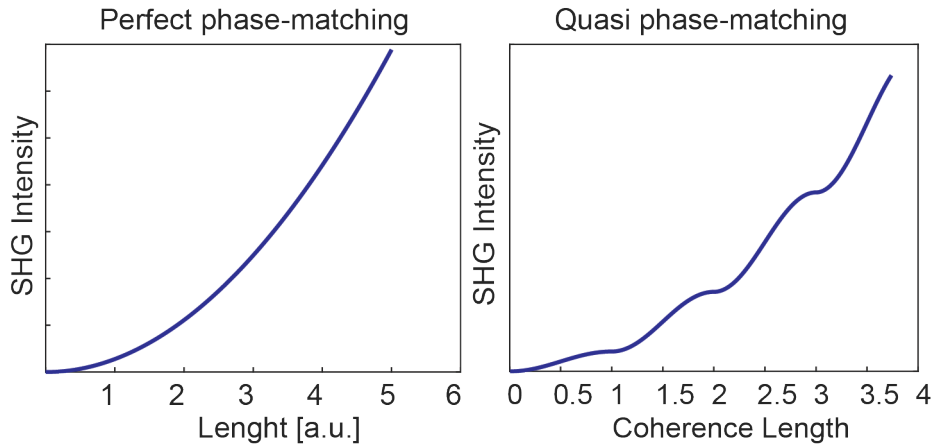


FIGURE 2.10: Perfect phase matching conditions make the SHG intensity grow quadratically with the length of the crystal. Quasi-phase-matched SHG grows with the same trend.

In these situation is possible to employ another strategy which is the quasi-phase-matching (QPM). This strategy is based on engineering the material flipping the crystals domain at each coherence length. This is represented in the plot on the right of Fig. 2.10. Both perfect and quasi-phase matching allow to produce second harmonic with intensity that scales quadratically with the length of interaction.

## 2.4 Random quasi-phase-matching

Perfect phase-matching and quasi phase-matching rely on a certain degree of order in that the wavelength and the polarization of the pump light have to be fixed, and the temperature and the orientation of the crystal have to be carefully controlled. This results in efficient SHG at the cost of being very wavelength-specific. There exists another approach which goes in the direction of exploiting disorder rather than order. This scheme is called random quasi-phase matching. It considers a disordered distribution of domains that generates nonlinear waves with random amplitude and phase, under the excitation of a pump beam. The interference of the SHG from the many random domains counter-intuitively does not destructively interfere. On the contrary the light generated from the disordered sources leads to a global second harmonic, whose power scales linearly with the sample thickness.

$$I_{SHG} \propto N \quad (2.41)$$

This linear scaling, whose properties have been investigated in recent numerical studies, is a fingerprint of RQPM since it is in contrast to the quadratic scaling of both phase-matched and quasi-phase-matched crystals. Therefore at the cost of a lower efficiency, it is possible to have SHG from crystals broadband and with a random polarization [39]. The counter-intuitive fact that the random superposition of many disordered nonlinear sources does not end up in destructive interference has been known since a long

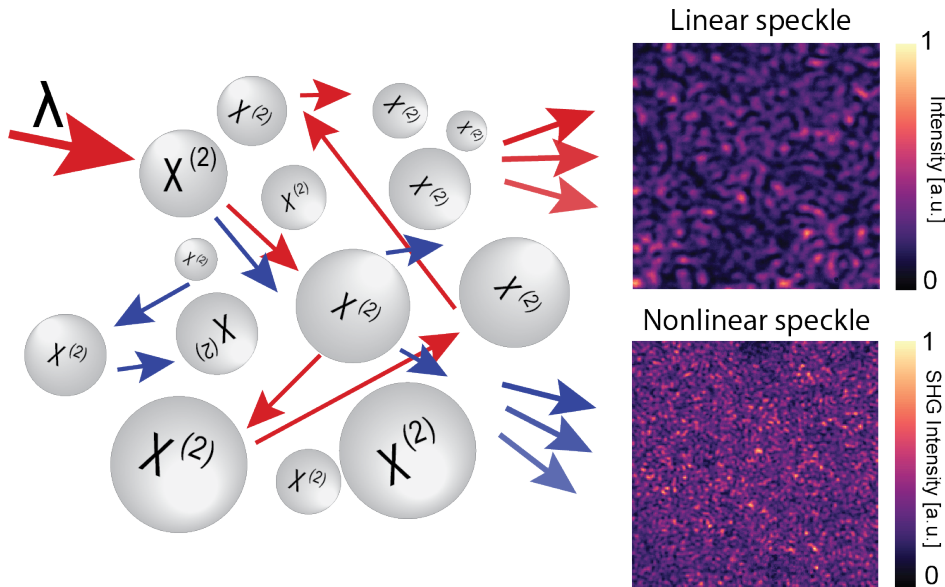


FIGURE 2.11: Sketch of multiple scattering material which is constituted by noncentrosymmetric particles. In red there is the impinging wavelength that is scattered in the material and in blue the generated and scattered second harmonic. Both these beam propagates and interfere in the material and result in linear (as shown in Fig. 2.5) and nonlinear speckle.

time. For example the second harmonic from powders of nonlinear crystals were used to study the components of their nonlinear tensor (identifying their crystal structure) [88]. Only more recently, this phenomenon has been called random quasi-phase matching[39]. In Fig. 2.12 it is possible to appreciate a that a sample of polycrystalline ZnSe can be more efficient than a single crystal, since the SHG that scales linearly with the number of grain can surpass the light generated by a single ZnSe crystal.

This process is one of the main focus of this thesis. It can generate second harmonic both in transparent and multiple scattering materials. The combination of scattering and nonlinear generation in the a material is represented in Fig. 2.11. Here, on top of the linear speckle that is generated by the interference of the pump scattered by every nanoparticle, we have a nonlinear speckle which results from the interference of the generated second harmonic by every  $\chi^{(2)}$  nanoparticle. It is interesting to note that the nonlinear speckle is present even in absence of any scattering in a fully transparent material. Since it is a result of a random interference, the scattering of the fundamental and/or the second harmonic simply adds a random phase in the process, therefore does not prevent the global second harmonic generation. A direct way to visualize how this random interference leads to a global signal can be given representing the SHG vector in the complex plane. In particular, if we consider the SHG generated by a 1D array of randomly oriented nonlinear crystals, we can compute the interference adding N phasors of SHG. They can be placed in the complex plane. In this case the SHG at the end of the complex system is represented by a random walk in this plane. The single

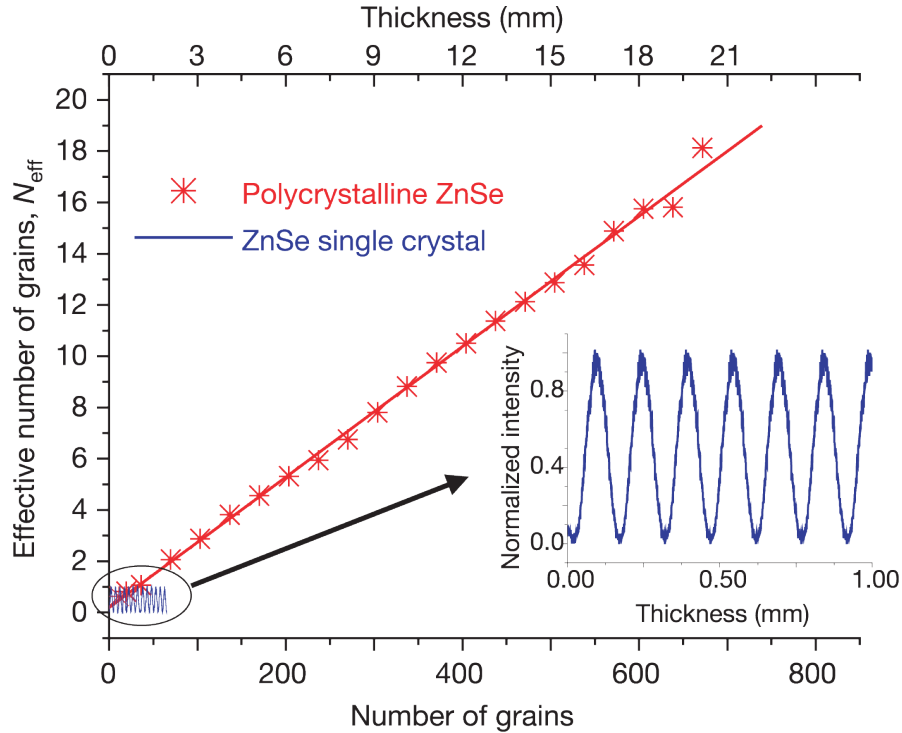


FIGURE 2.12: SH intensity as a function of the sample thickness. The scaling of a ZnSe polycrystal (averaged over different configurations of disorder) grows linearly with the number of grains. In the inset the oscillation of a single ZnSe crystal. This graphs shows that the disordered emission can outperform the a single crystal. Image reprinted with permission from Nature.

realization leads to a random result, but the average of many disorder configurations will have a certain average distance from the origin. (This is similar to the problem of the 2D walk of the drunken man, which will find himself after a certain time at a distance from the start proportional to the number of steps taken). This can be seen in Fig. 2.13 where we display the SHG from two different random crystals.

The single realization can fluctuate a lot, however after averaging over many realization of disorder (ensemble average), we retrieve the linear dependence of the intensity of the SHG with the number of the grains. Moreover, we can picture every speckle grain the nonlinear speckle being the result of an individual random walk in this phase space. Therefore, it will happen to have more constructive interference, leading to a bright spot in the speckle, and more destructive in other points of the image, resulting in a darker spot. Moreover this model can explain the origin of a speckle pattern in absence of scattering. In Fig. 2.14 we can see how a pump beam propagating in a transparent disordered and nonlinear material can produce a SHG speckle. Each small domain along the propagation of the fundamental produces second-harmonic light with amplitude and phase randomized by its position and orientation. If we add all the contribution from the domains at the end of the disordered assemblies we have a signal which is the interference of all the grains. The two examples displayed are from an assembly

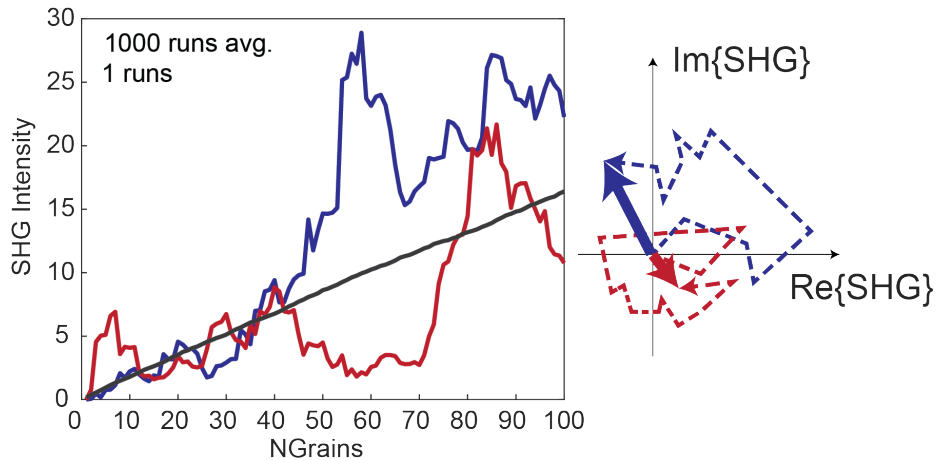


FIGURE 2.13: Simulation of a disordered crystal (1D). In red and blue are a single realization of disorder. In black there is the average result over 1000 realization from which we can see the clear linear trend. The simulation is obtained with the code presented in Appendix A.

with high efficiency and an assembly with mostly destructive interference. The final image is produced with the code detailed in Appendix A.



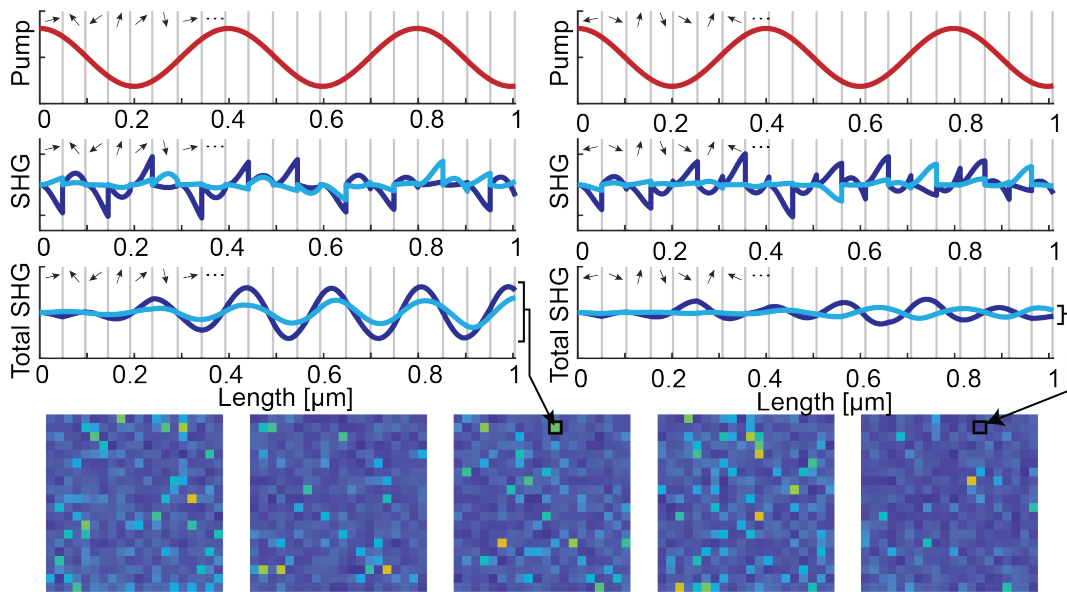


FIGURE 2.14: Local electric field in a transparent disordered 1D crystal. Two different configurations of disordered are presented in the left and right side. The fundamental wave travels in the crystal without being significantly deflected (birefringence is ignored). The SHG generated in each single domain is plotted on the second row where we can see that each contribution is randomly oriented. The total SHG represents the coherent sum of the locally generated fields. On the left we have a case that is mostly constructive while on the right the random interference generates a weak global signal. If we consider a 3D system made of these grain in parallel and we monitor the output after the last domain, we reconstruct a speckle pattern. Five different examples are plotted in the last row. This simple model can explain the appearance of a SHG speckle even in absence of scattering. The SHG speckle stems only from the random interference of the second-harmonic from randomly oriented and polydisperse in size domains.

## Chapter 3

# Materials and Fabrication

In this chapter we describe first the two main materials used in this work which are lithium niobate ( $\text{LiNbO}_3$ ) and barium titanate ( $\text{BaTiO}_3$ ). We discuss their most important properties and give their refractive indices in the visible range. We highlight their technological relevance linking it to specific material parameters, such as the coefficients of the  $\chi^2$  tensors for the non-linear properties. We detail the synthesis of the  $\text{BaTiO}_3$  nanoparticles and  $\text{LiNbO}_3$  nanocubes with chemical hydrothermal and solvothermal methods. These fabrication approaches can produce mono-crystalline structures down to sizes of the order of tens of nanometers. The produced particles have usually a quite broad size distribution. For materials that are hard to fabricate with top-down methods, the chemically synthesized nanoparticles are often one of the only viable approaches. The main challenge to exploit these particles consists in assembling them in structures with targeted functionality. We describe the emulsion-templated fabrication used to assemble the nanocrystals into microspheres and the fabrication employed to assemble the nanocrystals in a slab geometry. These procedures can control the global geometry of the assembly and do not control the orientation of the crystalline axis of the individual nanoparticles. The Brownian motion of the nanoparticles in solution ensures that they have a random orientation. One of the goal of this work is to exploit the intrinsic disorder that this fabrication entails. In the end, we mention briefly how the fabrication of the microspheres can be upgraded with microfluidics to target specific sizes of the assembly. In particular, we use microfluidics to assemble monodisperse microspheres composed by titanium dioxide ( $\text{TiO}_2$ ) with nanodiamonds.

### 3.1 Lithium niobate and barium titanate

Lithium niobate and barium titanate are ferroelectric metal-oxides. They can have different crystalline structure, two non-centrosymmetric crystal structures are displayed in Fig. 3.1. Many of their properties are similar: they have  $>2$  refractive index, and wide transparency window from the near ultraviolet (NUV) to the near infrared (NIR). Some of the properties are summarized in Table 3.1. They are both birefringent with ordinary and extraordinary refractive indices displayed in Fig. 3.2. Both are chemically inert materials, which makes them very robust, with high damage threshold since they can withstand intense laser pulses. This robustness makes them also

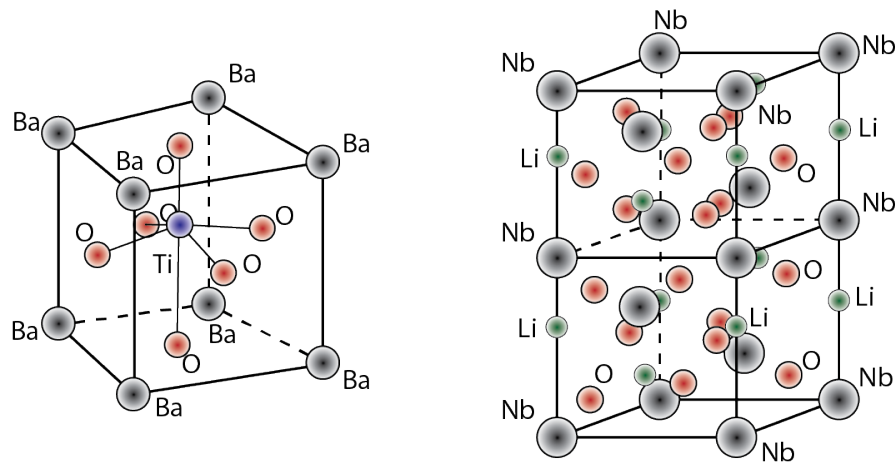


FIGURE 3.1: Crystalline structure of tetragonal barium titanate and hexagonal lithium niobate. Both crystals are non-centrosymmetric in that the titanium and niobium are displaced from the center inducing a permanent polarization on the crystals.

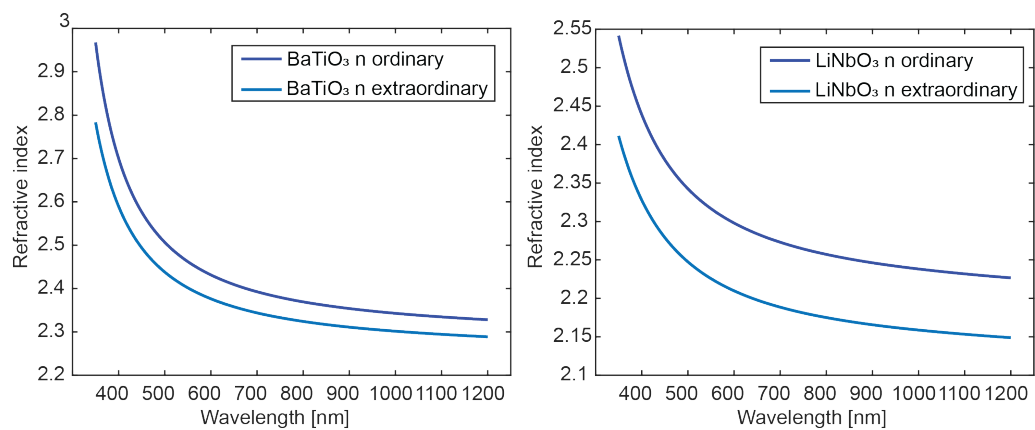


FIGURE 3.2: Refractive index of  $\text{LiNbO}_3$  and  $\text{BaTiO}_3$  in the visible and NIR spectrum. Both crystals are birefringent therefore have an ordinary and an extraordinary axis [89][90].

Material	Crystal structure	Bandgap (eV)	Electro-optic coefficient (pm/V)
BaTiO <sub>3</sub>	Tetragonal	3.5	8 to 1640
LiNbO <sub>3</sub>	Hexagonal	4	6.7 to 32.7

TABLE 3.1: Properties of tetragonal BaTiO<sub>3</sub> and hexagonal LiNbO<sub>3</sub>. The bandgap values are taken from [95]. The electro-optic coefficient of BaTiO<sub>3</sub> from [95], and of LiNbO<sub>3</sub> from [96].

very hard to etch, and for a long time they have not been used in any top-down fabrication process. In the last years, LiNbO<sub>3</sub> is becoming much more popular since it started to be available in the useful platform of lithium niobate on insulator (LNOI). This new platform, together with a step forward in the fabrication processes, has allowed to create photonic integrated circuits in LNOI [91][92]. Recently also thin films of mono-crystalline BaTiO<sub>3</sub> are became available thanks to molecular-beam epitaxy (MBE) [93], and pulsed laser deposition [94].

Besides their aforementioned linear optical properties, BaTiO<sub>3</sub> in tetragonal form and LiNbO<sub>3</sub> in hexagonal form display also nonlinear optical properties because they are non-centrosymmetric. This means that they have a non-zero second-order susceptibility tensor  $\chi^{(2)}$ . This fact allows them to display, for example, the Pockels effect which is a very interesting property stemming from the electro-optic coefficient. It links the applied voltage with the change in the refractive index of the material and has a lot of application for the production of memories or active devices [93]. Here lies another substantial difference between the two materials, in fact BaTiO<sub>3</sub> has an electro-optic coefficient two orders of magnitude greater than LiNbO<sub>3</sub>, as can be seen in Table 3.1. The most important parameters for the work presented in this thesis are the components of the  $\chi^{(2)}$  tensor which are the ones responsible for second-harmonic generation. They are summarized in Eq. 3.1 and Eq. 3.2.

$$d_{BaTiO_3} = \begin{pmatrix} 0 & 0 & 0 & 0 & d_{15} & 0 \\ 0 & 0 & 0 & d_{15} & 0 & 0 \\ d_{31} & d_{31} & d_{33} & 0 & 0 & 0 \end{pmatrix} \quad \text{with} \quad \begin{cases} d_{15} = -17.0 \text{ pm/V} \\ d_{31} = -15.7 \text{ pm/V} \\ d_{33} = -6.8 \text{ pm/V} \end{cases} \quad (3.1)$$

$$d_{LiNbO_3} = \begin{pmatrix} 0 & 0 & 0 & 0 & d_{21} & -d_{22} \\ -d_{22} & d_{22} & 0 & d_{31} & 0 & 0 \\ d_{31} & d_{32} & d_{33} & 0 & 0 & 0 \end{pmatrix} \quad \text{with} \quad \begin{cases} d_{22} = +2.1 \text{ pm/V} \\ d_{31} = -4.2 \text{ pm/V} \\ d_{33} = -27.0 \text{ pm/V} \end{cases} \quad (3.2)$$

We can see that the  $d_{33}$  component of the tensor of LiNbO<sub>3</sub> is bigger than the others and in specific crystal orientation this is the main component exploited for second-harmonic generation.

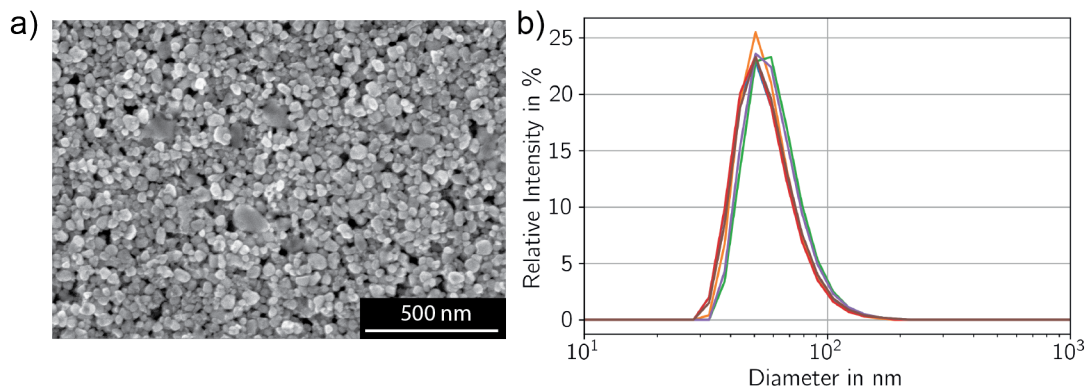


FIGURE 3.3: Characterization of the  $\text{BaTiO}_3$  nanoparticles from Nyacol. a) SEM images of  $\text{BaTiO}_3$  nanoparticles deposited on a substrate. b) Distribution of sizes of the nanoparticles measured by dynamic light scattering. Image adapted with permission from V. Vogler-Neuling PhD Thesis [98].

## 3.2 Synthesis of the nanoparticles

The barium titanate nanoparticles used in this work are commercially available from Nyacol (BT801, 25 wt. % in water, diameter of 50nm, tetragonal phase). The size of the nanoparticles was measured with SEM ( $42 \pm 1$  nm) and with dynamic light scattering (57 nm)<sup>1</sup>, as can be seen in Fig. 3.3. The potential of the  $\text{BaTiO}_3$  nanoparticles to assemble photonic structures is described in [97].

The lithium niobate nanoparticles were synthesized by the group of V. Buscaglia in ICMATE (Genoa, Italy). They were fabricated through solvothermal synthesis starting from 3 g of  $\text{Nb}_2\text{O}_5$  and 0.689 g of LiOH in 60 cc of ethylene glycol. The suspension was ultrasonicated for 5 min and then poured in a PTFE-lined stainless-steel acid digestion bomb (model PA4748, volume 120 mL, Parr Instrument Company). The product of the reaction was hydrothermally treated at 250 C for 70 h. This resulted in a powder suspension that was cooled down, washed several times with water and freeze-dried. The powder obtained contained  $\text{LiNbO}_3$  rhombohedra with sizes ranging from 100 nm to 400 nm. We refer to these nanoparticles with the term  $\text{LiNbO}_3$  nanocubes. These nanoparticles have been extensively studied in the PhD thesis of Flavia Timpu [99], which exploited their properties as Mie resonators using them as nanoantennas [100].

## 3.3 Emulsion-templated assembly

Microspheres of different materials have a variety of potential applications, from optical resonators [53][101], to microlenses [102], and biological probes

<sup>1</sup>The discrepancy can be explained because the dynamic light scattering measures the hydrodynamic radius, i.e. the radius that the particle assumes in the solution including the functionalization. Therefore the size is expected to be bigger than the one measured with the SEM.

[103]. In this work one of the goal is to assemble non-centrosymmetric nanocrystals with nonlinear properties into microspheres. To assemble the nanoparticles into microspheres we adopted a technique called water-in-oil emulsion-templated assembly [104][105]. This process exploits the immiscibility of two liquids, for example water and oil. By placing a small amount of water in oil and shaking it is possible to create an emulsion in which small droplets of water are embedded into the oil phase. If our nanoparticles are stable in water, it is possible to exploit this phase separation. The solution with water and nanoparticle is called *disperse phase*. The oil part of the emulsion is called *continuous phase* and in all our fabrication process it was Hexadecane. Additionally, the continuous phase has to be added with a surfactant<sup>2</sup>. This is a viscous organic compounds constituted by amphiphilic molecules (every molecule has a hydrophobic and a hydrophilic group).

Once the solution is shaken and it forms an emulsion, the surfactant forms a protecting layer around the droplets of nanoparticles and water in the oil, lowering the surface tension between the liquids. After waiting a few hours, the water diffuses out from the droplets into the continuous phase, the droplets shrink, and the water/oil interfaces compacts the nanoparticles into a microsphere [107], as we can see in Fig. 3.4a,b. This process can be controlled with temperature, pressure or with microwave irradiation [108]. During the diffusion time of water in the oil, the Brownian motion of the nanoparticles in water, ensures that the position and orientation of the particles is randomized. The result of this process is schematically illustrated in Fig. 3.4c. The assembling part of the process happens on a glass slide at a controlled temperature.

### 3.3.1 Microspheres of BaTiO<sub>3</sub> nanoparticles

We realized micrometer-sized spherical structures by the emulsion-templated assembly of colloidal BaTiO<sub>3</sub> nanocrystals (5% polydispersity, 50 nm diameter). 10  $\mu\text{l}$  of aqueous dispersion (2 wt%) of BaTiO<sub>3</sub> nanocrystals is mixed with 2.5 ml of surfactant-loaded (SPAN80 1 wt%) hexadecane. The solution was then emulsified by mechanical shaking to generate polydispersed water-in-oil droplets. Afterwards 100  $\mu\text{l}$  of emulsion was transferred onto a glass substrate and placed in the oven at 80° C for 12 hours. During this time the water diffusion in the hexadecane reduced the size of the droplets and the water/oil interfaces acted as dynamic templates for the assembly of the nanocrystals into larger microspheres. Their size distribution depends on the size dispersion of the droplets and on the concentration of the nanocrystals in water. After the baking in the oven, the residual surfactant was removed by gentle washing with hexane. As can be seen in Fig. 3.5, we generated microspheres with diameters from 0.5  $\mu\text{m}$  to 20  $\mu\text{m}$ . The assembled structures have a purely spherical geometry over the whole size range and the surface roughness is solely determined by the finite size of the nanocrystals. The microspheres are by kept surface forces. Since BaTiO<sub>3</sub> has a Curie temperature

---

<sup>2</sup>The word *surfactant* comes from **surface-active agent** and was created to specify the role of these compounds which control the surface tension between two liquids.

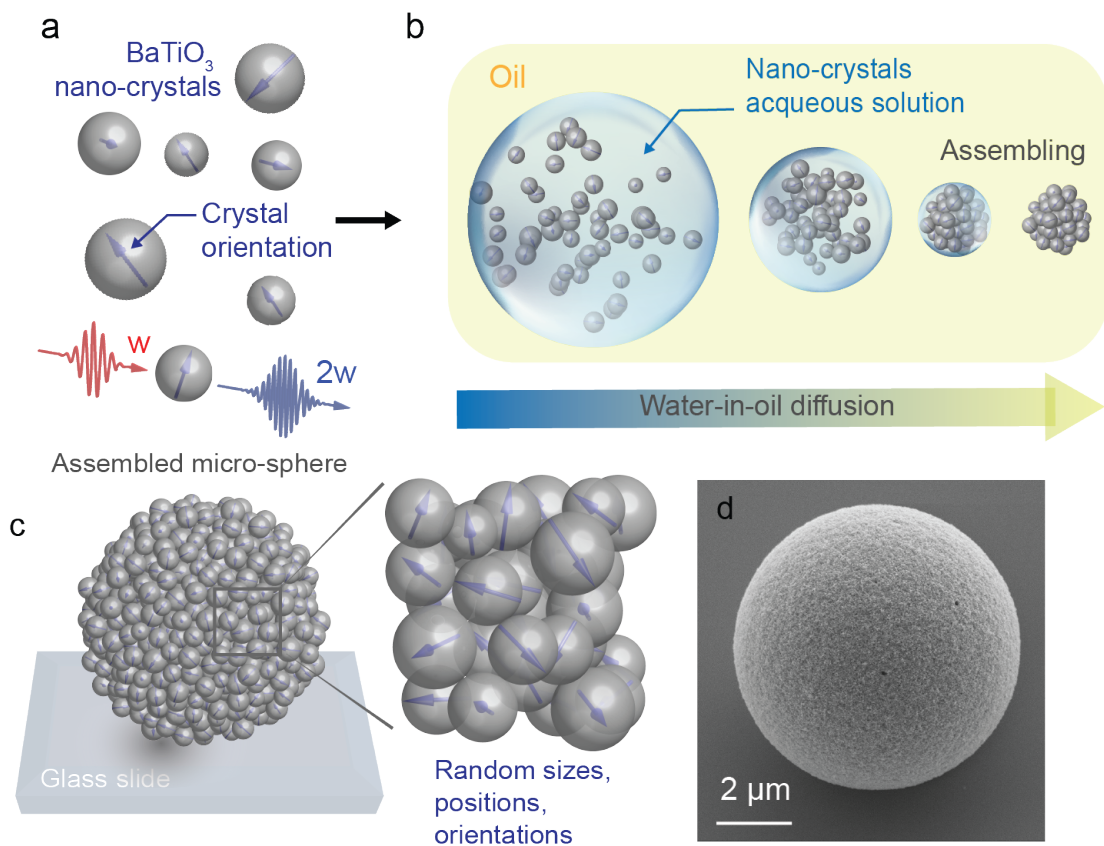


FIGURE 3.4: a) Representation of the BaTiO<sub>3</sub> nano-crystals dispersed in water. They have different sizes and orientations, which is indicated by the arrows. The SHG efficiency of the nano-crystals depends on the size and orientation with respect to the incoming beam. b) Sketch of the emulsion-driven assembly procedure. c) Representation of an assembled micro-sphere highlighting the randomness in the sizes, positions and orientations of the nano-crystals. d) SEM image of a BaTiO<sub>3</sub> micro-sphere assembled on a silicon substrate for better image quality. Image adapted from [106].

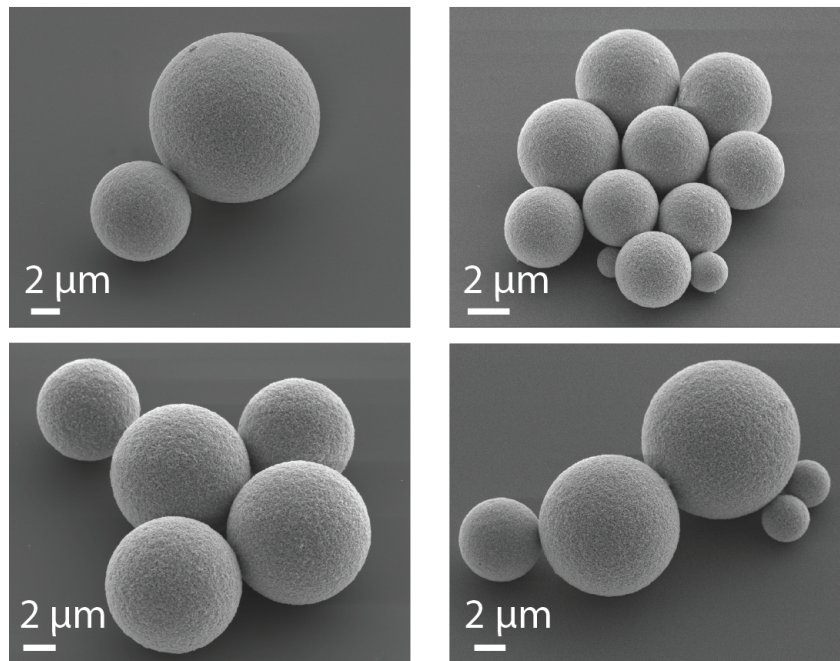


FIGURE 3.5: SEM images of  $\text{BaTiO}_3$  microspheres of different sizes. Each individual fabrication can produce thousands of spheres on a substrate.

of  $120^\circ\text{C}$  [109], the microspheres were not sintered. Exposing the nanocrystals to much higher temperatures could result in a non-reversible transition to the cubic crystalline phase and in the loss of non-centrosymmetry. Remarkably, they are robust and appear free from deformation several months after fabrication. In Fig. 3.5 we report some SEM images of cluster of spheres of different radii, to show that their surface quality is maintained over different sizes. In fact, in the range of radii between  $0.5\ \mu\text{m}$  to  $20\ \mu\text{m}$ , no difference can be observed. In this work, we studied the optical properties of individual microspheres. However, the tendency of these microsphere to cluster could have some application in fundamental studies [110][111]. Moreover, the optical coupling between spherical microresonators can have application in for low-loss light guiding over a long distance [112].

### 3.3.2 Microspheres of $\text{LiNbO}_3$ nanocubes

We fabricated the disordered microspheres by using the  $\text{LiNbO}_3$  nanocubes described in Section 3.2 and adapting the recipe used for  $\text{BaTiO}_3$  microspheres. We used emulsion-templated assembly technique; we mixed  $10\ \mu\text{l}$  of aqueous dispersion of the nanocubes (2wt%) with 1 ml of surfactant loaded (10wt% SPAN 80) hexadecane, followed by an emulsification process obtained through mechanical shaking. This process generates a polydispersed distribution of water-in-oil droplets filled with the nanocubes, which are collected and then deposited on a glass substrate with a pipette. The water in the droplets diffuses into the oil, shrinking the size of the droplets and forcing the nanocubes



to assemble into microspheres, as depicted in Fig. 3.6a. During this process and similarly as what occurred with BaTiO<sub>3</sub> nanoparticles, the Brownian motion of the nanocubes in the droplets ensures that each nano-cube is positioned and oriented randomly within the microsphere. As can be seen in Fig. 3.6b the microspheres in dark field are opaque white, suggesting that the light is multiply scattered in the structure. Fig. 3.6c displays a SEM image of a microsphere made of nanocubes. We can see that the structure is rough and the system is porous.

The obtained microspheres have diameters ranging from 2  $\mu\text{m}$  to 40  $\mu\text{m}$ . In Fig. 3.7 we have two examples of microspheres of different sizes. On the left side, a microsphere of roughly 3  $\mu\text{m}$  in diameter, shows the polydispersity of sizes of the nanocubes, as well as their random orientation in the assembly.

### 3.3.3 Microspheres of TiO<sub>2</sub> nanoparticles and nanodiamonds

Diamond containing nitrogen vacancy is a fluorescent emitter which is available in forms of nanoparticles that are usually referred to as nanodiamonds [114]. They have promising properties for bio markers and quantum sources. To better exploit their properties, it is crucial to couple the nanodiamonds to optically resonant structures [115]. In our case we used the emulsion templated assembly to fabricate TiO<sub>2</sub> microspheres with a small percentage of nanodiamond, to realize bottom-up resonators. We tried to exploit the optical modes given by the geometry to influence the emission of the nanodiamonds. To do that, we adapted the emulsion-templated fabrication explained in the previous sections for the new purposes. As is depicted in Fig. 3.8 the dispersed phase is composed by water with nanodiamonds (15mg/ml in deionized water, 100 nm average particle size, 3 ppm NV centers, *Sigma Aldrich*) and TiO<sub>2</sub> nanoparticles (Titanium Oxide (Anatase), 15 nm average particle size, dispersion in water, 15 wt%, *Nanostructured & Amorphous Materials Inc.* Hexadecane (95%, *Alfa Aesar*) with a mixture of two surfactants, Span 80 (Sorbitan monooleate, *Sigma Aldrich*) and Tween 60 (Polyoxyethylen(20)-sorbitan monostearat, *Sigma Aldrich*) was used as a continuous phase. The concentration of surfactants in the continuous phase was 4wt% Span 80 and 1wt% Tween 60. 10  $\mu\text{l}$  of nanoparticle solution and 1 ml of surfactant loaded hexadecane were filled into a 2 ml Eppendorf and emulsified by shaking. The emulsion was deposited onto a glass substrate and put in the oven for 4 hours at 80° C. With this technique it is possible to have full control the concentration of the nanodiamonds in the microsphere. As can be seen in Fig. 3.8b the resulting assembly are very homogeneous and under the dark field microscope they appear of light blue color. From the SEM image in Fig. 3.8c we see a microsphere with nanodiamonds on the surface. To study the internal structure and composition, we cut the microsphere with focused ion beam milling, revealing the internal structure. We see in Fig. 3.8d which is SEM collecting the backscattered electrons that some nanodiamonds are randomly distributed in the volume of the sphere. The dark appearance tells us

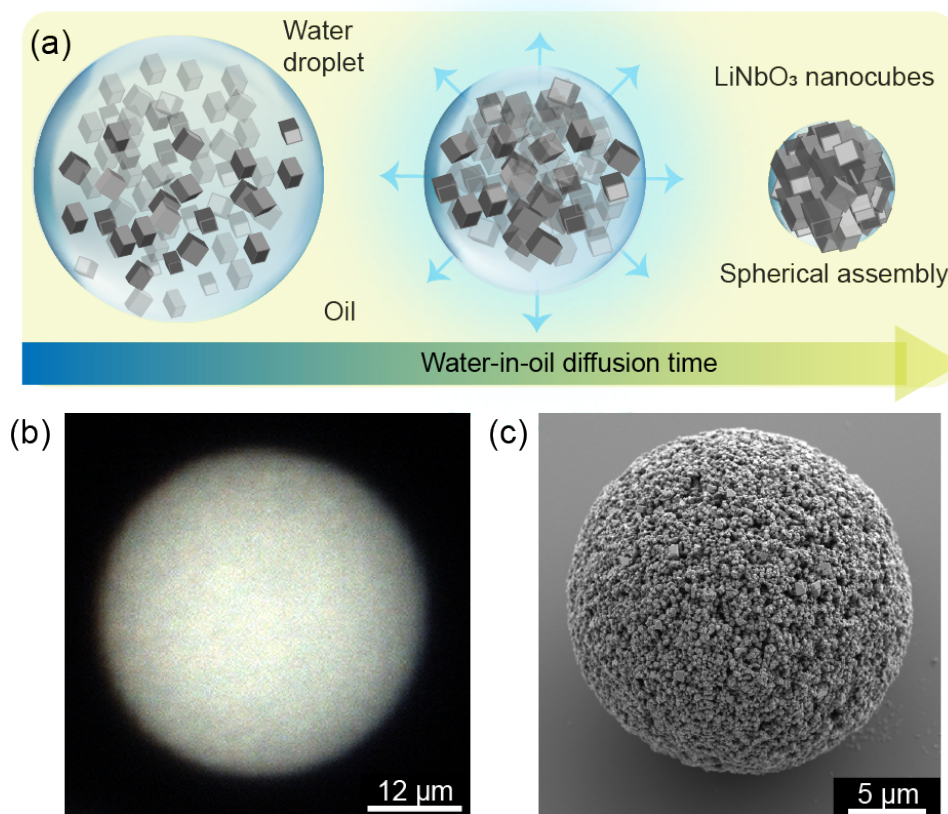


FIGURE 3.6: Fabrication of the LiNbO<sub>3</sub> microspheres. a) Principle of the emulsion-templated assembly of the LiNbO<sub>3</sub> spheres. b) Dark-field microscopy image of an assembled microsphere obtained with a 50x apochromat objective. The white appearance suggests that the light undergoes multiple scattering in the microspheres. c) Scanning electron micrograph image of an assembled microsphere, which was also used to precisely measure the volume of the microspheres. This image is adapted from [113].

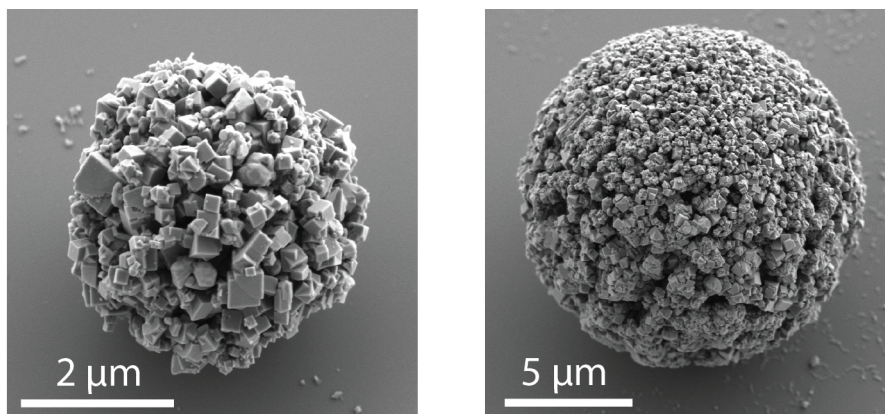


FIGURE 3.7: SEM images of two microspheres made of  $\text{LiNbO}_3$  nanocubes. The spheres are rough and porous because of the constituting nano-cubes are not small enough to form a smooth surface.

that the element has a lower atomic weight compared to titania (compatible with the carbon of the nanodiamonds).

### 3.3.4 Spin coated nanodiamonds

In Chapter 6 we use spin coated nanodiamonds on a glass sample to measure the second-order correlation function  $g^{(2)}$ . To do that we employed nanodiamonds that contained on average a single NV center (Carboxylated 20 nm Red Fluorescent Nanodiamond in DI water, < 1ppm NV center from *Adamas Nano*). To fabricate slabs with different concentration of nanodiamonds per unit area we used different spin coating parameters. The recipe that was employed was 50 rpm/m of acceleration and 2000 rpm of velocity for 2 minutes.

### 3.3.5 Monodisperse $\text{TiO}_2$ microspheres with microfluidics

Up to this point, we have been interested in producing polydispersed spheres. However, for many applications it would be of great importance to control the size of the microspheres. This is not possible with the mechanical shaking of the Eppendorf or by using a vortex to shake the emulsion. Nonetheless, there are established techniques in materials science that allow to fabricate monodisperse microspheres by emulsions assembly. This whole branch of material science is called microfluidics and it involves the use of small channels to control the forces acting on fluids at the microscale. We tested this possibility in collaboration with the Laboratory for Soft Materials and Interfaces of Prof. Lucio Isa. In Fig. 3.9, it is reported a picture of the microfluidics circuit that we used. It consists of a T-junction for two-phase mixing. This device can generate droplets of different sizes that can be controlled with the flow rate. The dispersed phase is pushed from the left and crosses the continuous phase that flows from top to bottom in the picture. This flow at constant speed can create highly monodispersed droplets. If we use the continuous phase and dispersed phase described in the previous section, we can

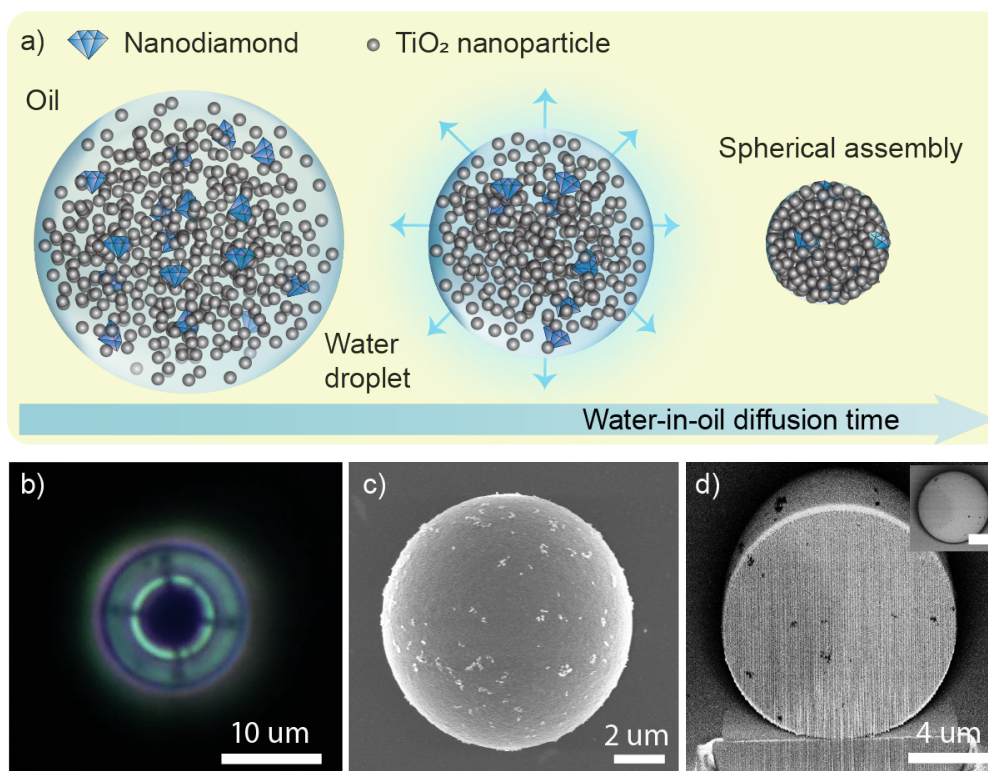


FIGURE 3.8: a) Sketch of the emulsion templated assembly fabrication of hybrid sphere with a matrix of  $\text{TiO}_2$  and variable concentration of nanodiamonds. b) Dark field image of a hybrid microsphere, the light blue color stems from the Rayleigh scattering of the 15 nm titania particles, the ring comes from the illumination. This is possible because the sphere is very homogeneous and interact with the light like an effective medium, i.e. like a spherical microlens. c) SEM image of the microspheres, the white dots on the surface are the nanodiamond. d) Cross section of the sphere obtained by FIB and with the backscattered electrons. The dark spot here corresponds to the white ones of the image in c). The brightness is linked to the atomic weight of the element, therefore the carbon in the nd scatters less the electrons compared to  $\text{TiO}_2$ .

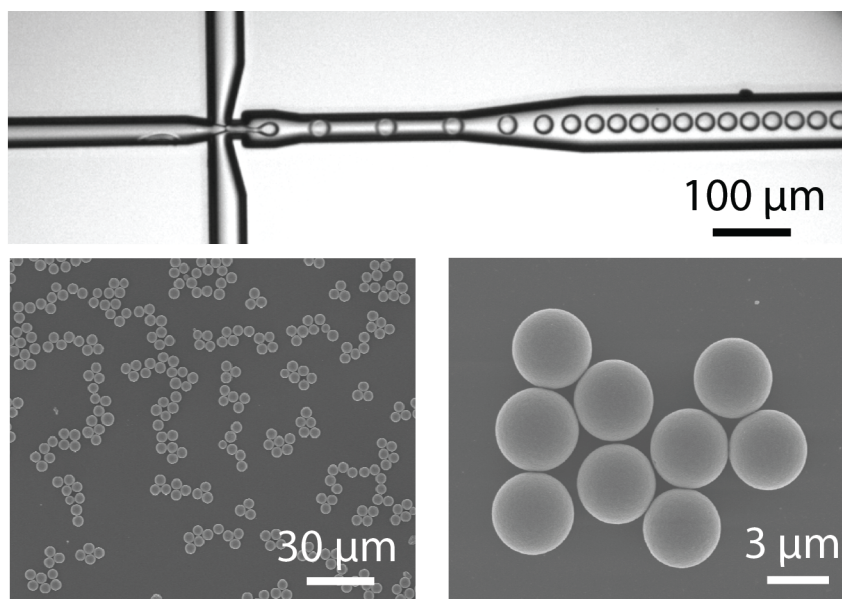


FIGURE 3.9: a) Picture of the microfluidics setup used to produce  $\text{TiO}_2$  microspheres. Photograph of the T-junction microfluidic setup used to fabricate the microspheres. The dispersed phase of water and  $\text{TiO}_2$  nanoparticles flows from left to right and the continuous phase of surfactant-loaded hexadecane from top to bottom. This process generates the droplets that can be seen in the right part of the image. b) SEM image of many microspheres. c) Close up SEM image on a cluster of microspheres which are smooth and monodispersed.

fabricate microspheres of arbitrary fixed size. We tested this fabrication with spheres of  $\text{TiO}_2$  and this resulted in the microspheres showed in Fig. 3.9. Employing microfluidics enables to create microsphere of excellent surface quality and with controlled size to target specific properties.

### 3.4 Slabs assembly

As useful as spherical geometry can be, having a flat layer (or slab) of a given material is essential for many applications. The physics in slab is more easily modeled with analytical approaches and even faster simulated. For these reasons, we developed a recipe to assemble the  $\text{LiNbO}_3$  nanocubes into slabs. Unfortunately, a simple drop-casting method is not sufficient because in a droplet drying on a flat hydrophilic surface, a faster evaporation occurs at the edges of the droplet and this generates an outward flow responsible for the accumulation of the solute at the borders [116]. In our case this would have produced rings of nanocubes and not the flat layer that we were aiming to. This phenomenon is known as the coffee-ring effect [117][118]. We assembled the nanocubes into slabs by drop deposition and solvent evaporation. An aqueous suspension (2wt%) of the  $\text{LiNbO}_3$  nanocubes was mixed with 30% polyvinyl alcohol and deposited over a glass substrate framed with hydrophilic tape, as depicted in Fig. 3.10. The sample was placed onto a

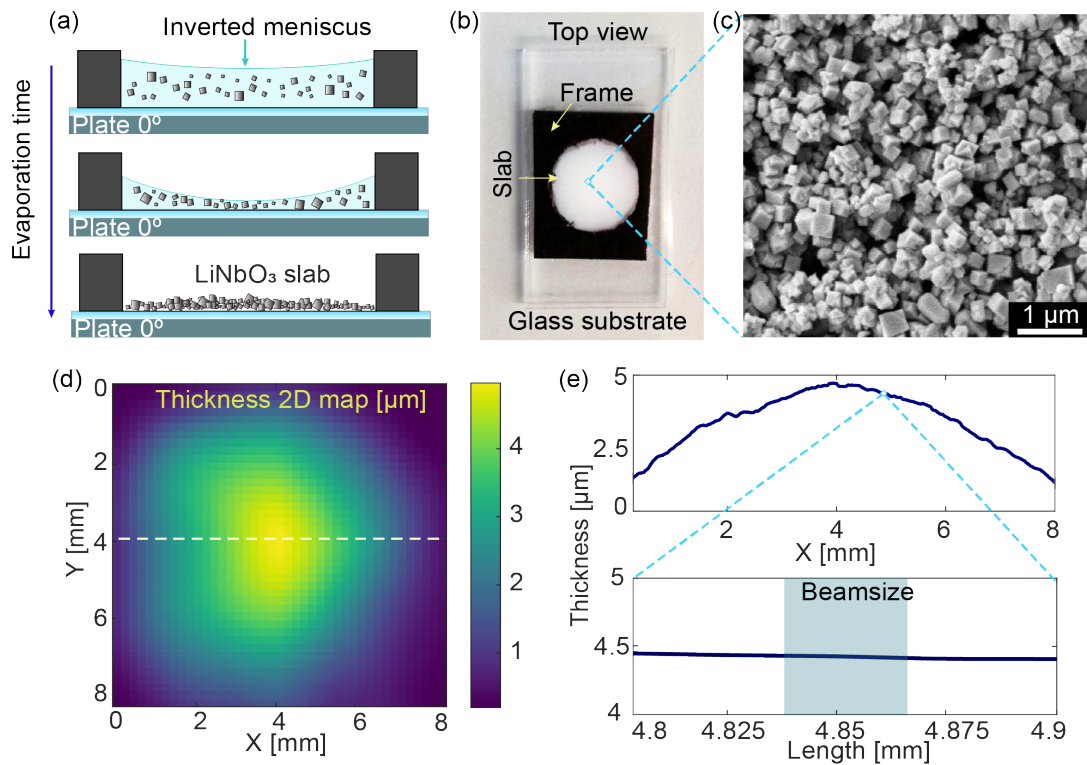


FIGURE 3.10: Fabrication and thickness characterization of disordered LiNbO<sub>3</sub> slabs. a) Schematic of the inverted meniscus technique to avoid the coffee ring effect. The contact angle between the liquid and the frame ensures a uniform deposition in the center of the sample. b) Top view of a typical sample. Prior to the deposition, the substrate was cleaned with acetone and ethanol, followed by 10 min of plasma cleaning. The white circle is the slab and the black frame around it is the tape. The slab is unsealed from the top. c) SEM image of the slab surface composed of nanocubes of LiNbO<sub>3</sub>. d) 2D map of the thickness of the slab measured by profilometry technique. e) Measured thickness along the white dashed line reported in d) with a close-up on a smaller region of 0.1 mm. The sample can be considered flat on the length scale of the beam diameter (30 μm).

Adapted from [113].

horizontal substrate holder within an isolating box filled with ice water to keep the sample at 0° C. After 36 hours, the nanocubes were deposited and the water had evaporated. We prevented the coffee ring effect by adding a frame around the droplet, which ensured that the meniscus of the suspension stayed concave during the evaporation of the water. This inverted meniscus technique made the suspension evaporate first in the center of the droplet such that the resulting internal capillary flow carried most of the nanocubes towards the center of the droplet where they deposited. Under visible light illumination, the slabs have the white appearance that is typical of multiple scattering media, as can be seen in Fig. 3.10b. In Fig. 3.10c a SEM picture of the surface of the slabs to show a uniform packing of the nanocubes. The measurement of the thickness of the slab was performed with profilometry. Thanks to this technique it is possible to realize a 2D scan of the thickness of the sample over a large area (contrary to what is usually achievable with atomic force microscopy). The 2D map is presented in Fig. 3.10d, with the plot over a line displayed in Fig. 3.10e. We can see that the thickness changes smoothly with the lateral size of the sample, such that it can be considered flat on the length scale of tens of microns. However different thicknesses can be obtained by translating the sample with respect to the laser beam.

### 3.5 Measurement of the filling fraction

To study how the nanoparticles are assembled in the microspheres we cut them with focus ion beam (FIB) milling. This allowed us to see the interior of the microsphere and to measure the filling fraction by image analysis of the cross section. The images are taken with the SEM with the same FIB-SEM NVision40-Zeiss. To minimize the local charging effects, the sample was previously covered with a 3 nm layer of platinum that was sputtered in the deposition chamber Elios600i. To achieve uniform deposition the sample was mounted on a planetary stage during the sputtering. The cross section of a microsphere of about 3  $\mu\text{m}$  of diameter is shown in Fig. 3.11a. The image is tilt-corrected in the vertical direction to preserve the proportions. The image is then binarized through the adaptive Otsu algorithm [119], through the function `IMBINIRIZE`, which returns 0 for the empty space and 1 for a pixel filled by a nanocrystal. The high contrast image is shown in Fig. `IMBINIRIZEb`. A circular region of interest was selected starting from the center of the cross section with different radii. The filling fraction  $ff$  is measured as  $ff = N_{full}/N_{TOT}$ .  $ff$  was measured at different radii to test if the porosity was homogeneous in the assembly. This measure is displayed in Fig. 3.11d shows that the filling fraction is roughly constant in the volume with a value of  $ff \approx 0.55$ . The same procedure was applied to 5 different spheres with radii in the range 1-5  $\mu\text{m}$ , resulting in similar results. This  $ff$  is consistent with the limit given by the random close packing which are in the range 50-70% [120][121]. The value of the filling fraction is fundamental for optical studies since it is closely linked with the effective refractive index.

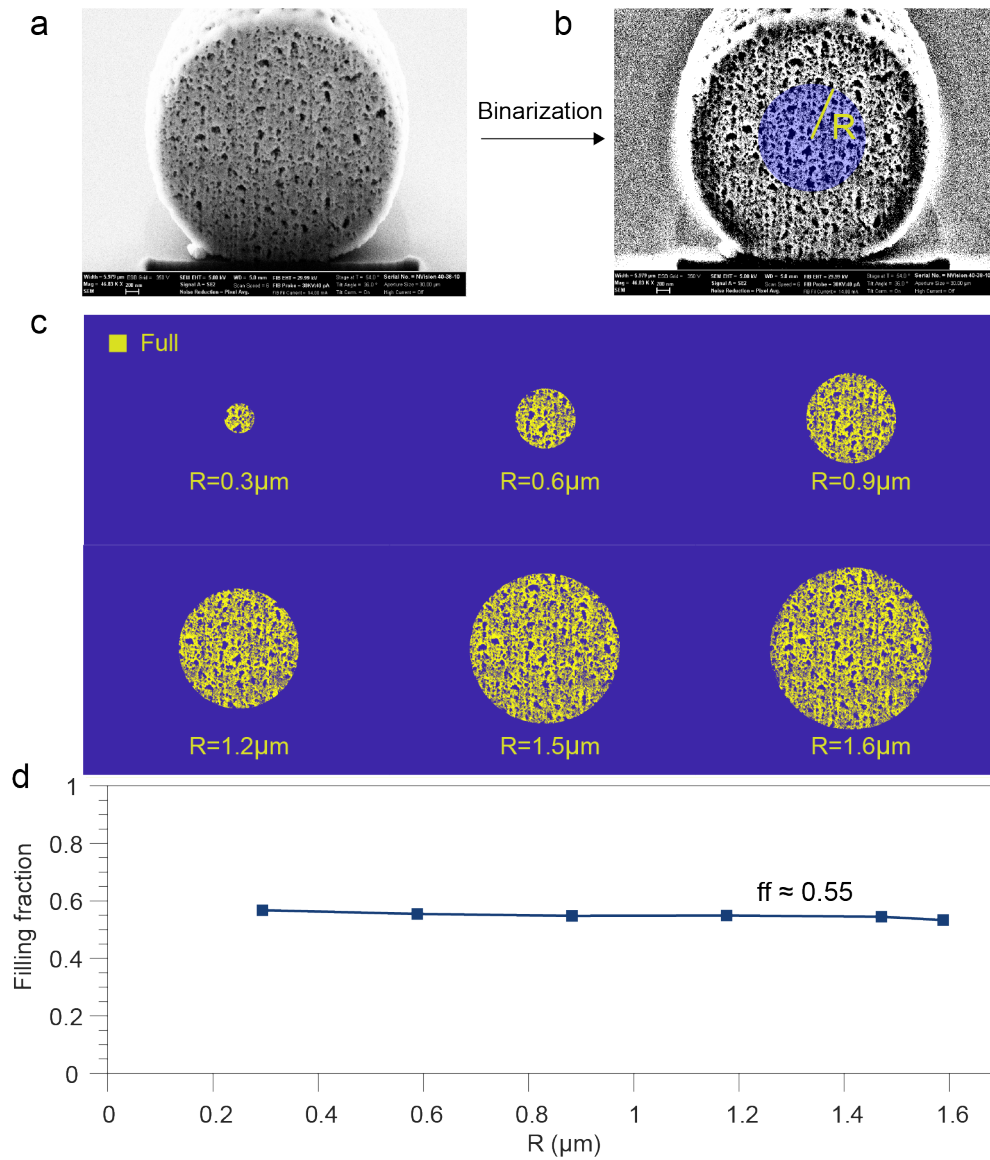


FIGURE 3.11: Filling fraction study on the microspheres. SEM image of a FIB cut of a microsphere. b) Binarized image for different radii. The algorithm used is Otsu algorithm [119]. c) Displayed binarized cross sections. The filling fraction measured with this technique is 0.55. d) Measured filling fraction as a function of the radius of the selection region.



### 3.5.1 Effective refractive index with the Maxwell-Garnett mixing rule

When dealing with a macroscopic composite material, it can be convenient to describe some of its properties as if it was an homogeneous medium. These models are called effective medium approximations or effective medium theories. In the field of optics, one of the prominent application of these homogenization theories is the concept of effective refractive index  $n_{eff}$ . In practice, under some conditions it is possible to treat a composite system as an homogeneous medium with an effective refractive index. The advantage of using an effective-medium theory lies in its simplicity and in the possibility to describe the optical behaviour of a complex medium with a single parameter [122]. In general, effective-medium mixing formulas are expected to work well for diluted composite media with a low index-contrast [123]. However, when the size of the composite medium gets smaller (e.g. nanoparticles clusters, meso-crystals), the main requirement is to have individual nanoparticles with an optical response dominated by the electric dipole term [124]. In our case, BaTiO<sub>3</sub> nano-crystals have a full dipole behaviour, with a size parameter  $x \approx 0.3$  (Rayleigh scattering regime), and the effective-medium approximation is a viable solution. On the contrary, the microspheres assembled with LiNbO<sub>3</sub> nanocubes can not be described with an effective medium approach. In fact, the approximation gets weaker when light scattering from the constituent particles/enclosures is not negligible. In such a case an exact solution of Maxwell's equations is required.

We calculated the effective refractive index of the assembled nanocrystals-air composite with the Maxwell-Garnett<sup>3</sup> mixing rule is reported in Eq. 3.3, with  $n$  the average refractive index of bulk BaTiO<sub>3</sub> and  $ff$  the nano-crystals filling fractions of the composite [125]. The wavelength-dependent effective refractive indices calculated at different filling fractions are shown in Fig. 3.12.

$$n_{eff}^2(\lambda) = \frac{1 + \frac{2ff}{3}(n^2(\lambda) - 1)}{1 + \frac{ff}{3}(n^2(\lambda) - 1)} \quad (3.3)$$

We employed the MG model, and not other effective-medium mixing rules as the Bruggmann's rule [125] because MG provides a slightly better estimation of the effective refractive index for small and packed systems [123].

## 3.6 Declaration of personal contribution

The idea of the fabrication of the microspheres through the emulsion-templated assembly was the result of a collaboration between Dr. Romolo Savo, who started the project, and Prof. Lucio Isa and Michele Zanini (from ETH group

<sup>3</sup>James Clerk Maxwell Garnett (1880–1958) was the son of physicist William Garnett, who named his son after his friend James Clerk Maxwell the renowned physicist.

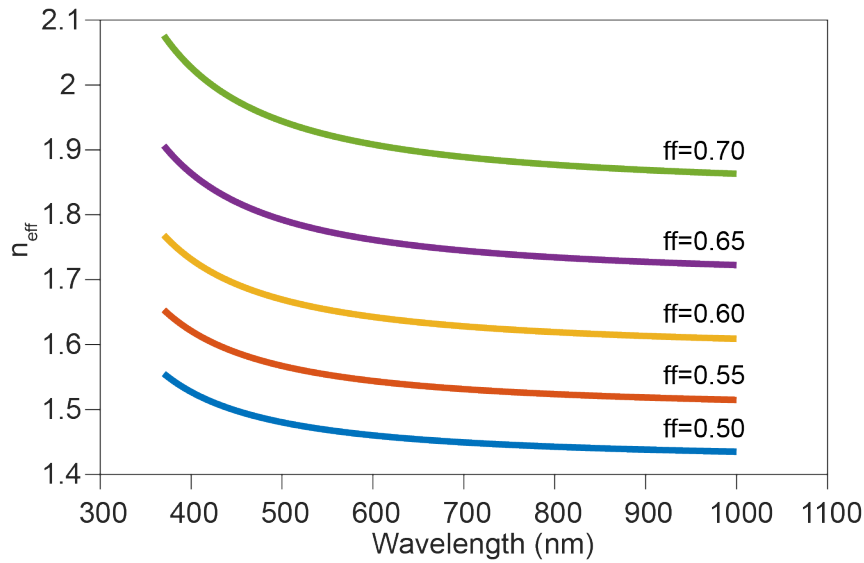


FIGURE 3.12: Wavelength-dependent effective refractive indices for the BaTiO<sub>3</sub>-air composite calculated with the Maxwell-Garnett mixing rule at different filling fractions. Assembled micro-spheres have a refractive index corresponding to  $ff = 0.55$ .

of soft materials and interfaces). My contributions were the development of the actual recipe for the BaTiO<sub>3</sub> nanoparticles (type and quantity of surfactant, temperature and timing of procedure, etc...), the FIB milling and the profilometry. The fabrication of the LiNbO<sub>3</sub> microsphere was adapted by Jolanda Müller during her master thesis. The hybrid microspheres with TiO<sub>2</sub> and nanodiamonds was developed with the contribution of Andrea Scheidegger during her master project. The microfluidics assembling was done by Dr. Minghan Hu (from ETH group of soft materials and interfaces). The disordered slabs of LiNbO<sub>3</sub> nanocubes were fabricated by Simeon Richter under Dr. R. Savo supervision.



## Chapter 4

# Mie driven random quasi-phase-matching in BaTiO<sub>3</sub> microspheres

In this chapter we study the second-harmonic generation from bottom-up microspheres of BaTiO<sub>3</sub>. The fabrication of the microspheres is presented in Chapter 3. The goal is to show that it is possible to couple the SHG obtained through random quasi-phase-matching with resonances given by the spherical geometry of our assemblies. We begin by providing the context of nonlinear generation in disordered materials, highlighting the advantages and the disadvantages of exploiting a disordered structure over an ordered one. This scheme is called random quasi-phase-matching (RQPM). After the context is given, we present the linear measurements on the microspheres. We show that the linear scattering cross section and the internal energy of the bottom-up microspheres can be matched with the results obtained through effective medium approximation combined with Mie theory (effective medium Mie model, EMM) as well as with the finite element method simulations (with COMSOL). These results verify that the homogenization theory can be applied to our microspheres and that the quality of the fabrication is good enough to sustain resonances.

Next, we show the measurements of the second-harmonic signal from the spheres. To pump the assemblies we use a femtosecond pulsed Ti-Sa laser in the visible. We provide evidence of the nonlinear generation measuring the quadratic power scaling and the spectrum of the emitted light. We present, then, the images of the SHG from the microspheres both in the real and in the Fourier plane and discuss different properties of the emitted light, such as the nonlinear speckle and the dependency on the input polarization. Furthermore, we show the linear dependency of the SHG on the volume of the spheres, which is one of the fingerprint of random quasi-phase-matching even though it was never shown from sample with spherical geometry. To highlight the effect of the Mie modes in the spheres, we measure the SHG sweeping the pump wavelength; we emphasize the broadband emission and the modulation given by the resonances of the pump in the assembly. To conclude, we adapt the model of the random walk to include resonances and we use it to study the efficiency of the random quasi-phase-matched SHG in comparison with perfect phase-matching and quasi-phase-matching for crystals of the same size using the code described in Appendix A. The results

presented in this chapter are based on [106].

## 4.1 State of the art

Well-ordered noncentrosymmetric crystals are widely used to generate coherent light at frequencies at which laser light is unavailable [9]. In fact, thanks to the high coefficients of the  $\chi^{(2)}$  tensor, they allow for efficient three-wave mixing such as second-harmonic generation and spontaneous parametric down-conversion [126]. These light sources have numerous applications in a wide range of fields including spectroscopy [54], bioimaging [127][128], and ultrafast optics [35]. More recently, noncentrosymmetric crystals became one of the leading materials for the generation quantum states of light [129–131]. To generate efficiently light at new wavelengths the pure crystals have to be properly handled. In fact, the emission is efficient only if the new waves generated by the different atoms in the crystal interfere constructively. These constraints are known as phase-matching conditions and they are a consequence of momentum conservation. The phase-matching control is usually achieved by perfect phase-matching in birefringent crystals [132], quasi-phase-matching in periodically poled crystals [133], or through modal phase-matching in waveguides [134]. All of these phase-matching schemes require the control of the temperature as well as the polarization of the pump. Most importantly, by fulfilling these conditions the resulting device has wavelength-dependent performances. In practice, if we change the pump wavelength, we would need to change the angle of the birefringent bulk crystal to maintain the phase matching (and for certain crystals there might be no angle that solves the problem). For quasi-phase-matching and modal phase-matching there is no flexibility at all since the sample is fabricated to target a single wavelength of operation. High-order crystals are therefore not the ideal platform for broadband or widely tunable applications. For these reasons, solutions that relied on a different mechanism were investigated [11]. One viable strategy is to employ a crystal smaller than the coherence length and boost its emission by coupling it to a dielectric or a plasmonic resonator [100, 135–137]. In all these cases however, the optimization of the nonlinear generation relies on a resonant mechanism, which usually provides wavelength-specific performances that hampers the use of  $\chi^{(2)}$  sub-coherence length monocrystals for widely tunable applications.

The approach that we discuss in this thesis is very different, it exploits the disorder of a random distribution of  $\chi^{(2)}$  crystals to generate second-harmonic light. As was proposed by Baudrier-Raybaut *et al.* [39], a polycrystalline disordered material, with single-crystal domains with random orientation, random shape and random size can be used as a platform. Thanks to the disorder, the nonlinear light generated in each domain interferes with a random phase. This process is, counterintuitively, non-destructive, but gives rise

to a global signal that scales linearly with the number of domains. This approach is called random quasi-phase-matching (RQPM) and was also theoretically studied by Morozov *et al.* [138] (which called it stochastic quasi-phase-matching). So far RQPM has been realized mostly in disordered polycrystals with domains with the typical sizes of tens of microns. Based on these transparent polycrystals it was possible to fabricate polycrystalline lasers [40], and disordered optical parametric oscillators (OPOs) [41]. In a conventional OPO there is a bulk crystal in a cavity and, if a new emitted wavelength is targeted, then the full cavity and the crystals need to be reoriented (or require a temperature change). This results in bulky and expensive OPOs. On the contrary, an OPO based on a disordered polycrystal can reduce the complexity of the device, removing the phase-matching constraints. The benefits of the frequency conversion in random structures are in the wide bandwidth and the reduced costs of fabrication. On the other side, the efficiency is, in many implementations, much lower compared to bulk or periodically poled crystal (see Section 4.4.1). In this thesis we explore the advantages of the random quasi-phase-matching and we present ideas to compensate the drawback of a lower efficiency.

It is important to note that, in all the parts discussed until here, we considered random quasi-phase-matching with negligible scattering from the domains. However, when we study the interaction of light with disordered materials, scattering is an ubiquitous phenomenon, in particular when the sizes of the crystalline domains are comparable to the pump and second-harmonic wavelength. In fact, it has been known at least since the seminal work of Kurtz and Perry [88] that grinded nonlinear crystals could generate SHG in the presence of scattering. In this chapter we focus only on random quasi-phase-matching in transparent disordered crystals. The combination of disordered nonlinear crystals and scattering is addressed in detail in the next Chapter 5.

## 4.2 Linear effective medium Mie scattering

The linear measurements on the assembled microspheres of BaTiO<sub>3</sub> nanocrystals (see Subsection 3.3.1) are performed with an upright microscope adapted to do spectral measurements. The samples are illuminated with a halogen lamp and the light is collected both in reflection and transmission by a 50X objective (Zeiss EC Epiplan Aphocromat, NA=0.95) with a collection angle of 72°. The microscope allows for both bright-field and dark-field illumination. Part of the collected light is divided by a beam splitter onto a CMOS camera and into an optical fiber. The fiber then guides the light into a spectrometer (*Shamrock, Andor*). We filtered the pump to allow only red-near-infrared light on the sample (RNI) or blue-green (BG) light, the spectra of the source are shown in the inset of Fig. 4.1. From the images in transmission we can see that the microspheres of different sizes focus the light in a small spot, and this happens both for the BG and the RNI spectral region. This focusing on the rear part of the microsphere is the photonic nanojet discussed in Chapter 2. Effectively our microspheres behave as microlenses, the light is

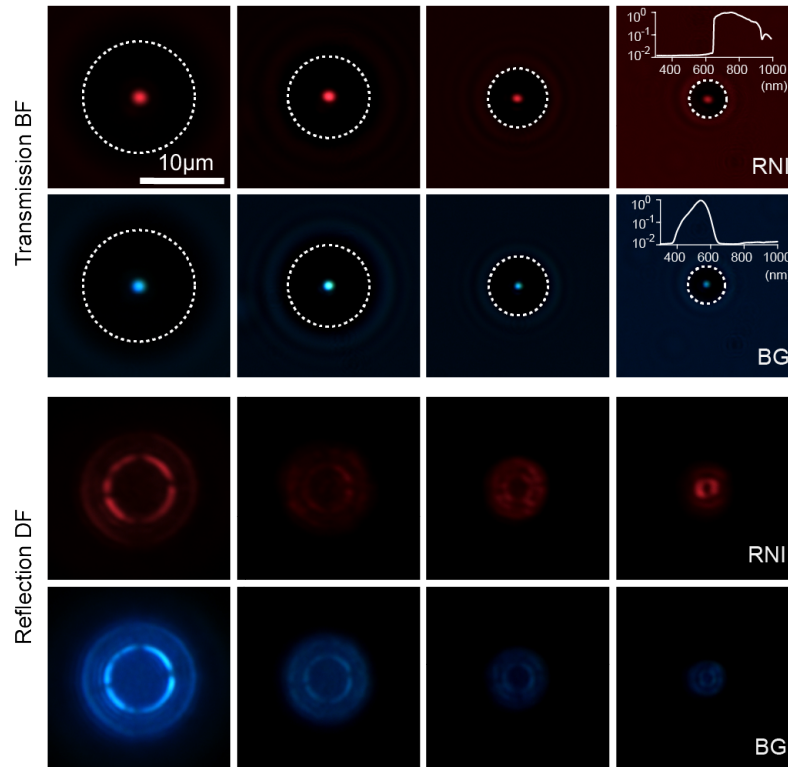


FIGURE 4.1: True color microscopy images of assembled microspheres with diameters in the range  $3 \mu\text{m}$  to  $12 \mu\text{m}$  under red-near-infrared (RNI) or blue-green (BG) illumination. The illumination is constituted by a halogen lamp with a colored filter. The spectra of the illumination is displayed in the inset. The same 4 microspheres are measured both in transmission and bright-field (BF) and reflection dark-field (DF). In transmission it is possible to see a strong focusing of the light in a small central spot, a phenomenon called photonic nanojet. In reflection the microsphere create an image of the illumination cone. The blue part of the spectrum is scattered more than the red by the nanoparticles in the spheres, which gives a brighter blue color compared to the red halo. Image adapted from [106].

not diffused and the spheres look very transparent. This constitutes an indirect evidence that the fabrication is able to assemble very homogeneous spheres that interact with the light as an homogeneous medium. The images of Fig. 4.1 in reflection show a very distinctive ring for every size in the range, which stems from the cone of the illumination of the dark-field microscope. In practice the assemblies create an image of the source of the illumination. The only qualitative difference that can be seen between the BG and the RNI illumination comes from a slightly more pronounced halo for the blue part of the spectrum. This can be attributed to a weak Rayleigh scattering from the nanoparticles that constitutes the microspheres. In fact, it is expected that the blue part of the spectrum is scattered more by particles of 50 nm in diameter. To test if the microspheres could be modeled by Mie theory, we measured the wavelength-dependent scattering cross section under white light illumination. The results are displayed for two different spheres of diameter 0.8  $\mu\text{m}$  and 3.2  $\mu\text{m}$  in Fig. 4.2. The experimental curves are plotted in red and blue. We can see the distinctive peaks of the Mie resonances in the normalized scattering cross section. These peaks tell us that the light interact with the microsphere as if it were a uniform medium. The measured spectra were normalized with the following:

$$\sigma(\lambda) = \frac{\sigma(\lambda)_{\text{meas}} - \sigma(\lambda)_{\text{BG}}}{\sigma(\lambda)_{\text{Illum}} - \sigma(\lambda)_{\text{DC}}} \quad (4.1)$$

where  $\sigma(\lambda)_{\text{meas}}$  is the scattering from the micro-sphere,  $\sigma(\lambda)_{\text{BG}}$  is the background (measured as the light scattered in an empty area near the micro-sphere),  $\sigma(\lambda)_{\text{Illum}}$  is the illumination and  $\sigma(\lambda)_{\text{DC}}$  are the dark counts. In the reflection configuration,  $\sigma(\lambda)_{\text{Illum}}$  was measured as the spectrum of the light reflected by a thick Teflon diffuser (99% reflectivity). In the transmission configuration,  $\sigma(\lambda)_{\text{Illum}}$  was measured as the spectrum of the background in a completely dark environment. To show that these modes indeed come from the spherical geometry, we calculated the scattering cross section as it was done in Chapter 2 of spheres of the same size with an effective refractive index given by the Maxwell-Garnett rule. We called this model effective medium Mie (EMM) theory. Thanks to this model, we could plot the theoretical curves in Fig. 4.2. The estimate effective refractive index is  $n_{\text{eff}} \approx 1.55$ . While in the RNI part of the spectrum the agreement supports the Mie description, in the BG wavelength range the Rayleigh scattering starts to affect the measurements, giving a flatter spectral response. However, we note that there is a good qualitative agreement between the experiment and the analytical calculation.

### 4.2.1 Analytical model and FEM simulations

To further test our analytical EMM theory we performed finite element simulations with COMSOL. We calculated both in the simulation and in the EMM model the same microsphere with effective refractive index  $n_{\text{eff}} = 1.6$ . The benefit of using the simulation is the possibility to include the substrate. In fact, experimentally we measure the spheres on a glass substrate and not in



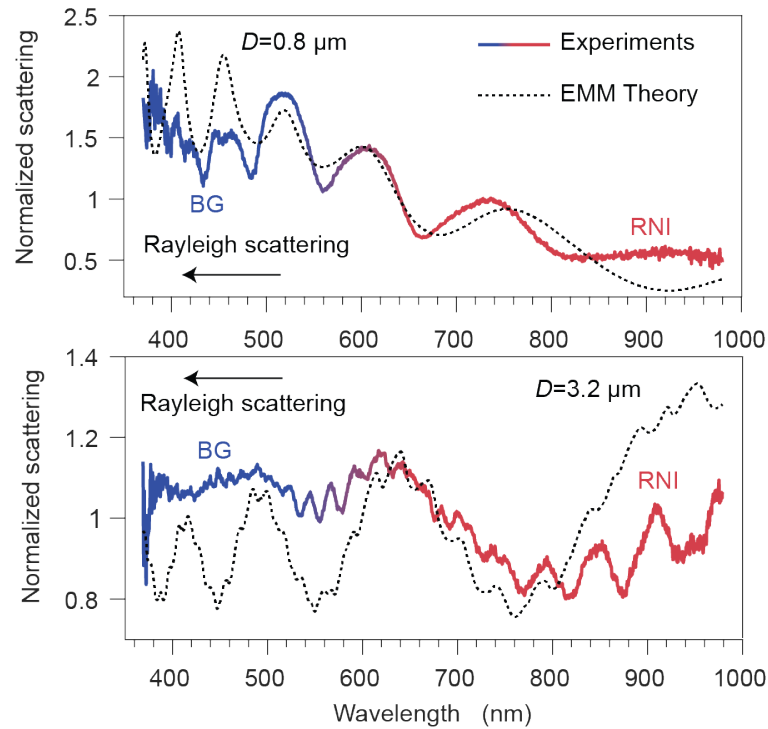


FIGURE 4.2: Normalized scattering cross section of the microspheres of diameter  $0.8 \mu\text{m}$  and  $3.2 \mu\text{m}$ . In red-blue it is plotted the experimental result, in dashed gray the effective medium Mie model which matches the modes. The measurements are obtained in dark-field (DF). The filling fraction theoretical plot is 52% for the smaller one and 55% for the bigger. The imaginary part of the refractive index  $k=0.003$  for the microspheres. The agreement in the BG part of the spectrum is worsened by Rayleigh scattering which affect the Mie modes in the sphere. Image adapted from [106].

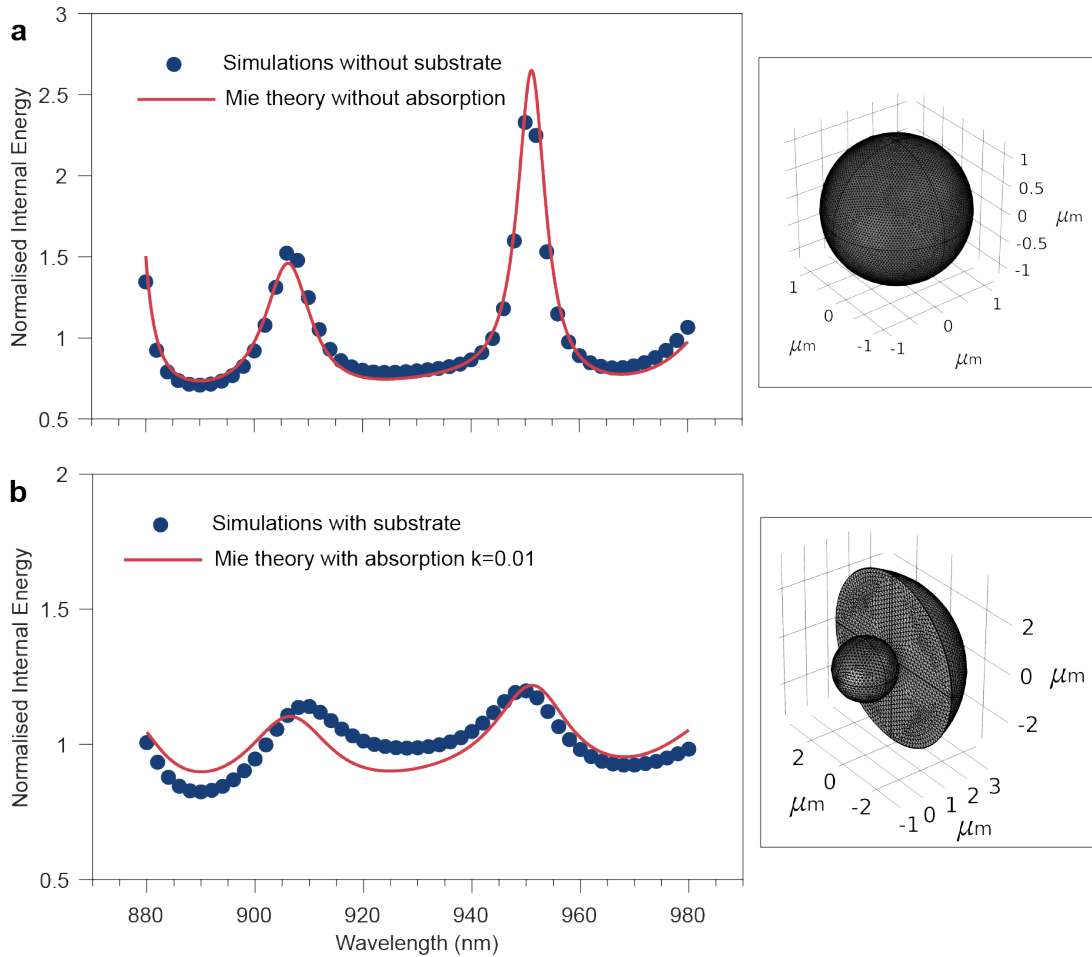


FIGURE 4.3: Comparison between the normalized internal energy with the EMM model and the COMSOL simulation. The calculations are done for a microsphere of  $1.2 \mu\text{m}$  radius and  $n_{eff} = 1.6$ . The energy is normalized to the same volume without the Mie modes. a) Internal energy for the microsphere in air with no substrate, we can see that the results match. b) Internal energy for the same microsphere simulated with a glass substrate. In the case of EMM model it is not possible to insert the substrate as it is done in COMSOL. However, we can mimic the losses by artificially increasing the imaginary part of the refractive index. This generates good agreement in terms of positions of the peaks and quality factor of the modes.

vacuum. This substrate heavily affects the measurements given that the refractive index contrast between the samples ( $\approx 1.6$ ) and the glass substrate ( $\approx 1.5$ ) is small. We expect, therefore, that the substrate modifies the mode in the spheres and that it is responsible for the out-coupling of some energy, effectively inserting losses into the system. The simulated and computed internal energy for the microspheres for different wavelengths are represented in Fig. 4.3. First we check that, in absence of the substrate, the results coincide. It is worth to point out that the analytical calculation with EMM model is fast and allows to sweep the wavelength range with a very fine step keeping the computation time in the orders of minutes. This is not the case for the COMSOL simulation that was computed for less dense values. The absorption coefficient of BaTiO<sub>3</sub> in the displayed wavelength range is of the order of  $k = 10^{-5}$ . The comparison in Fig. 4.3b is more interesting. From the simulation we see that the presence of the substrate indeed lowers the quality factor of the modes. Moreover, it induces a tiny shift, which can be expected considering the microsphere and the substrate as two coupled resonators. In the EMM model we can mimic these losses with the imaginary part of the refractive index  $k$ , i.e. inserting artificial losses in the system. This model can reproduce the results in terms of Q factor and roughly match the position of the peaks. This comparison shows that the EMM mode can reproduce the results of the simulation of the internal energy.

The COMSOL simulation are also compared to the linear optical images obtained using the setup depicted in Fig. 4.5 without filtering the fundamental at 930 nm. In Fig. 4.4 we can see for both the sizes ( $0.8 \mu\text{m}$  and  $3.2 \mu\text{m}$ ) that the simulated mode matches the experimental one. Moreover the optical modes are in agreement to the analytical calculation presented in Fig. 2.4. Our bottom-up assemblies interact with the light as homogeneous media and the scattering cross section and the internal energy density can be computed with our EMM model. This is further supported by the close correspondence that both the analytical model and the simulation with COMSOL have with the linear measurements.

### 4.3 Nonlinear generation from the BaTiO<sub>3</sub> microspheres

The setup used to perform the nonlinear measurements of the BaTiO<sub>3</sub> microspheres is shown in Fig. 4.5. The source is a Titanium-Sapphire pulsed laser (Spectra-Physics MaiTai HP) with pulse width of 120 fs at the output of the laser and a repetition rate of 80 MHz. The wavelength can be tuned in the range of 690 nm to 1040 nm with an average power that can exceed 1 W. We used this set-up to measure the second-harmonic light from the microspheres. To give evidence that the collected signal is indeed second-harmonic generation (and, for example, to exclude the presence of significative fluorescence from the assemblies) we measured both the spectra and the power scaling. These measurements are displayed in Fig. 4.6 and confirm that the detected light is SHG. We measured the SHG from a microspheres

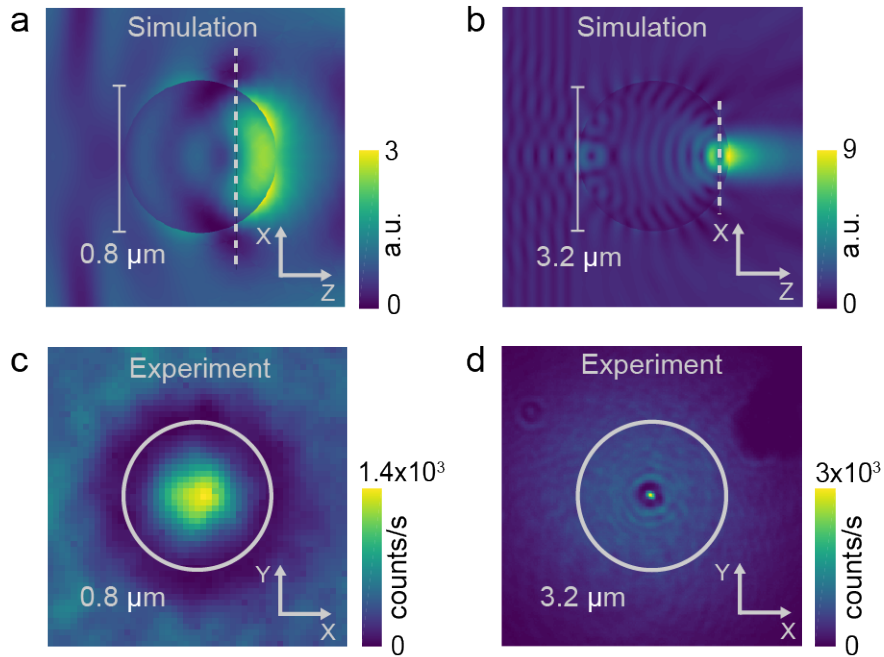


FIGURE 4.4: Finite element method simulation using the effective medium approximation of the internal energy density of microspheres with matching optical measurement. The simulation of the modes is obtained for a plane wave of wavelength of 930 nm coming from the left. a,b) COMSOL simulation of a microsphere of size 0.8 μm and of size 3.2 μm. The field is concentrated on the rear part of the sphere, for the bigger sphere we see that the formation of the nanojet is more pronounced (see Fig. 2.4) for a comparison. c,d) Experimental image of the rear plane of the microspheres of size 0.8 μm and of size 3.2 μm illuminated with laser light at 930 nm. Image adapted from [106].

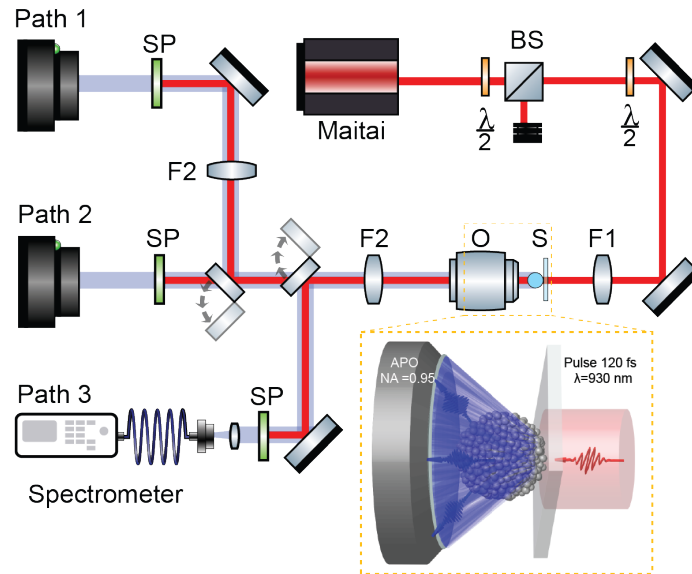


FIGURE 4.5: Schematic of the setup used to do the nonlinear optical characterization of the microspheres. The pump power at 930 nm is controlled with a  $\frac{\lambda}{2}$  half-wave plate and a polarizing beam splitter (BS). After that, the polarization is controlled by a second  $\frac{\lambda}{2}$  wave plate. The beam is then focused with lens (F1) of focal distance 75 mm on the sample (S). The pump and the second harmonic are then collected by an objective and imaged sent to three different path to do Fourier plane imaging (Path 1), real plane imaging (Path 2), and spectrometry. When measuring the second-harmonic the pump at 930 nm was filtered with short-pass filter (SP-BG39). In the inset there is a zoomed representation of the pump impinging on the microsphere and the disordered SHG at 465 nm collected by the wide numerical aperture objective. Image adapted from [106].

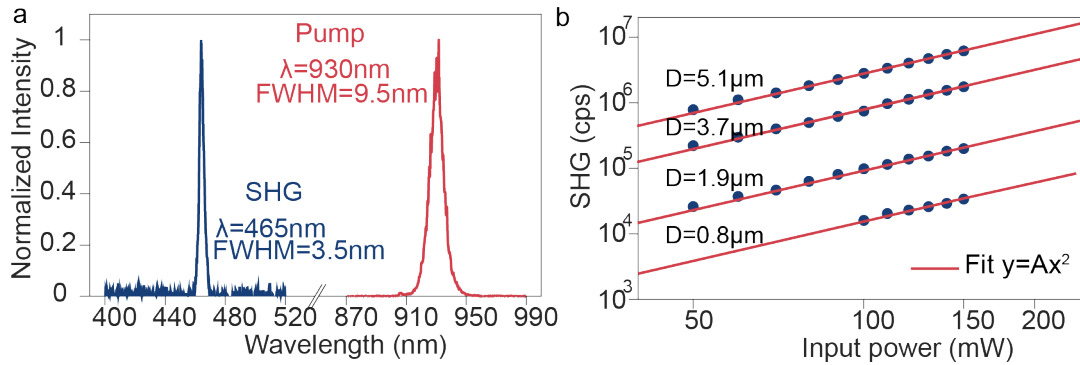


FIGURE 4.6: Second-harmonic generatino measurement from the BaTiO<sub>3</sub> assembled microspheres. a) Spectrum of the SHG at 465 nm and the pump at 930 nm, not to scale. b) Power scaling of microspheres of different size. The quadratic power scaling gives evidence that the measured light comes from second harmonic generation. The shift on the vertical axis shows that the bigger spheres generate more nonlinear signal than the smaller ones.

of different size. The SEM images of 4 microspheres are displayed in Fig. 4.7a-d. The images of the SHG in Fig. 4.7e-h show that the emission is a speckle pattern. Comparing these images with the linear microscopy ones in Fig. 4.7a-d, we can appreciate an evident contrast. The assemblies presented in Fig. 4.1 are transparent and ordered from the pump view point, and the effective medium model can describe the linear interaction that they have with the laser light. On the contrary, they produce second-harmonic signal stemming from the disorder of the positions, orientations and sizes of the BaTiO<sub>3</sub> nanoparticles. Furthermore, we see that the SHG is stronger from the center of the image as a result of the nanojet of the fundamental. As shown in Fig. 4.7i-l, the measurement of the SHG is emitted over the whole angle 72°. In this k-space the SHG generates another speckle: similarly to the real plane the interference of the random sources is more constructive in some directions and less in others. This fact is evidenced by the alternation of light and dark points in Fig. 4.7i-l. Interestingly for smaller spheres there is more emission at wider angles (i.e. closer to the outer ring in Fig. 4.7i-j). For bigger spheres the speckle in the k-space is more evenly distributed in the emission cone, as reported in Fig. 4.7k-l.

To test further the random quasi-phase-matching SHG from the microspheres, we measured the SHG from a set of 32 assemblies of different diameter in the range of 1  $\mu\text{m}$  to 12  $\mu\text{m}$ . The scaling with the size is reported in Fig. 4.8. The data are displayed with their best fit curves both in semi-logarithmic and logarithmic scale. We can see that the SHG grows linearly with the volume of the assembly, i.e. with number of the BaTiO<sub>3</sub> nano-crystals. This scaling is the predicted trend and has been already measured in polycrystals with micron-size domains and in a planar geometry [39][139][140]. The presented results extend the validity of the linear relation between SHG and volume for a different geometry and even in presence of resonant modes.

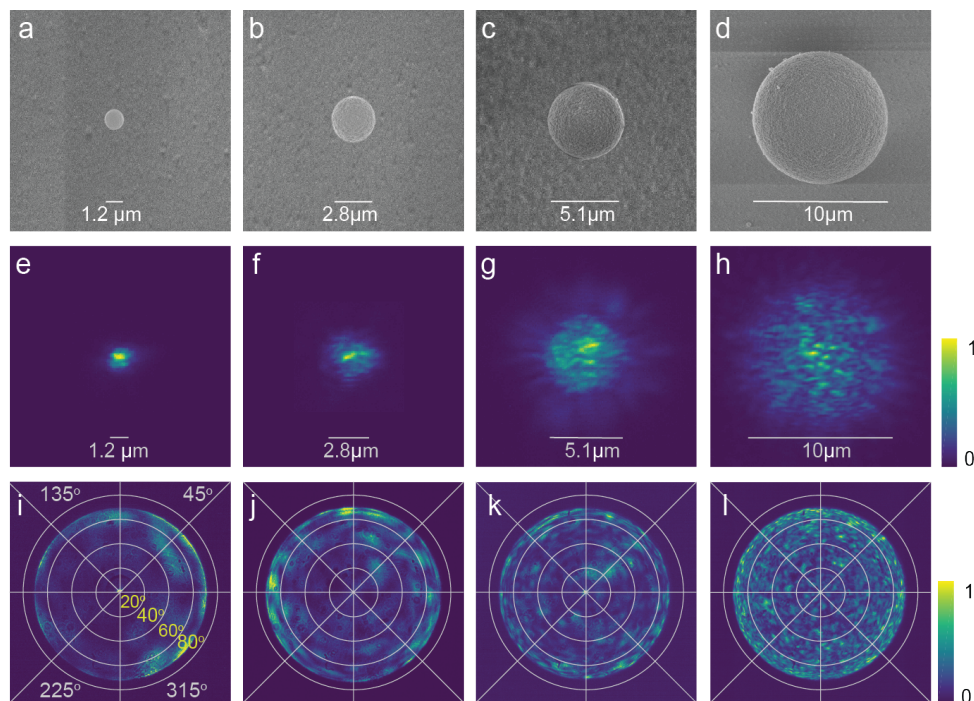


FIGURE 4.7: Measurements of the microspheres. a,d) SEM images of four microspheres with different sizes. e,h) SHG emitted from the microspheres. The signal with spherical geometry is nonlinear speckle. i,m) SHG of the back focal plane of the objective. This measures the  $k$  vectors of the emission, and this is also a nonlinear speckle pattern. Image adapted from [106].

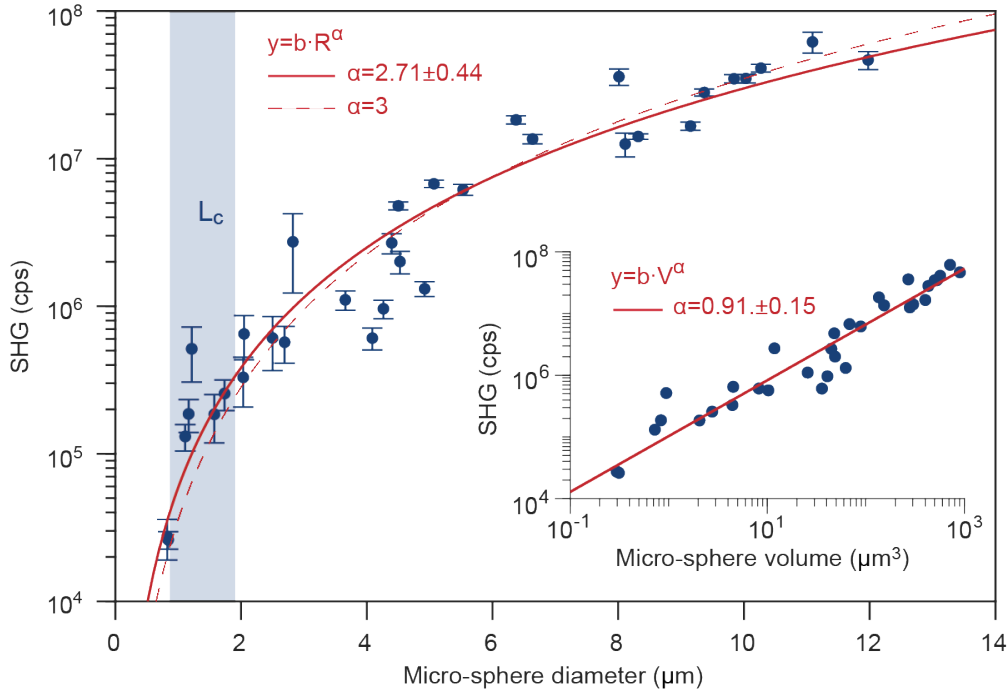


FIGURE 4.8: Measured SHG from 32 microspheres of different diameters, integrated over the speckle. The results are averaged over input polarization and the error bars represents the range of variability of the global SHG with the polarization. In the inset the same data are plotted with the volume, to show the consistent linear trend over four orders of magnitude of volume. Image adapted from [106].

In light blue in the graph it is displayed the coherence length for BaTiO<sub>3</sub> at the pump wavelength of 930 nm. Since BaTiO<sub>3</sub> is birefringent the coherence length is angle dependent and we have to compute  $\Delta k$  for every k-vector (ordinary and extraordinary for both pump and SHG). We computed it thanks to the code detailed in Appendix A. BaTiO<sub>3</sub> is non-phase matchable at 930 nm, i.e. there is no solution angle for which  $\Delta k = 0$ . The angle-dependent coherence length have values in the range 0.95  $\mu\text{m}$  to 1.87  $\mu\text{m}$ . This number is interesting because it tells us that we are working in a range in which every crystalline domain is smaller than the coherence length (i.e. every crystal contributes to generate second-harmonic). At the same time, for microspheres with diameter longer than the coherence length we do not see any decrease in the SHG up to sizes six times greater than the coherence length. By looking carefully at the data, we see that the efficiency of the individual microspheres fluctuates around the purely cubic trend. We attribute this difference to the resonances in the microspheres that drives the SHG emission. The measured efficiency will be investigated further in the Section 4.4.1 of this chapter. Another explanation has to be considered, these different efficiencies can be due to fabrication imperfection since the surface quality of the spheres is not identical for different assemblies and this can result lower emission for some microspheres.



### 4.3.1 Nonlinear Speckle and polarization

Besides the scaling of the SHG with the volume there are other interesting properties of the SHG from the disordered microspheres. For instance, in Fig. 4.9 we show the statistical intensity distribution of the nonlinear speckle for three different microspheres. This plot follows a Rayleigh distribution [67], which stems from the interference of many emitters of randomized positions, orientations and sizes. While the linear speckle from scattering is heavily studied, little is known on this nonlinear speckle of SHG through RQPM. Recently, properties like the speckle correlation with the angle [141], or the intensity-dependent speckle contrast [32] are gaining interest. We acquired also the polar dependency of the SHG by changing the input polarization, reported in Fig. 4.9. The polarplots shape depends on the size of the assembly, as reported in [34]. We can see, bigger microspheres have an almost isotropic response which can be attributed to the averaging between the many sources in the assemblies. At smaller sizes ( $D < 5 \mu\text{m}$ ) there is still a remaining polarization dependence. This phenomenon is a result of the averaging with a smaller number of sources. To provide more insights on the polar dependency we combined the COMSOL simulation as in Fig. 4.4, to export the intensity distribution of the pump in the microsphere. The distribution of the fundamental E-field in the micro-spheres (blue) and the same distribution weighted with the square of the fundamental power ( $E^4$ ) (orange) are reported in Fig. 4.9. They are called electric field enhancement because they are compared to the electric field of the pump field impinging on the microsphere (plane wave). The fourth power of the E-field enhancement represents the contribution to the total SHG power from grains with a specific enhancement ( $I_{2\omega} \propto I^2(\omega) \propto E^4(\omega)$ ). This skewed distribution shows that a small portion of the grains (grains in the nanojet, with high E-field enhancements) contribute significantly to the total SHG. We quantified this effect by determining how many grains on average positioned where the pump is focused in the microsphere contribute to 50% of the total emission (P50). For the reported case of a sphere of  $1.2 \mu\text{m}$  of diameter, only 170 grains of average diameter of 50 nm generate half of the SHG. We calculated this for a cuboid of 170 grains with random orientation with the code in Appendix A, for two different realization of disorder, showing that in that case the SHG is not randomized enough in the sample and still have a clear polar response.

## 4.4 SHG coupled with the Mie resonances

To investigate the influence of the Mie modes on the SHG, we measured the nonlinear light from microspheres of different diameters sweeping the pump wavelength over 100 nm around a central wavelength 930 nm. The measurements give evidence that the SHG with the random quasi-phase-matching is broadband. The data plotted in Fig. 4.10 show that the SHG is modulated in the explored range. We attributed these peaks to the Mie modes, in that the internal energy of the microsphere changes for different wavelengths. To test

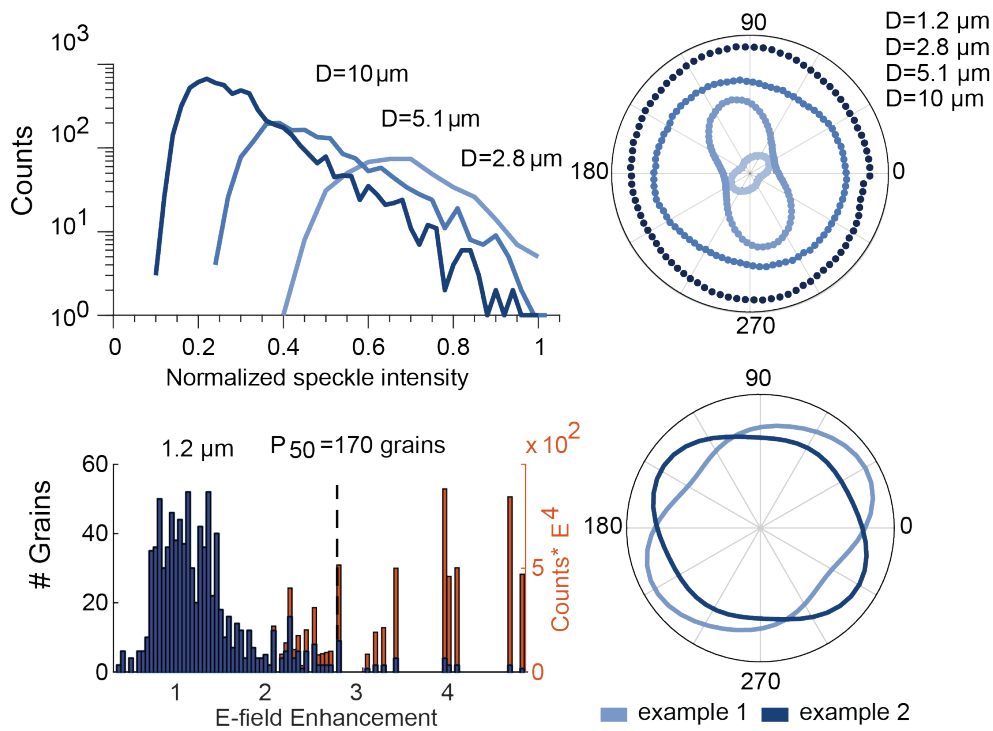


FIGURE 4.9: Statistical intensity distribution of the nonlinear speckles. SHG counts integrated over the whole image (speckle) for different input polarization. Smaller spheres have a polar dependency while the emission of the bigger assemblies is isotropic. Distribution of the fundamental electric field enhancement in the microsphere (blue). The same distribution weighted with the electric field enhancement at the power 4 (in red). Simulated polar plot of two different assembly with the same number of grains equals to P50, summed each point with their mean.

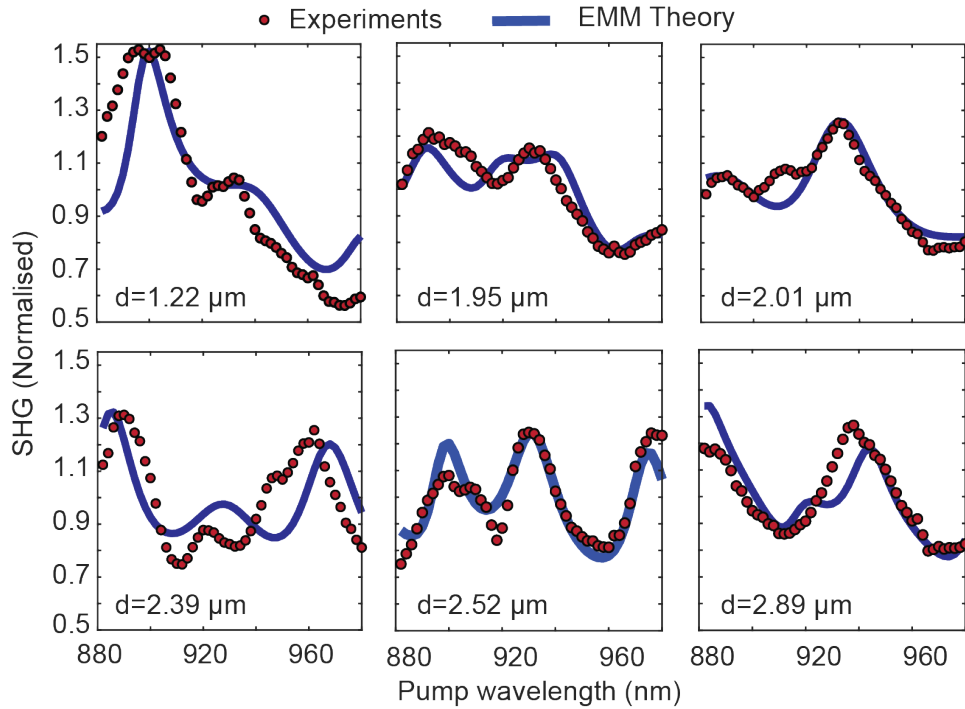


FIGURE 4.10: SHG measured on six microspheres of different sizes. The experimental data are normalized with the transmission of the setup and the quantum efficiency of the camera. The peaks obtained through EMM theory match the experiments with  $n_{eff}$  around 0.55 and  $k$  between 0.001 and 0.01. Image adapted from [106].

this hypothesis, we fitted the experimental data with the analytical calculation of the internal energy with Mie theory. We optimized with two parameters, the filling fraction, which regulates the effective refractive index of the assembly, and the imaginary part of the refractive index that (as explained in Section 4.2.1) controls the losses. For every result we found a correspondence from EMM theory that could explain the modulation. The quality factor of the modes is modest, similar to what was obtained through the COMSOL simulation in Fig. 4.4, however provides a consistent explanation of the observed emission. The agreement with the EMM modes is not perfect, and we attribute this to the artifact introduced by using a complex part of the refractive index to mimic the losses from the substrate. For spheres of diameter bigger than  $3 \mu\text{m}$  the model loses progressively its validity due to the aforementioned reason or because the Rayleigh scattering plays a non-negligible role.

It is possible to extend the model of the random walk in the complex plane that we introduced in Section 2.4, to explain how the random quasi-phase-matched emission can be coupled with modes. The resonant modes in the microspheres can enhance the emission from a single domain in the assembly. This can happen for two reasons. The first mechanism is the focusing of the fundamental; we already explained that the microspheres behave as microlenses and focus the fundamental in the nanojet area. Therefore, the grains

in that area are pumped with higher intensity and generate more second harmonic compared to the case of a non-resonant system. Since the generation of SHG is quadratically proportional to the intensity of the pump, this results in a net enhancement. A second mechanism of enhancement can arise from the Purcell factor (most likely it has an influence only with the small spheres). A nanodomain will emit more efficiently if its emission is coupled to a mode of the second harmonic in the microsphere.

We can explain the resonant enhancement of the SHG upgrading the random walk model. If we consider a 1D disordered array of  $N$  poly-dispersed crystalline domains with random orientations, as sketched in Fig. 4.11. The SHG field at the end of the array is given by the sum of the SHG generated in each domain. This can be represented by the sum of  $N$  phasors, whose phase and amplitude depend on the disorder configuration, as expressed in Eq. 4.2. The SHG amplitude from each grain expressed is here concisely represented by  $A_i$ . We highlight the dependence of the amplitudes on the randomly distributed lengths  $L_i$  and orientations  $s_i$  of the domains. The phase terms are assumed to be randomly distributed in  $[0, 2\pi]$ .

$$E_{\text{SHG}} = \sum_i^N A(L_i, s_i) e^{i\phi_i} \quad (4.2)$$

Eq. 4.2 describes a random walk in the complex plane of the SHG field. Accordingly, the SHG intensity is given by the mean square displacement (MSD) of this random walk  $I_{\text{SHG}} = \langle (\sum_i^N A(L_i, s_i) \cdot e^{i\phi_i})^2 \rangle$ , where  $\langle \dots \rangle$  indicates the ensemble averaging. By assuming that all domains are equally illuminated by the pump beam and that there is no correlations between the contributions of the phasors, the MSD grows linearly with the number of steps, such that  $I_{\text{SHG}} \propto N$ , without any particular wavelength-dependent modulation. This is the well known result of the random quasi-phase-matching. Now, we assume that the disordered array can sustain optical modes, both at  $\omega$  and  $2\omega$ . In such a case the specific pattern of the modes defines an inhomogeneous distribution of the pump and of the SHG field, see Fig. 4.11. We assume that the spatial features of the modes evolve on a scale larger than the mean size of the domains (large-scale modes), such that the fields can be considered constant over the single domain.

The modulated fundamental  $E$ -field in each domain is given by:  $\tilde{E}_i(\omega) = F_i(\omega) \cdot E_i(\omega) e^{i\phi_i}$ , with  $E_i(\omega)$  the unmodulated field amplitude,  $\phi_i$  the phase of the fundamental, and  $F_i$  the Mie-enhancement factor. The second-harmonic  $E$ -field of the  $i^{\text{th}}$  domain is:  $E_i(2\omega) = \xi_i \cdot A_i \cdot e^{i\phi_i}$ , with  $A_i \propto E_i(\omega)^2$  the second-harmonic  $E$ -field amplitude generated from the unmodulated field, and  $\phi$  the phase of the SHG. The modulation can be described by a domain-dependent SHG enhancement factor  $\xi_i(\omega, 2\omega) = F_i^2(\omega) F_i(2\omega)$  combining Mie effects of the fundamental as well as the SHG as in an homogeneous nonlinear resonator [142]. Thus, the total SHG  $E$ -field of  $N$  domains is:  $E_{\text{SHG}} = \sum_i^N \xi_i \cdot A_i \cdot e^{i\phi_i}$ . In the ensemble average  $\langle \dots \rangle_{\text{ens}}$  the SHG intensity is therefore given by:

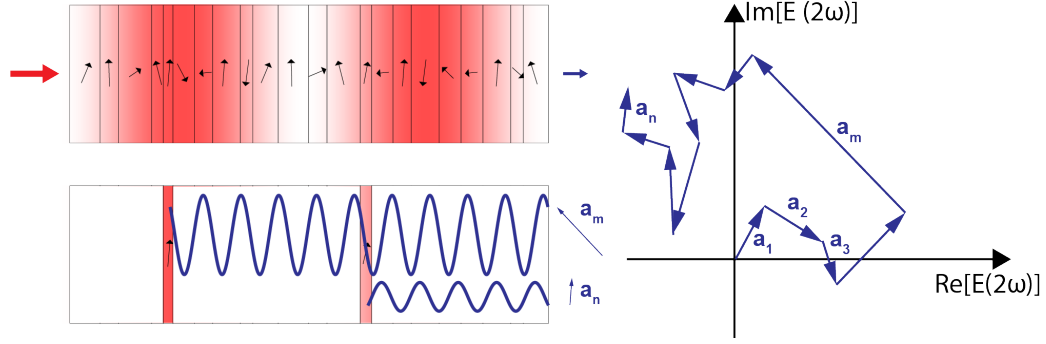


FIGURE 4.11: Sketch of a one-dimensional  $\chi^{(2)}$ -disordered system and effect of an optical mode on the RQPM mechanism. The color modulation within the disordered crystalline stick indicates the intensity distribution of the pump, which here is a  $\sin^2(x)$  as an example. Crystalline domains in a region of high field-enhancement (red) generate a SH-wave with a larger amplitude compared to the others. The corresponding phasors ( $a_m$ ) are longer steps of the random walk in the SH complex plane, which enhance the RQPM generation by increasing the mean square displacement.

$$\langle I_{\text{SHG}} \rangle_{\text{ens}} \propto \langle \left| \sum_i^N \zeta_i A_i e^{i\phi_i} \right|^2 \rangle_{\text{ens}} \quad (4.3)$$

The SHG intensity with a modulated field corresponds to the the mean square displacement of a random walk with a mode-dependent step-length distribution, in which some steps contribute more than others if the corresponding domain is in a high-enhancement region. We consider the standard situation of RQPM, where the system is disordered in the  $\chi^{(2)}$  spatial distribution, but it is homogeneous in the  $\chi^{(1)}$  spatial distribution, i.e. the refractive index. This way, the modes are determined by the geometry and are independent from specific disorder configurations, which means that  $\overline{(\zeta_i^2)}$  can be taken out of the ensemble average. With this in mind we can simplify Eq. 4.3 as follows:

$$\langle I_{\text{SHG}} \rangle_{\text{ens}} \propto \langle |\sum_i^N \tilde{\zeta}_i A_i e^{i\phi_i}|^2 \rangle_{\text{ens}} = \langle \sum (\tilde{\zeta}_i A_i)^2 + 2 \sum_{i \neq j}^N \tilde{\zeta}_i \tilde{\zeta}_j A_i A_j \cos(\phi_i - \phi_j) \rangle_{\text{ens}} \quad (4.4)$$

$$= \langle \sum (\tilde{\zeta}_i A_i)^2 \rangle_{\text{ens}} + \underbrace{\langle 2 \sum_{i \neq j}^N \tilde{\zeta}_i \tilde{\zeta}_j A_i A_j \cos(\phi_i - \phi_j) \rangle_{\text{ens}}}_{= 0 \text{ (interference terms)}} \quad (4.5)$$

$$= \langle \sum (\tilde{\zeta}_i^2 A_i^2) \rangle_{\text{ens}} = \sum (\langle \tilde{\zeta}_i^2 A_i^2 \rangle_{\text{ens}}) = \sum \tilde{\zeta}_i^2 \langle A_i^2 \rangle_{\text{ens}} \quad (4.6)$$

$$\stackrel{\text{approx.}}{=} \overline{(\tilde{\zeta}_i^2)} \sum_i^N \langle A_i^2 \rangle_{\text{ens}} = \overline{(\tilde{\zeta}_i^2)} N \langle A_i^2 \rangle_{\text{ens}} \quad (4.7)$$

We used the approximation  $\sum_i (c_i \cdot X_i) \approx \bar{c}_i \sum_i X_i$ , where  $\bar{c}_i = (\sum_i^N c_i) / N$  denotes the average of all coefficients  $c_i$ . We tested the validity of this approximation numerically for multiple different field distributions of the modes (with finite mean and variance). In the equation above,  $c_i = \tilde{\zeta}_i^2$  and  $X_i = A_i^2$ .

We evaluate the total contribution of the field enhancement as

$$\overline{(\tilde{\zeta}_i^2)} = 1/N \sum_i^N (\tilde{\zeta}_i(\omega, 2\omega)^2) = 1/N \sum_i^N F_i^4(\omega) F_i^2(2\omega) \quad (4.8)$$

We emphasize that this leads to a stronger overall SHG enhancement, when the power is distributed more unevenly within the volume (i.e. stronger focusing of the power into a small region, like the photonic jet). This comes from the fact, that the enhancement factor of the fundamental E-field  $F_i^4(\omega)$  is taken to the fourth power before averaging. The final expression for the SHG intensity is reported in Eq. 4.9

$$I_{\text{SHG}} \propto \overline{(\tilde{\zeta}_i^2)} N \langle A_i^2 \rangle_{\text{ens}} \quad (4.9)$$

We find the expected linear dependence on the number of domains and an additional term  $\overline{(\tilde{\zeta}_i^2)}$  accounting for the resonant enhancement, which is determined by both the internal energy enhancement at the pump wavelength and the spatial distribution of the mode. For our micro-spheres, this calculation is exact for the pump since we have a plane-wave illumination, but it is an approximation for the SHG, since real sources are randomly placed within the sphere.

#### 4.4.1 Efficiency comparison

Using the model developed in the Appendix A we can analyze the SHG emission with the random quasi-phase-matching coupled with Mie modes in comparison to other efficiencies. We can see that we retrieve a linear dependence on the number of grains (i.e. linear with the volume). The results

of the calculations are displayed in Fig. 4.12. We can compare the efficiency of the emission from a microsphere with modes with a sphere with no modes (purely artificial). On top of the modulation, we notice that there is at least an order of magnitude increase for all the sizes. This stems from the increased mean energy and the focusing of the pump power in a very small volume. We see with this indeed the spherical geometry is very effective in increasing the emission. The fact that the assemblies behave as microlenses focuses very tightly the pump resulting in a boost of the nonlinear process. On top of that, there are clear wavelength-dependent peaks. These modes correspond to the ones showed in Fig. 4.10 (Mie modes arise for certain combination of radii and wavelength and sweeping one of the two parameters results in a similar plot). It is useful to compare the gain in efficiency with the emission from a single crystal. As we mentioned previously,  $\text{BaTiO}_3$  is non phasematchable at 930 nm of pump. We computed the second-harmonic emission from a single crystal for two different orientation (one random one the best possible, i.e. longest coherence length). They are displayed with the grey dashed line in Fig. 4.12. We can see that the EEM modes outperform a crystal of the same size at this wavelength. We also compared it with a periodically poled  $\text{BaTiO}_3$  crystal (simulated). This comparison shows that the PP crystal is better than the microsphere for of one order of magnitude and this difference increases with the dimension of the sample. On the other hand this PP crystal is wavelength specific and could not be used with the same efficiency for another wavelength. It is worth to note that the calculation for these Fig. 4.12 were performed with the code in Appendix A, which considers cubes instead of spheres and does not account for the filling fraction. In practice the microspheres contain only 29 % of the material of the cubes.

## 4.5 Summary and perspectives

In this chapter we presented bottom-up assembled microspheres made of  $\text{BaTiO}_3$  nanoparticles. Our assemblies are transparent in the visible and present clearly visible Mie resonances. Interacting with the pump light in the visible range, they display a photonic nanojet and wavelength-dependent modes. We used them as a platform to study the combination of order in the linear interaction with pump light, together with nonlinear effects in a disordered material. Our fabrication on one hand provides nice quality of the linear resonances, on the other, it ensures that individual nanocrystals are randomly oriented in the assemblies. Therefore, our  $\text{BaTiO}_3$  microspheres are disordered only with respect to the nonlinear optical interaction. We studied the peculiar broadband generation of second-harmonic light from the disorder thanks to the random quasi-phase-matching enhanced by the Mie resonances of the spheres. This optimization mechanism for the SHG circumvents the phase-matching conditions and works also at scales larger than the coherence length of the material. We accompanied our findings with an analytical model that combined Mie theory and homogenization theories, as well as a model to compute the SHG from disordered structures to support our results [143]. As can be seen in Fig. 4.8, the presence of the resonances provides an

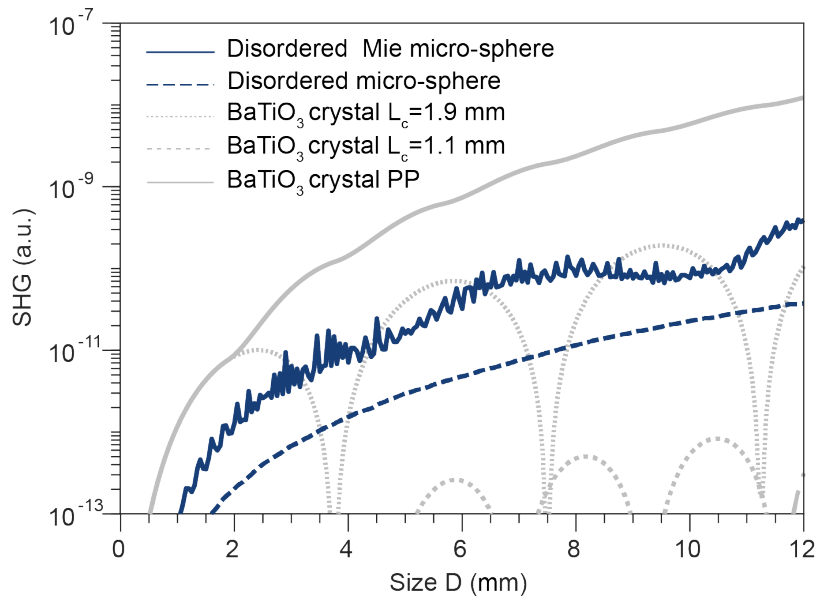


FIGURE 4.12: Numerical comparison of SHG scaling between the disordered microspheres with the Mie modes and different  $\text{BaTiO}_3$  crystalline structure. The blue line is the SHG from our resonant Mie microsphere. The dashed blue line is the SHG from the same sphere removing the contribution of the Mie modes. We can see a wavelength-dependent enhancement constituted by the narrow peaks on top of a broadband enhancement. The grey dashed lines are monocrystals of  $\text{BaTiO}_3$  with a random and the optimal orientation. The solid gray line shows a periodically poled  $\text{BaTiO}_3$ , this is more efficient than the RQPM by roughly one order of magnitude for the considered size range.

Image adapted from [106].



broadband increase of one order of magnitude compared with non-resonant structures. This comes from the photonic nanojet, which enhances the efficiency of the nonlinear generation by focusing in the assembly. Moreover the wavelength-dependent Mie modes produce the small modulation that can be seen in Fig. 4.10.

If we want to consider how to further increase efficiency of our BaTiO<sub>3</sub> microspheres the first issue is represented by the losses due to the outcoupling to the substrate. Employing a substrate with lower refractive index or introducing a spacer could drastically improve the enhancement performances. The other approach is to use bigger nanocrystals, forgoing the resonances and benefiting from a greater efficiency from the individual domains. This comes at the price of introducing scattering and it will be the subject of the next chapter.

This work paves the way to novel research that combines nonlinearity and disorder. For examples, intriguing perspective are unlocked by hierarchically assembling the microspheres into large-scale structures. These suprastructure could display correlation in the positions resulting in a different interplay between order and disorder. The impact that a microfluidic fabrication can have with this structures is still unexplored. Another unexplored application of disordered bottom-up structures is the RQPM to generate disordered quantum sources. In fact, owing the to time-reversal symmetry of the three-wave mixing, it could be possible to use nonlinear disordered materials to generate global spontaneous parametric down-conversion.

## 4.6 Declaration of personal contribution

The results presented in this chapter are published in [106]. The work presented was done by Romolo Savo, Jolanda Müller and me. My contributions were the fabrication of the microspheres and the optical linear and nonlinear measurements. I was also responsible of the FEM simulations, the conceptions and implementation of the effective Mie medium model and the random walk representation of the random quasi-phase-matched SHG.

## Chapter 5

# Multiple scattering and random quasi-phase-matching in $\text{LiNbO}_3$ assemblies

In this chapter we study the linear scattering properties and the second-harmonic generation from bottom-up fabricated assemblies of  $\text{LiNbO}_3$  nanocubes. The fabrication of the assemblies, which consist in slabs and microspheres, is presented in Chapter 3. The goal of this chapter is to investigate the random quasi-phase-matching in presence of strong scattering. There are several motivations to study the combination of second-harmonic generation and scattering in disordered materials. To increase the efficiency of the SHG from disordered materials the simplest approach is, in fact, to increase the size of the nano-domains. Bigger domains, from sub-wavelength size in the previous chapter, to size comparable to the wavelength for this chapter, enhance drastically the efficiency of the SHG, since the efficiency of a single domain scales with its diameter to the power of 6 [144]. This increase of the size introduces scattering in the assemblies, since, as was discussed in Chapter 2, the scattering cross section of a single nanoparticle is maximal when  $\lambda \approx nd$ . Therefore, to increase the efficiency of the SHG in disordered materials we have to understand how random quasi-phase-matching can be combined with scattering. A second motivation to study SHG in multiple scattering materials is constituted by the many applications in bioimaging [145]. Second-harmonic emitting nanoparticles are a useful biomarker used in one of the most studied multiple scattering material, the human tissue [146]. Moreover, recent works have shown that specific cells are able to emit second-harmonic and that it is possible to distinguish between different type of cancer from the polarization dependence of the SHG that the cells emit [147]. In the beginning of the chapter, we present a state of the art of the second-harmonic generation in nonlinear and scattering material. From Kurtz and Perry's seminal work [88] to some reviewed version of their study [148][149]. After that, we describe how we quantified the scattering strength of the disordered material made of  $\text{LiNbO}_3$  nanocubes. To do so, we used slabs made of the  $\text{LiNbO}_3$  nanocubes presented in Chapter 3, since a planar geometry is necessary to interpret the experimental results with diffusion theory. These measurements show that our bottom-up disordered material have a subwavelength transport mean free path. Next, we show the nonlinear measurements on the slabs

of LiNbO<sub>3</sub> and on the microspheres. The nonlinear properties of the individual nanocubes are well studied and their SHG has been proved to be very efficient [100]. The idea is to study RQPM SHG both in planar and spherical geometry to give explicit evidence that the SHG power scales linearly with the the volume even in presence of strong scattering and for different geometries. This result was previously claimed but never presented. This chapter is based on [113].

## 5.1 State of the art

The study of disordered photonic media in which light is multiply scattered is a well established field in optics. Indeed, the behavior of light beams in random materials has numerous interesting physical aspects such as anomalous diffusion [150], Anderson localization [14, 26, 84], and mean path length invariance [151]. On top of that, the knowledge of multiple light scattering can be used to develop new applications from laser sources [152], to novel bio-medical imaging [19]. While the transport of light in scattering material in the linear regime has been more extensively explored, less is known of the light scattering in disordered media composed by nonlinear domains. These nonlinear disordered photonic media (NDPM), composed by a random configuration of noncentrosymmetric crystals, are able to generate coherent light through random quasi-phase-matching. As we discussed in the previous chapter, SHG in disordered media has been investigated in transparent polycrystals which are disordered distribution of non-scattering  $\chi^{(2)}$  domains that generate second-harmonic with random amplitude and phase. The interference of the SHG from the numerous random sources leads to a global SHG, the power of which scales linearly with sample thickness. This linear scaling is a fingerprint of the RQPM, as it is in contrast to the quadratic scaling of phase-matched and quasi-phase-matched crystals. Differently to this scenario, nonlinear disordered photonic media (NDPM) have noncentrosymmetric domains that also scatter the light. The fabrication of such a medium is non-trivial, in that it has to have both nonlinear crystalline domains and high refractive index contrast. The simplest way to produce a NDPM is to grind bulk nonlinear material into powders [153][154], which have to be deposited uniformly on a substrate. Kurtz and Perry first reported a study of the nonlinear emission from grinded powders [88]. They proposed a method to study the nonlinear optical coefficient using SHG, telling which materials could be phase-matched. However, grinding a bulk crystals has two main drawbacks. The first one is that it usually produces grains of tens of microns, which are not very efficient to scatter the light in the visible range. Secondly, grinding usually creates defects and strain in the resulting grains, that can cause undesired sub-band gap absorption. Kurtz and Perry eventually removed the scattering by inserting an index matching liquid in the powder, because the scattering even though was present, was not the focus of their work. Several experiments of SHG from NDPM were performed much more recently on electrochemically etched GaP and GaAs slabs [63,

[155], [156]. This fabrication allowed to create a porous (network-like) structure in the crystals with high nonlinearity and strong scattering, avoiding the problems created by the grinding. In a work from Faez *et al.* [157], they measured SHG from the material and provided a diffusion model to interpret the data. However, they did not display the scaling of the SHG power with the thickness of the slabs. Indeed, to measure SHG scaling, they used multiple samples with increasing thicknesses, which were etched independently, potentially generating different internal structures. This lack of control over the size distribution of crystalline nanodomains may introduce systematic differences in the SHG and scattering properties of the samples. Consequently, there is no explicit demonstration of RQPM scaling for SHG in NDPM, although the effect has been clearly predicted by models combining RQPM and the light diffusion hypothesis. Many other properties have been studied in more recent works, for example the intensity distribution [85], the polarization dependency [34], and the nonlinear speckle pattern [32]. The physics of the NDPM is in many of its aspects not understood, and consequently many of their properties not exploited.

## 5.2 Linear scattering measurements

The linear scattering measurements were performed on the slabs of  $\text{LiNbO}_3$  nanocubes described in Section 3. The quantification of the scattering strength was done by measuring the total transmission as a function of the thickness, and fitting the result using diffusion theory. This procedure, which is quite standard in the field of light propagation in complex media, is possible thanks to the planar geometry of the slabs, which allows for analytical solution of the diffusion equation. The key component of the experimental set-up is the integrating sphere. This device consists of a hollow sphere with internal surfaces coated by a material with high and broadband reflectance. If the sample is placed at the entrance port of an integrating sphere, as it is shown in Fig 5.1a, it is possible to measure the total transmission. All the light transmitted through the sample, in fact, scatters on the inner surface of the sphere and it is collected by a fiber and sent to a detector. By moving the sample laterally, it is possible to measure the total transmission for every point of the sample. In our case, the transmission of our slab is reported in Fig. 5.1b, where we can map the total transmission for different points in of the sample. By matching the map of the transmittance with the thickness obtained by profilometry (Fig. 3.10d) we can have many data points of the transmittance versus the sample thickness. This procedure motivates the fabrication of the slabs illustrated in Fig. 3.10a, that resulted in samples with the thickness slowly varying over the lateral size. We measured the total transmission for different wavelengths, the data reported in Fig. 5.1c is for 930 nm wavelength, and every point is the average over many points with the same thickness.

We can fit the reciprocal of the total transmittance as a function of the thickness with the following Eq. 5.1

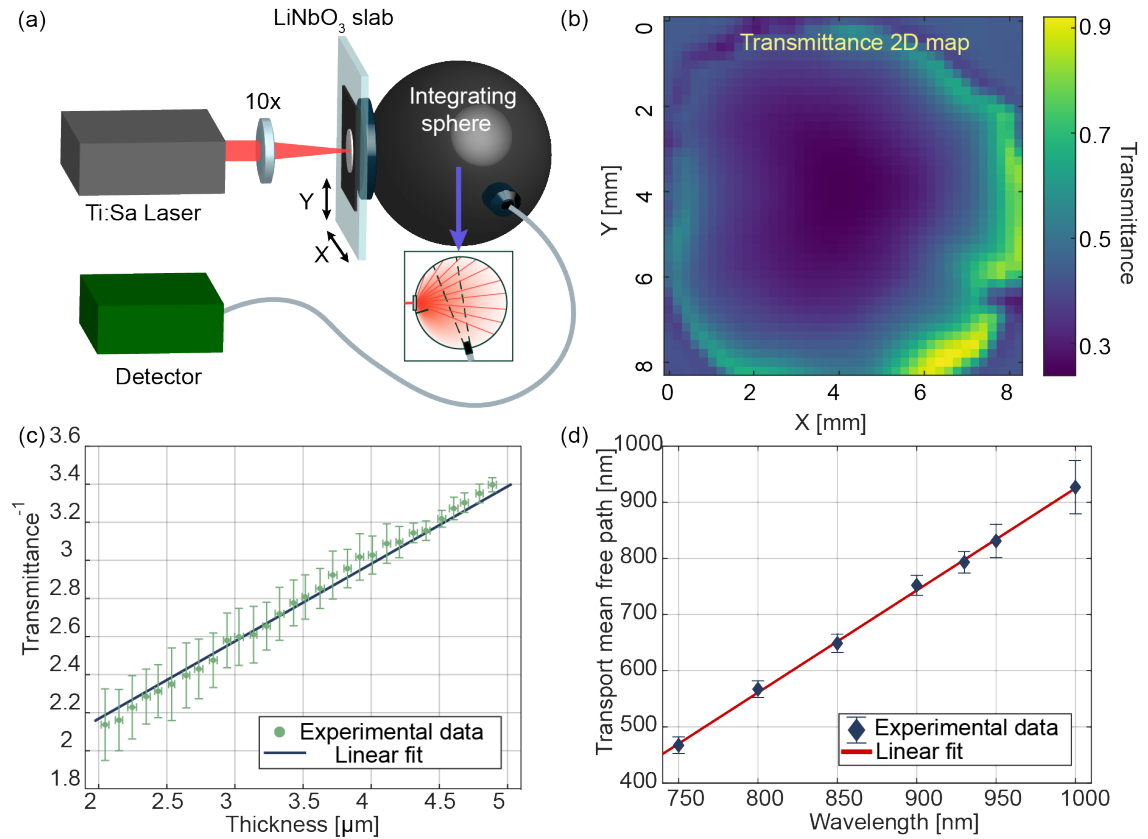


FIGURE 5.1: Characterization of the scattering properties of the slabs. a) Schematic of the setup with the sample placed on motorized stages to access the  $1 \text{ cm}^2$  surface and with an integrating sphere to collect the transmitted light. The inset depicts the working principle of the integrating sphere. b) Measured 2D map of the transmittance measured at 930 nm of pump. c) Reciprocal total transmittance over the thickness with the linear fit, the error bars represent the standard deviation of all the data collected at the same thickness. d) Transport mean free path estimated for different wavelengths between 750 and 1000 nm. Taken from [113].

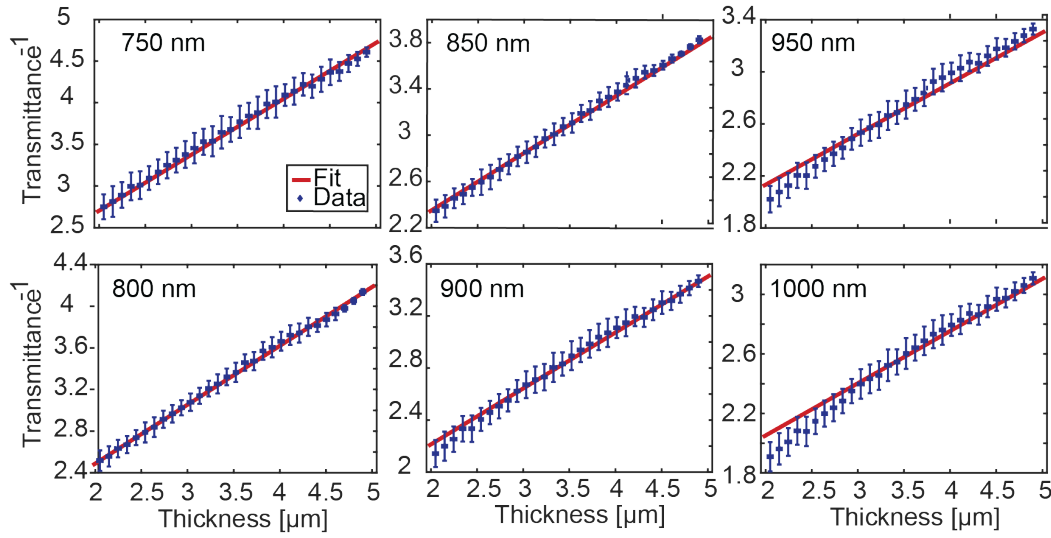


FIGURE 5.2: Inverse transmittance obtained with the integrating sphere for different wavelengths. While lower wavelengths are in optimal agreement with the linear expected from the model, for higher wavelengths a deviation from the trend is appreciable at low thicknesses of the sample. This is due to the fact that  $l^*$  approaches the thickness of the sample reaching the limit of validity of the diffuse approximation.

$$\frac{1}{T(\lambda)} = \frac{1}{\ell^*(\lambda) + z_0(\lambda)}L + \frac{2z_0(\lambda)}{\ell^*(\lambda) + z_0(\lambda)} \quad (5.1)$$

where  $\ell^*(\lambda)$  is the transport mean free path and  $z_0 = \frac{2}{3}\ell^*(\lambda)\frac{1+R_i}{1-R_i}$  is the extrapolation length, and  $L$  the thickness of the slab as defined in chapter 2. From this fitting procedure it is possible to extract the transport mean free path. It is worth to discuss briefly what is the meaning of  $z_0$  and how it is computed. The extrapolation length is the position outside the slab where the light intensity extrapolates to zero. These conditions are imposed to the diffusive Eq. 2.29 outside the system and not at the border, because this would mean that no energy could enter or leave the medium [68]. The specific value of the  $z_0$  is a transport mean free path  $\ell^*(\lambda)$  modified by a number that takes into account the internal reflectivity of the system ( $R_i$ ). The diffusive theory was first applied for transport problems and this correction was not included (for example it was used to calculate the diffusion of neutrons in a nuclear reactor). However, light has a different behavior at the interfaces (for example compared to a neutron). At an interface we have to compute the angle-dependent Fresnel coefficient (the light can impinge on the surface with every angle). This requires to compute the effective refractive index of the material. It is important to specify that in this case the material does not behave as an effective medium and the calculation of the filling fraction to extract  $n_{eff}$  is needed only to compute properly the extrapolation length. The effective refractive index was measured by image analysis and it is reported in Fig. 5.3 The images are acquired with a scanning electron microscope and

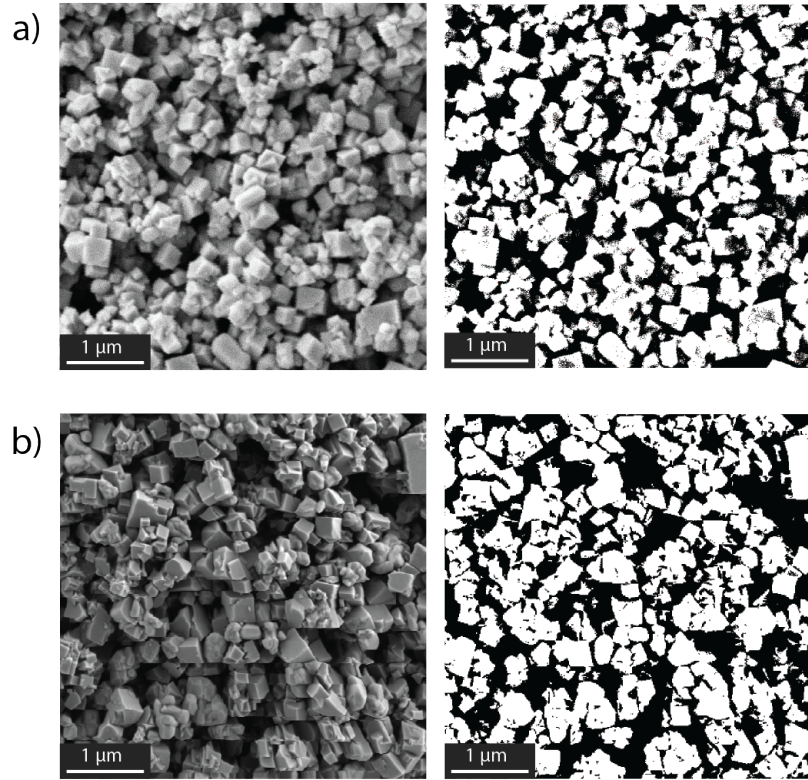


FIGURE 5.3: Scanning electron microscopy image of  $\text{LiNbO}_3$  slabs (a) and microspheres (b) with image binarized to extract the filling fraction.

are binarized through a Matlab function called *imbinarize* which is based on the Otsu thresholding algorithm [119]. The values obtained vary depending on the threshold of the algorithm. The function *imbinarize* allows to control the sensitivity of this modification and we tuned this from 0.5 to 0.7 and took the average filling fraction as the result of our calculation. The final result is  $ff = 52 \pm 4\%$  for the microspheres and  $ff = 55 \pm 5\%$  for the slabs. The numbers obtained were used to calculate the correction factor for the extrapolation length and allowed us to perform a fit with a single free parameter  $l^*$  on the data displayed in Fig. 5.2.

The values of the refractive index and the correction factor for the internal reflection  $A$  are plotted in Fig. 5.4. By fitting all the data in the range 750 nm to 1000 nm, we obtain the values of  $l^*$  reported in Fig. 5.1d and in Table 5.1. For all the measurements,  $l^*$  is subwavelength and shorter than the thickness of the sample. This fact is a confirmation a-posteriori of the validity of the diffusive regime. If we check again the results of Fig. 5.2 at 950 nm and 1000 nm of wavelength, we notice that for small thicknesses (above  $2 \mu\text{m}$ ) the data deviate from the linear trend. This deviation can be attributed to the fact that for those wavelengths the transport mean free path is only twice smaller than the thickness and this condition is at the edge of the validity of diffusion theory (the sample is not optically thick enough). The value of  $l^*$  are of particular interest if we use them to compute the inverse scattering efficiency  $kl^* = 2\pi l^* / \lambda$  (reported in Table 5.1). The smallest value

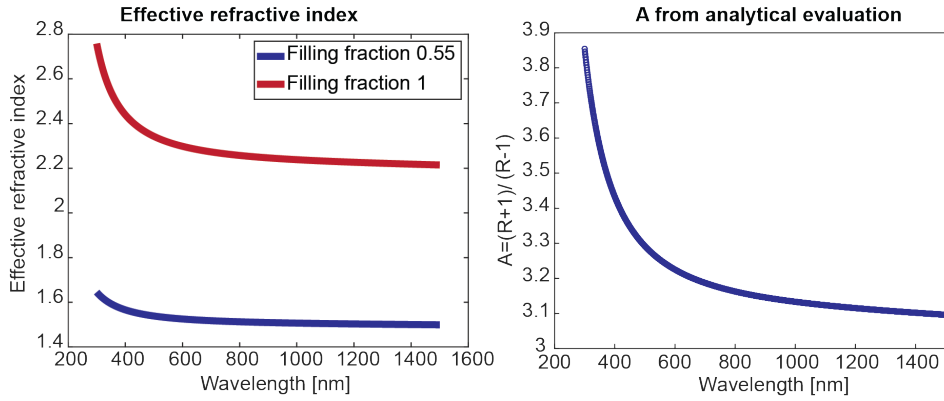


FIGURE 5.4: Effective refractive index computed with the Maxwell-Garnett mixing rule. Correction factor for extrapolation length  $A = \frac{1+R_i}{1-R_i}$ , for an interface of LiNbO<sub>3</sub> with filling fraction 55 % and air. The formula to compute A is taken from [71], [72].

Wavelength [nm]	$\ell^*$ [nm]	$k \cdot \ell^*$
750	$476 \pm 6$	$3.9 \pm 0.1$
800	$567 \pm 7$	$4.4 \pm 0.1$
850	$649 \pm 8$	$4.8 \pm 0.1$
900	$752 \pm 12$	$5.3 \pm 0.1$
930	$788 \pm 14$	$5.4 \pm 0.1$
950	$831 \pm 22$	$5.5 \pm 0.2$
1000	$927 \pm 34$	$5.8 \pm 0.2$

TABLE 5.1: Transport mean free path and inverse scattering coefficient at different pump wavelengths.

reported is  $kl^* = 3.9$  at 750 nm and it is close to the smallest value reported for visible light of 2.6 [63]. On top of that, the value of  $kl^*$  decreases with the wavelength as it is shown by the linear trend of Fig. 5.1d. This decrease suggests that at wavelengths shorter than 750 nm a stronger scattering could be reached. This possibility is permitted by the wide transparency window of the LiNbO<sub>3</sub> that is transparent at least down to 400 nm [90]. Furthermore, the individual nanocubes have scattering resonances in the blue spectral region, as was shown by [100]. Therefore, it could be interesting to investigate the nonlinear response of the the disordered assemblies of the LiNbO<sub>3</sub> nanocubes. They could show values of  $kl^*$  similar or even lower than the lowest reported value of  $kl^* = 2.6$  [63], that can be close to the localization transition.



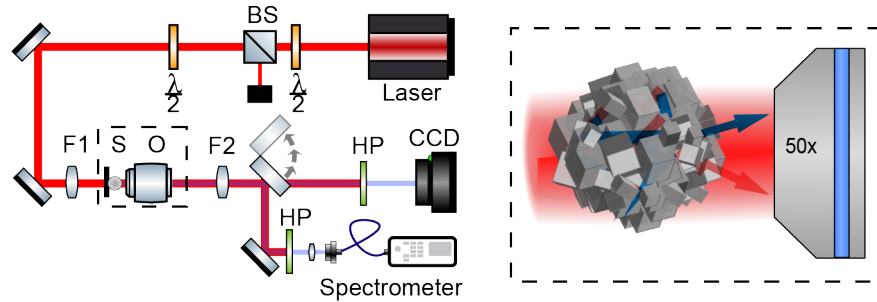


FIGURE 5.5: Nonlinear setup used for the optical characterization of the microspheres. (a) Schematic of the setup used to measure the SHG. (b) Sketch of the fundamental beam scattering in the assembly as well as the second-harmonic signal generated from the disordered nanocubes. Image adapted from [113].

### 5.3 Second-harmonic and scattering trend

We measured the second-harmonic emission from the disordered  $\text{LiNbO}_3$  microspheres with the setup sketched in Fig. 5.5. We illuminated the assemblies with the same laser pulses used for the  $\text{BaTiO}_3$  spheres in Chapter 4 at 930 nm of wavelength, and collected the emitted photons with a 50X Zeiss apochromat objective. The collected light, after the fundamental wavelength is filtered out, can be imaged by a camera or coupled in a spectrometer through a fiber. In the inset of Fig. 5.5 we can see a sketch of the pump light being scattered in the disordered assembly as well as the nonlinear generation in the system. Thanks to the results presented in the previous section, we know that the light at the pump wavelength is undergoing multiple scattering in the assemblies and the trend presented in Fig. 5.1d, suggests that the scattering for the SHG may be even stronger. To confirm that the measured signal is indeed SHG, we measured the scaling of the second-harmonic with the power of the input beam. The data and the quadratic fit for two spheres of different sizes are displayed in Fig. 5.6. This measurement ensures that the signal collect comes indeed from second-harmonic generation and do not arise from fluorescence of defects or impurities in the assembly. The SHG is further confirmed by the spectral measurements displayed in Fig. 5.6.

We performed the nonlinear characterization of the  $\text{LiNbO}_3$  disordered slabs by collecting the SHG with the setup sketched in Fig. 5.5. We measured a 2D map of the transmitted second-harmonic for different positions of the slabs by moving the sample laterally with respect to the impinging laser beam. This measurement produces the intensity map displayed in Fig. 5.7a.

Similarly to the procedure adopted for the linear case, in which we compared the thickness with the total transmission, here we established a one to one correspondence between the thickness and the SHG. This procedure produces a wide set of data points, allowing to average the results over many configurations of disorder. The data are plotted in Fig. 5.7b together with a linear fit with a power law  $y = \beta x^\alpha$ . The fitting procedure returns a value

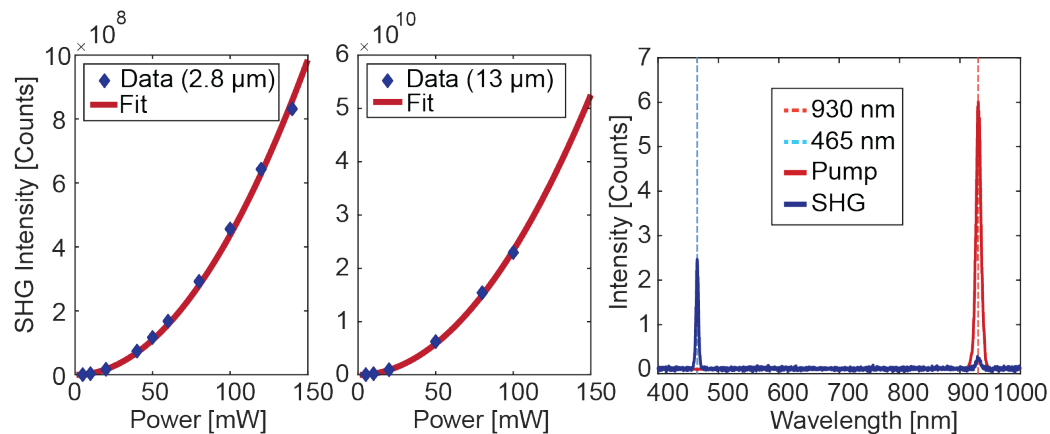


FIGURE 5.6: Nonlinear measurements on  $\text{LiNbO}_3$  assemblies. SHG quadratic scaling with the power of the pump for two different spheres of diameter  $2.8 \mu\text{m}$  and  $13 \mu\text{m}$ . Spectrum of the pump and of the SHG.

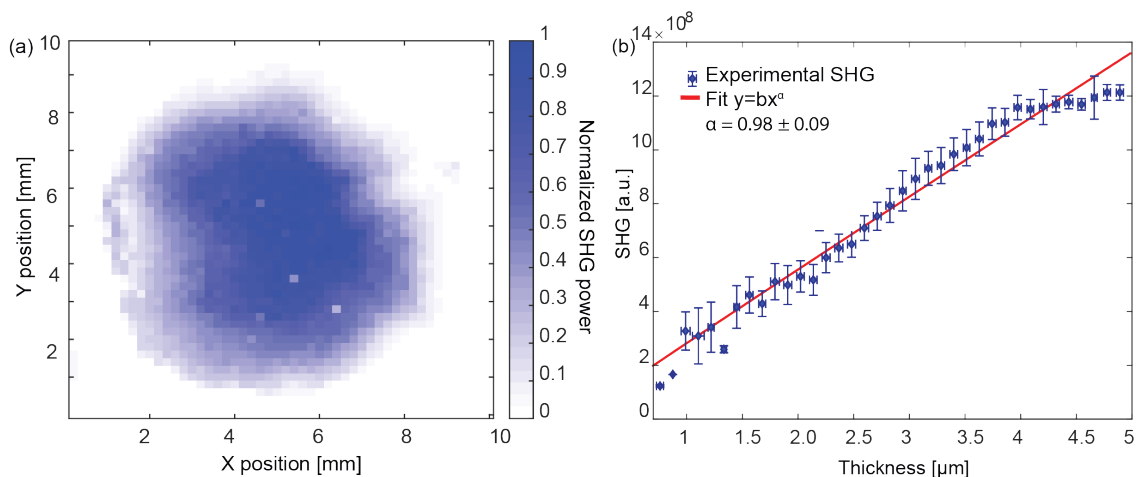


FIGURE 5.7: Second-harmonic generation from a  $\text{LiNbO}_3$  slab. (a) SHG 2D map with a pitch of  $200 \mu\text{m}$ . This ensures that every pixel is independent from the neighbors since the beam waist is around  $30 \mu\text{m}$ . The wavelength used is  $930 \text{ nm}$ . The SHG is more intense from the sample, where the slab is thicker. SHG for different thicknesses. Every point is an average over many measurements of positions of the slabs with same thickness. The error bars quantify the standard deviations of the different SHG produced for comparable thicknesses. The linear trend seems to decrease for samples thicker than  $4 \mu\text{m}$ , this can be due to a progressive redistribution of the emission from the forward transmitted to the backscattered SHG. Image taken from [113].

of  $\alpha = 0.98 \pm 0.3$  which is compatible with a linear trend. This observation agrees with different theoretical results for the SHG in multiple scattering medium that predicts a linear trend with the thickness for both the forward- and the backward-emitted second-harmonic power. This trend is one of the key results of this work because the linearity of the random quasi-phase-matched emission was not explicitly shown in previous studies. The usefulness of our disordered  $\text{LiNbO}_3$  slabs assembled from nanocubes lies in their wide area, that allows to explore numerous configurations of disorder in the same sample knowing the thickness in every point. In many studies it is required to change sample to access different thicknesses and this might introduce sample-to-sample variability, that here is prevented. The fitted linear trend deviates slightly at thicknesses above  $4 \mu\text{m}$ . An explanation for this deviation can be found in the hypothesis of the diffusive model used here. In fact, the conditions of application of the diffusive model are that the transport mean free path has to be much smaller than the thickness of the sample. Here, we have thicknesses spanning from 2 to 10 transport mean free paths, therefore we can be observing a transition between two linear trends which stems from a redistribution between the forward emitted and the backward emitted SHG. It is interesting to note that, while the fundamental is linearly suppressed in the assembly, the SHG grows linearly with the system depth. This apparent contradiction is well explained by [158], where they show that it is a result of the combined effect of the quadratic increase of the SHG with the linear decrease due to scattering. This compensation mechanism can be well understood in the slab geometry, and it is backed up by several theoretical studies, however how the geometry of the sample would affect the scaling of the SHG is still an open question. Indeed, the scaling of the SHG power with the slab thickness, or in general sample volume, is in principle geometry-dependent since the specific distribution and generation of light depend on the sample shape. We tackle this question in the next section with the nonlinear measurements on the  $\text{LiNbO}_3$  disordered spheres.

### 5.3.1 Second-harmonic in disordered $\text{LiNbO}_3$ microspheres

We measured the SHG from the disordered  $\text{LiNbO}_3$  microspheres with the setup depicted in Fig. 5.5. The images of the emission are a nonlinear speckle pattern. A picture of a typical image is reported in Fig. 5.8. Similarly to what we presented for the  $\text{BaTiO}_3$  resonant microspheres, we measured the SHG for assemblies of different sizes. We measured a total of 25 microspheres with diameters in the range  $1 \mu\text{m}$  to  $15 \mu\text{m}$ . The results are shown in Fig. 5.9 both in logarithmic and semi-logarithmic scale. We fitted with the function  $y = \alpha x^\beta$  which results in a best-fit exponent of  $\beta = 2.76 \pm 0.34$ , which corresponds to a linear scaling of the SHG power with the volume of the assembly (i.e., with the number of nanocubes). The show the linear scaling with the volume we plotted it in the inset of Fig. 5.9. The second-harmonic generation in a sphere, in which conventional diffusive equations are challenging to solve due to nontrivial boundary conditions, we retrieve a linear trend of the SHG power versus the volume. This observation demonstrates

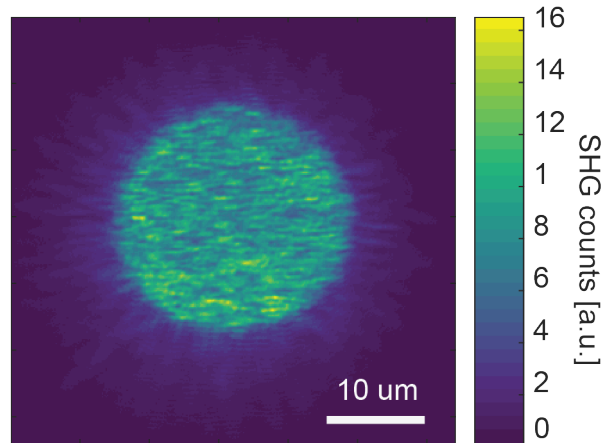


FIGURE 5.8: Second-harmonic speckle of a  $\text{LiNbO}_3$  microsphere.

that the compensation mechanism discussed before for the slab case, that is, that the laterally growing illuminated volume and the continuously attenuated pump power compensate to return the typical scaling of RQPM for transparent media, applies to a larger class of sample geometry. The bigger microspheres (above  $8 \mu\text{m}$ ) slightly deviate from the linear trend similarly to what happens for thick  $\text{LiNbO}_3$  slabs. This deviation can be explained with a partial redistribution from transmitted to backscattered SHG, similarly to the behavior in the slabs. An alternative explanation for the observed deviation could be that the diameter of the microspheres is comparable to the size of the Gaussian profile of the pump beam (FWHM  $18 \mu\text{m}$ ) and, therefore, the bigger microspheres of the data set are illuminated with less average intensity than the smaller ones.

## 5.4 Summary and perspectives

In this chapter we used  $\text{LiNbO}_3$  nanocubes as building blocks to fabricate nonlinear disordered photonic media (NDPM) with slab and spherical geometry. The nanocubes were chosen because it was shown in a previous work that they individually have a high scattering cross section and efficient second-harmonic generation [100]. Both of these effects stemmed from the Mie resonances of the single nanocubes. The initial goal of the fabrication of our bottom-up NDPM, was to produce disordered structures with a high SHG efficiency due to the Mie modes and the higher  $\chi^{(2)}$  tensor of  $\text{LiNbO}_3$  compared to  $\text{BaTiO}_3$ .

We measured the scattering strength of our assemblies, revealing bottom-up NDPM with a very short transport mean free path. In particular, we showed a minimum value of  $l^*$  of  $476 \pm 6$  which corresponds to an inverse scattering coefficient of  $kl^* = 3.9 \pm 0.1$ . This low value makes our assemblies a promising platform to study the combination of nonlinearity and multiple scattering. Moreover, the measured trend in Fig. 6.4d hints to an even lower  $kl^*$  for shorter wavelengths (i.e. stronger scattering), close to regimes in which

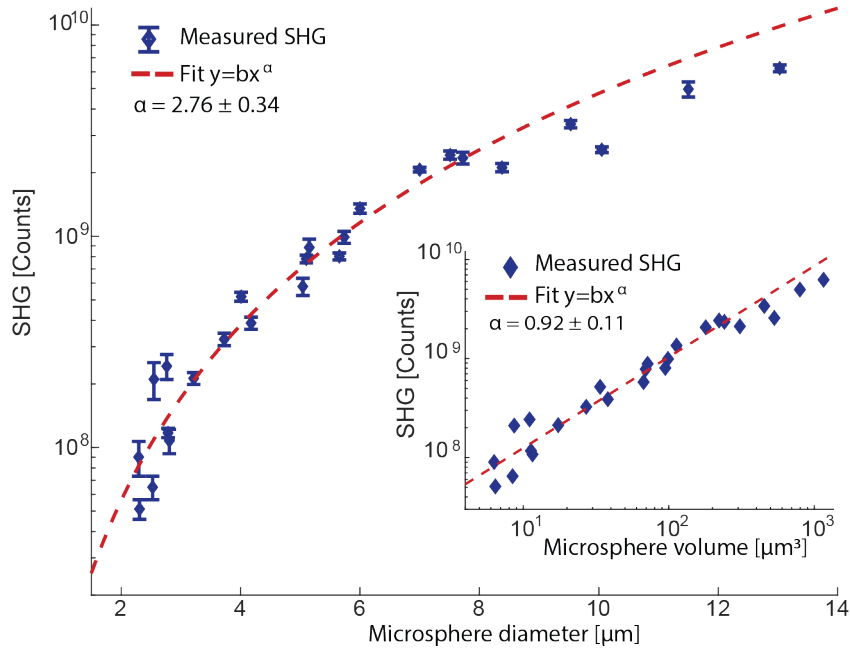


FIGURE 5.9: SHG scaling with the microspheres diameter and data fit with a power law function, proving the linear scaling with the volume, signature of the RQPM regime. Inset: SHG as a function of the microspheres volume, to explicitly show the linear scaling with volume over more than 2 orders of magnitude. Taken from [113].

the diffusion model fails and sign of 3D localization could appear. In order to study this further, an in-depth characterisation of the absorption of assemblies and the creation of thicker samples in which localisation can take place would be crucial. The presence of 3D Anderson localization for the fundamental beam can create disordered cavity modes that would affect the SHG efficiency in unforeseen ways [35][31].

In this work, we measured the scaling of the second harmonic with the volume of the microspheres and the thickness of the slabs. We provided evidence of the linear scaling typical of RQPM with the number of domains, which was predicted for multiple scattering samples, but never explicitly shown [158][157]. It is interesting to note that the scaling with the number of domains is independent of the scattering strength in the assemblies. This common behavior suggests that the energy distribution of the pump and SHG in the sample, could be regulated by a more fundamental property such as the mean path length invariance [151]. This aspect could be investigated in a future study. An under-explored combination will be possible at the intersection of the field of nonlinear optics and wavefront shaping. For instance, a spatial light modulator (SLM) can be used to control the nonlinear speckle of RQPM second-harmonic generation as well as the linear speckle [30]. This approach could be used to explore a possible regime after the random quasi-phase-matching towards and "optimal" RQPM, to enhance further the efficiency of the nonlinear generation. Furthermore, the combination of wavefront shaping and NDPM can have deep implications

from fundamental studies such as the definition of nonlinear transmission matrix, to application in optical computing. The possibilities enabled by the combination of nonlinear and disordered materials can have unforeseeable impact on the coming years. In this chapter we presented and characterized a bottom-up fabricated platform in which the interplay of coherent nonlinear generation and multiple light scattering can be studied, to enable it to realize its potential.

## **5.5 Declaration of personal contribution**

The results presented in this chapter are published in [113]. The work presented was done by Romolo Savo, Jolanda Müller and me. My personal contribution was the implementation of the optical setup for both the linear and nonlinear measurements. I performed the linear measurement of total transmission with the integrating sphere, the SHG measurements on the LiNbO<sub>3</sub> slabs and the analysis of the data. The nonlinear measurements on the microspheres were done by Jolanda Müller.



## Chapter 6

# Modulated fluorescence of nanodiamonds in bottom-up dielectric microspheres

Optically active nitrogen vacancies in diamond (known as NV centers) have attracted considerable research interest in recent years. They have numerous applications in biophotonics [159], sensing [160], [161] and quantum optics [162]. To harness the potential of the NV centers, it is of great importance to manipulate their photonic properties, such as spectrum and emission rate. One of the most employed approach consists in coupling the NV centers to resonating structure [115].

In this chapter we present a novel approach based on active NV centers in nanoparticles of diamond (we will refer to them as nanodiamonds). The main idea is to couple the nanodiamonds with bottom-up fabricated microspheres of titanium dioxide  $\text{TiO}_2$ , with a fabrication process that is heavily scalable (see Chapter 3). The resulting hybrid microspheres (with a matrix of  $\text{TiO}_2$  and a 1% of nanodiamonds in volume) can manipulate the emission of the NV center thanks to two effects: the photonic nanojet which focuses the excitation in a small volume of the sphere [56], and the Mie resonances that enhance the fluorescent emission of the NV centers at specific wavelengths [50]. This approach could be ideal to create single photon sources, maximizing both the contribution of the pump and the emitted light. We begin the chapter describing briefly the NV centers, focusing on their optical properties. Then, we give an overview of the state of the art in the field of diamond nanophotonics, discussing different applications reported in literature to engineer the emission with plasmonic and dielectric resonators. Next, we present our optical results on the hybrid microspheres, showing that we can assemble bottom-up resonators that can present Mie resonances in the scattering cross section. These Mie resonances of the spheres can shape the emission from the nanodiamonds; we show this thanks to measurements of the photoluminescence spectrum. In the following section we demonstrate that, thanks to the thermo-optic effect, we can actively change the position of the resonances with the temperature. This tunability is crucial to match the modes of the resonator with the desired emission wavelength. To check whether the Mie-assisted fluorescence of the NV center could show an enhanced emission rate thanks to the Purcell effect, we measured the lifetime of the emitted light. We describe the technique employed which is time



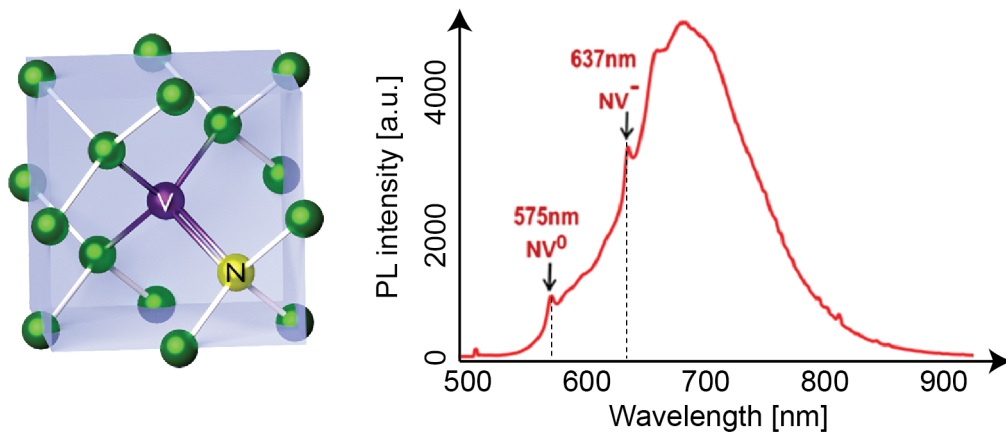


FIGURE 6.1: Crystal structure of diamond with a nitrogen vacancy. The substitutional nitrogen atom is represented in yellow with the neighboring vacancy in purple. All the other atoms in green are carbon. Photoluminescence spectrum of nitrogen vacancy in nanodiamonds of 100 nm, from Sigma Aldrich. The two ZPLs are at 575 nm and 637 nm are indicated by the dashed lines.

correlated single photon counting (TCSPC) in the following section and we present the results for the lifetime of the emission. Unfortunately, the low  $Q$  factor (about 200) and the large mode volume of the measured microspheres prevented us from measuring a clear reduction. To conclude, we show the measurement of the second-order correlation function  $g^{(2)}$  of the individual nanodiamonds with a Hanbury-Brown-Twiss (HBT) setup. This measurement is needed to assess the quality of the emitters and the setup prior to test the combination of the microspheres with the nanodiamonds. In the end, we summarize the results and the perspectives of this work. Parts of this chapter are taken from the Master thesis of Andrea Scheidegger and Daniel Streiff and from the semester thesis of Paolo Fischer.

## 6.1 Optically active NV centers in diamond

Diamond is a material with many interesting properties for photonics. It is biocompatible, chemically robust, has a transparency range from the deep ultra violet to the infrared, and has a refractive index of 2.4 in the visible range [163][164]. On top of these properties which are from bulk diamond, many other unique properties are enabled by optically active defects in diamond, sometimes referred as color centers [114]. These impurities consists of a missing atom in the lattice and/or a neighboring atom replaced with another material. There exists a host of optically active defects in diamond, determined by the element that replaces the carbon in the lattice. Their emission spectrum span the whole visible range and part of the infrared (therefore the name color center). Here, we focus on the nitrogen vacancy (NV center),

in which an atom of nitrogen replaces a carbon, as it is schematically illustrated in Fig. 6.1. The NV centers are the first and most studied defects in diamonds for their outstanding spin properties [165]. They have vast applications in the detection and imaging of magnetic field at the nanoscale, which is enabled by the spin of the defect in the diamond placed in a tip of a scanning probe setup. NV centers display a long coherence time and the spin can be coupled to its fluorescence allowing for an optical readout of the spin state. This topic is not the focus of the work discussed in this chapter, for a detail discussion of the properties of NV centers for magnetometry we refer the reader to the following review [166]. Moreover, the emission from NV centers does not blink nor photobleach, which makes them ideal as biomarker [167]. The other most important application of optically active NV centers is to use them as single photon sources. The NV center exists in two states: the neutral  $NV^0$  and the negatively charged state  $NV^-$ . These two defects can be excited with an optical beam in the range 490 nm to 560 nm of wavelength. Then, they relax into the ground state by emitting a photon at a specific wavelength which is 575 nm for the  $NV^0$  and 637 nm for the  $NV^-$  [168]. These two emission lines are called zero-phonon lines (ZPL) since they are the result of the radiative decay in the ground level, without interaction with the lattice. These two lines are highlighted by the arrows in Fig. 6.1. The rest of the broad spectrum from 500 nm to 900 nm, is constituted by phonon-assisted transitions. The photons emitted at the ZPL are preferred for quantum applications thanks to their defined energy. The ratio of the number of photon emitted in the ZPL compared to the total emission is called Debye-Waller factor  $\eta_{DW}$ . Compared to other defects such as silicon vacancies (SiV)  $\eta_{DW}$  for NV centers is rather small around 0.04 [169].

### 6.1.1 Single photon emission

Single photon emitters are a key building block of quantum optics [170]. The ideal single photon source should emit only one photon at a known time, indistinguishable from the others with a fast emission rate. The emission rate can be tested with TCSPC, the degree of indistinguishability with a Hong-Ou-Mandel experiment. To provide evidence that the emitters are single photons, we measure the antibunching. That means that the probability of detecting two photons at the same time tends to zero. This measurement is routinely done with a Harnbury-Brown-Twiss setup (HBT) [171]. The measured quantity is the second-order autocorrelation function  $g^{(2)}$

$$g^{(2)}(\tau) = \frac{\langle I(t)I(t+\tau) \rangle}{\langle I^2(t) \rangle} \quad (6.1)$$

A typical example of antibunching is reported in Fig. 6.2.

The emission of single photons from a NV center can be enhanced with two mechanisms. The first one consist in enhancing the excitation field intensity on the emitter. The second one is enhancing the quantum yield, i.e. the ratio of the radiative decay rate over the total decay rate. It can summarized with the following Eq. 6.2

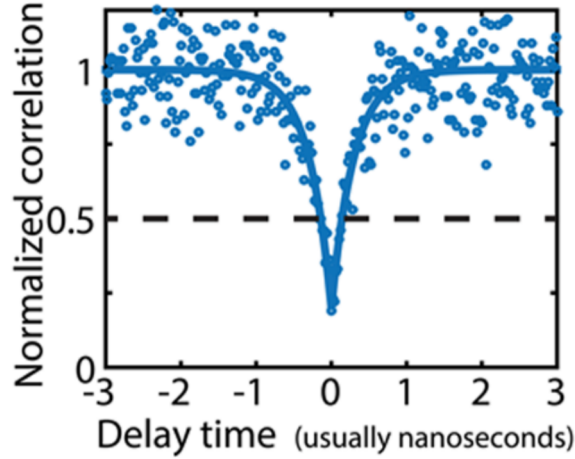


FIGURE 6.2: Typical measurement of antibunching in the second-order autocorrelation function  $g^{(2)}$  for single photons. Adapted from [172].

$$\rho = \frac{\gamma_{rad}}{\gamma_{rad} + \gamma_{non-rad}} \quad (6.2)$$

where  $\gamma_{rad}$  is the radiative decay rate and  $\gamma_{non-rad}$  is the non-radiative one. In this context the lifetime is defined by  $\tau = \frac{1}{\gamma}$ . The radiative decay rate can be modified by increasing the local density of state of the emitter, and this can be achieved by coupling the emitter to a cavity and exploiting the Purcell enhancement  $F$  [173].

$$F = \frac{3}{4\pi^2} \lambda^3 \frac{Q}{V} \quad (6.3)$$

$Q$  represents the quality factor of the resonator and  $V$  its volume. In our work the idea is to use the nanodiamond in a microsphere that should increase the pump intensity and to shape the emission thanks to its resonant Mie modes.

## 6.2 State of the art

As we mentioned in the previous section, an improved emission from the NV centers has been obtained by coupling the defects to resonant structures. Three reviews detail the progress of this active field [114], [115, 164]. The two main types of resonators are the plasmonic and the dielectric ones. Plasmonic resonators are very useful since they support broadband modes and they have a very small mode volume which allows to reach high Purcell enhancement (see Eq. 6.3). In fact, they have been used to increase the rate of the emission from a single NV centers by at least two orders of magnitude. The common drawback of this approach is constituted by the Ohmic losses which are due to the strong absorption of the metals. One notable example is represented in Fig. 6.3a, in where Bogdanov *et. al* coupled a single nanodiamond with a silver nanocube on a silver substrate [174]. The enhancement

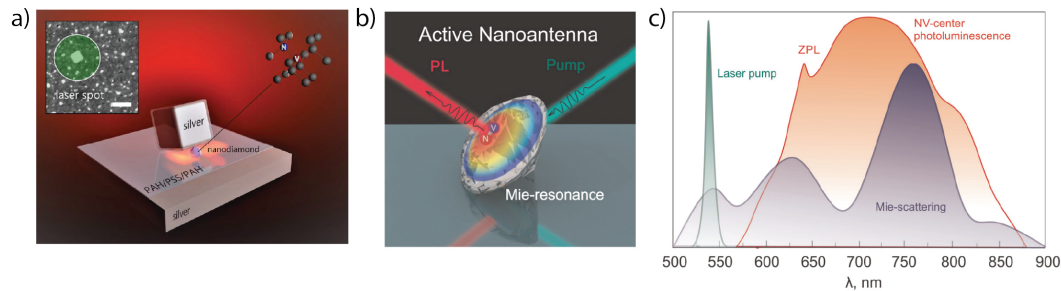


FIGURE 6.3: NV centers coupled with resonators. a) Schematic of a nanodiamond in a plasmonic resonator done by a silver nanocube and substrate. Image taken from [174]. b) Sketch of the working principle of Mie-enhanced photoluminescence from diamonds. c) Schematic of fluorescence modulated by the Mie modes of the dielectric resonator. Adapted from [173].

that they achieve is indeed remarkable, however the process is hardly scalable, since it requires to randomly disperse the nanocubes on a sample with spin coated nanodiamonds. Another viable approach which does not suffer from the absorption losses is constituted by coupling the NV centers with a dielectric resonator. For instance, thanks to ion beam milling, it is possible to shape the diamond with NV centers into a resonator down to sizes in the range 100 nm to 400 nm, where it should exhibit Mie modes [173]. The sketch of the sample and the concept of this work is displayed in Fig. 6.3b,c. This technique can display up to two-fold enhancement of the emission rate, but no single photon emission ( with  $g^{(2)}$  measurements ) given that it is hard to locate a single defect and mill a structure around it, resulting in Mie resonators with several NV centers. A recent work by Obydenov *et al.* demonstrated the concept of Mie resonance assisted spontaneous light emission in nanodiamonds synthesized by high pressure high temperature technique (HPHT) [175]. There, they gave evidence of an enhanced emission rate and of an increase in the Raman intensity thanks to the Mie modes. However, they work with silicon vacancies (SiV) and their method can not be applied for single photon sources due to the high number of defects in a single assembly. An alternative solution is to take single nanoparticles of diamond with defects (nanodiamond) and couple them one-by-one with a dielectric sphere [176]. Many of the insightful methods summarized here have the common drawback of the scalability, since they can produce single photon sources coupled with resonator at the cost of micromanipulating each individual structure. Our idea is to achieve comparable results with bottom-up fabricated spheres whose fabrication can be heavily scaled, as discussed in Chapter 3. The advantage from the fabrication side is that we can also carefully control the concentration of the nanodiamonds (therefore the concentrations of the NV centers) in each microassembly.

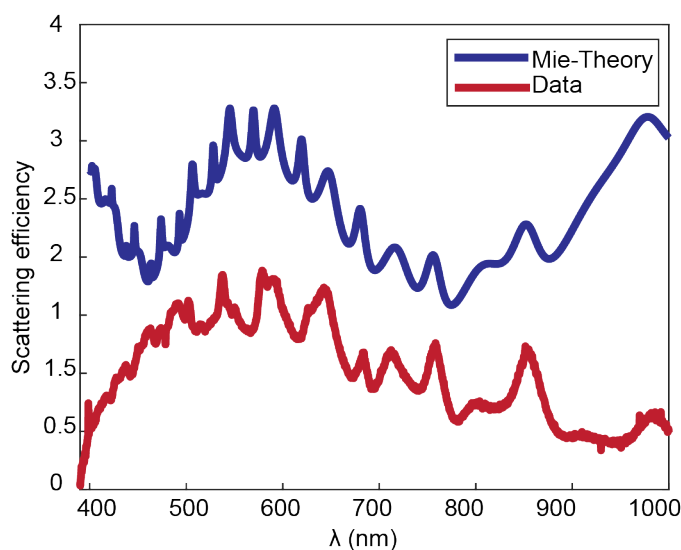


FIGURE 6.4: Experimental and theoretical scattering cross section of a  $\text{TiO}_2$  microsphere. The experimental data in red are collected from a sphere of diameter  $(1.4 \pm 0.4) \mu\text{m}$  measured with a darkfield microscope. In blue scattering efficiency for a  $\text{TiO}_2$  microsphere of  $1.46 \mu\text{m}$  composed entirely of  $\text{TiO}_2$  and filling fraction 0.58. The imaginary part of the refractive index  $k$  is 0.001.

### 6.3 Fluorescence modulation

To fabricate the microsphere we used titanium dioxide ( $\text{TiO}_2$ ) nanoparticles, as shown in Chapter 3.  $\text{TiO}_2$  was chosen for its transparency combined with high refractive index of 2.7 in the visible spectrum. Both these properties are useful to fabricate a resonator in the visible range with low losses and high mode confinement. On top of that, the small size of 15 nm of the  $\text{TiO}_2$  nanoparticles allowed us to fabricate structures with smooth surfaces. To assess the quality of the fabrication, we measured the scattering cross section with dark-field microscopy, similarly to what we did for the  $\text{BaTiO}_3$  microspheres in Chapter 4. We compared the scattering cross section with the one obtained through analytical calculation with the effective medium Mie model (EMM). The data are reported in Fig. 6.4. The discrepancy in the in the y-axis can be attributed to our setup, that was not collecting all the light scattered in transmission. However, the qualitative agreement between the model and the experiment can be appreciated for positions and shape of the peaks. This correspondence indicates that the microspheres of titania interact with the illumination beam as an effective medium. Therefore our bottom-up fabrication can deliver spheres that are effectively a resonator for the light and that can be modeled with our effective medium Mie model.

The fluorescence of the hybrid microspheres was measured with the setup depicted in Fig. 6.5a. A pulsed laser at 520 nm wavelength of emission (Thorlabs, NPL52C), is focused and the sample and the collected light is directed to a camera or to an optical fiber (to be sent into a spectrometer). An SEM

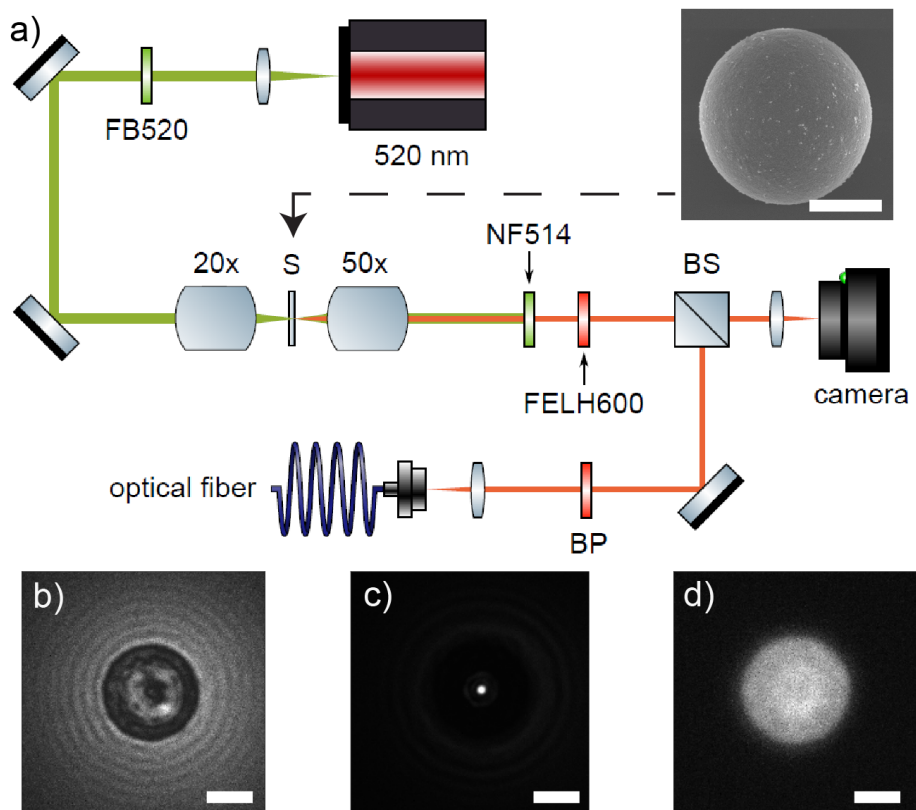


FIGURE 6.5: a) Schematic of the setup used to measure the images of the microspheres and to collect the spectra. In the inset, SEM of a microsphere of around  $6 \mu\text{m}$  diameter. The scalebar is fixed for all the figures to  $3 \mu\text{m}$ . b) Image of a hybrid microsphere with the image plane in the center of the sphere. c) Image of the sphere with focal plane on the rear part of the microsphere, to highlight the focusing (nanojet). d) Fluorescence image, filtering out the pump.

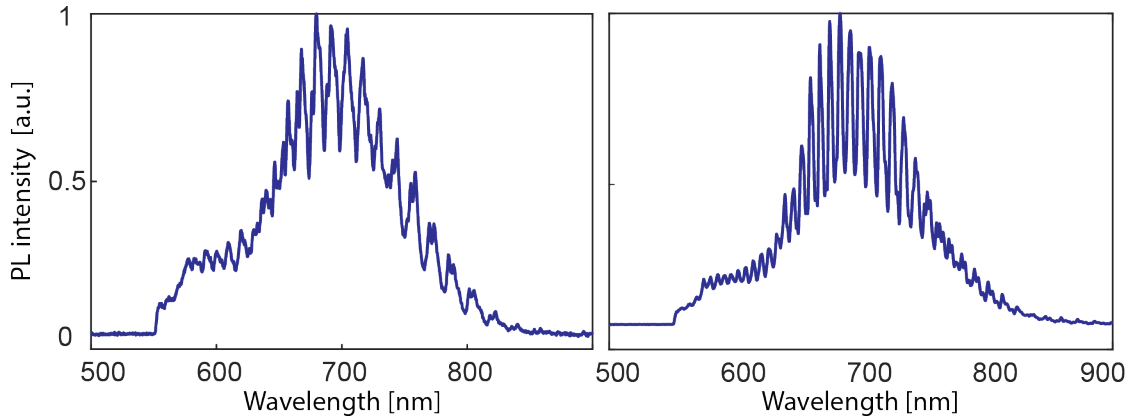


FIGURE 6.6: Fluorescence spectra collected for two microspheres of  $5\ \mu\text{m}$  of diameter and  $10\ \mu\text{m}$  diameter. The pump wavelength used is  $520\ \text{nm}$  and a longpass filter 550 is used to block the pump light.

picture of a hybrid microsphere is also shown in Fig. 6.5. The images of the microspheres show the strong focusing typical of the photonic nanojet for the pump as well as emission from the whole volume. With the same setup it is possible to measure the fluorescence spectrum. It is displayed in Fig. 6.6, for two microspheres with 1% nanodiamonds compared to  $\text{TiO}_2$  of diameter  $5\ \mu\text{m}$  and  $10\ \mu\text{m}$ , respectively. It is possible to see that the width of the modes decreases with the size of the microsphere as it is expected from Mie theory.

The results displayed in Fig. 6.6 give evidence that we can modify the spectrum of the emitted fluorescence from the nanodiamonds thanks to the spherical geometry of the assembly. The Q factor of the peaks is around 200. As we pointed out in beginning of the chapter, for single photons applications we want to work close to a ZPL line. Therefore, we would have spheres of a certain size with a resonance at that wavelength and spheres of other sizes without a resonant peak. This means that, to exploit the modes, we should control the size of the sphere and target a specific size to match the mode of the assembly with the ZPL at  $637\ \text{nm}$ . The fabrication used to assemble the spheres for this measurement was producing microspheres polydispersed in size, thus it was not suitable to target a specific resonant size. For this reason, we decided to exploit the thermo-optic effect to change the refractive index of the sphere to shift the modes.

## 6.4 Thermal shift of the resonances

The same setup illustrated in Fig. 6.5a was used to measure the spectrum for different temperatures. The measured microsphere has a diameter of  $10\ \mu\text{m}$  and the temperature was changed in the range  $21^\circ\text{C}$  and  $220^\circ\text{C}$ , as can be seen in Fig. 6.7a. The two arrows indicate the peaks taken as examples that shift to lower wavelengths. The central position of three peaks is represented in Fig. 6.7b. We can see that even a modest change in the temperature of tens of degrees is sufficient to shift a resonance (measured by the central

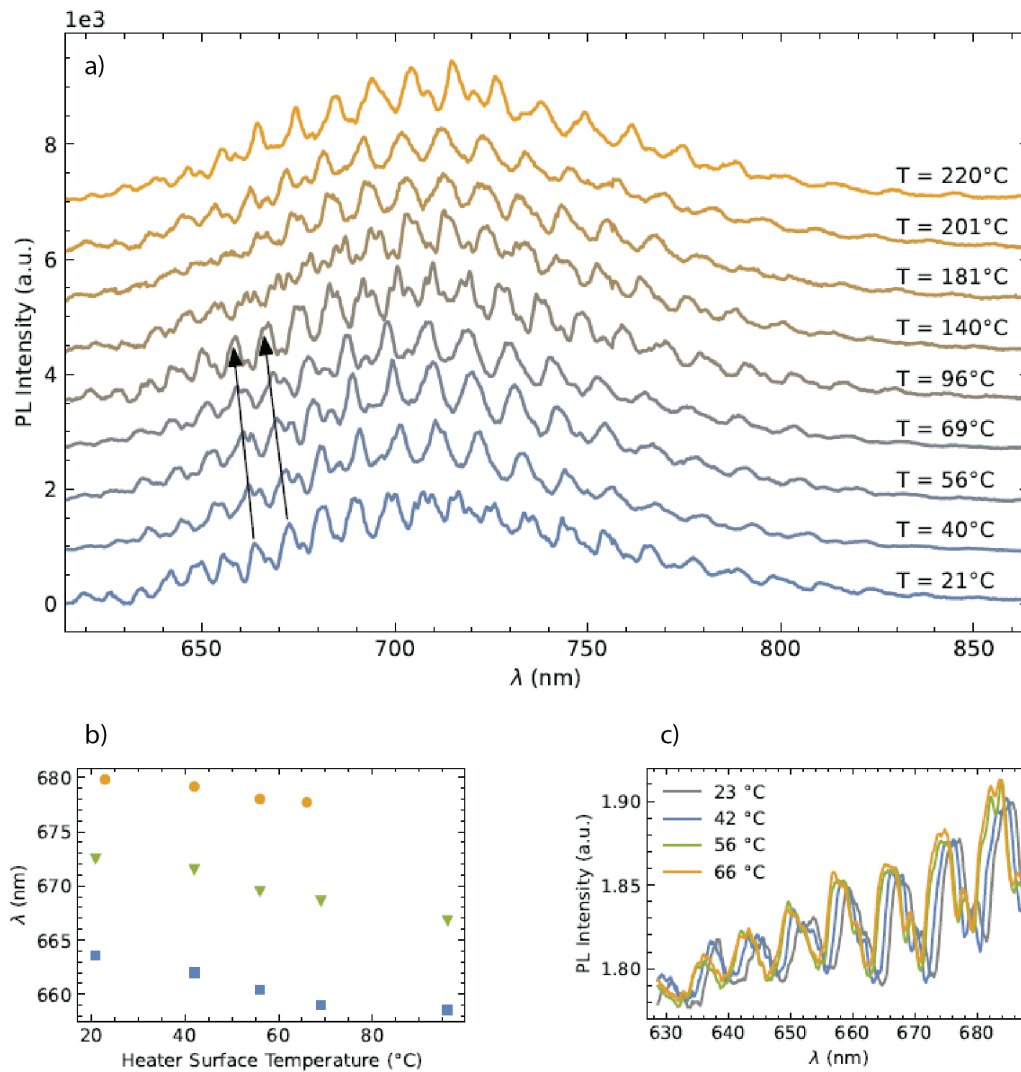


FIGURE 6.7: Thermal shift of the Mie resonances in the fluorescence. a) Fluorescence spectra at different temperatures  $T$ . As the temperature of the substrate increases, the effective refractive index of the  $\text{TiO}_2$  decreases, modifying the emission spectrum. b) Central position of specific peaks for different temperatures. c) Spectral shift for a microsphere heated with a Peltier element in a narrower temperature range.



wavelength position) by few nanometers. We performed Mie theory simulations to match the modes. For simplicity, we neglected the contribution of the nanodiamonds in the calculation of the effective refractive index of the microspheres (they constitute by design 1% only of the volume). Moreover we assumed that the spherical geometry is preserved for different temperatures such that we can use the Mie theory for spherical microparticles. In a next step, we changed the effective refractive index of  $\Delta n = 0.033$  and this produces a shift around 4 nm in the peak wavelength. This is compatible to our measurement with  $\Delta T = 49^\circ\text{C}$ . By computing the thermo-optic coefficient at room temperature in the wavelength range from 650 nm to 700 nm we get a negative number of the order of  $10^{-4}\text{K}^{-1}$ . This is compatible to values reported in the literature for the thermo-optic coefficient of thin film of  $\text{TiO}_2$  [177]. For example Zhang *et al.* [178], reported a value of  $-4 \cdot 10^{-4}\text{K}^{-1}$ . Even though the order of magnitude of the coefficient agrees with some work in literature, we point out that different values can be found in literature for different size of the nanoparticles, different thicknesses and different annealing temperatures.

#### 6.4.1 Lifetime measurements

We measured the temperature dependence of the fluorescence lifetime of the hybrid microspheres with the setup depicted in Fig. 6.8a. The set-up is similar to the one depicted in Fig. 6.5a but the fiber is sent to a single photon detector and the technique used is the time correlated single photon measurement. The working principle is the following: a train of laser pulses of 10 ns is sent on the sample and excites periodically the system. We record the delay between the trigger of the pulse, which is a consistent measurement of the time of the emission of the pump pulse, and the arrival of one emitted photon on our single photon detector. If we repeat this measurement several times, we are able to construct an histogram of photons collected versus the time delay with the trigger. With large enough statistic we can map the exponential decay of the emission. There are a couple of small caveat in this method. First, it works only provided that only 2% or less of the pulses are causing the emission of a photon from the sample. This is done to prevent the pile-up distortion on the detector which happens if too many photons are emitted by the NV centers. Secondly, the measured curve is not the true decay of the emitter, but rather it is a convolution with the temporal profile of the pump [179]. This can become an issue if the temporal width of the pump laser is not negligible compared to the characteristic decay time of the exponential. An example of measured exponential decay is show in Fig. 6.8b. It is possible to fit the data with an multi-exponential fit, to take into account the instrument response function. However, we applied a more robust method to deconvolve the signal from the IRF. The method chose is the iterative reconvolution [180]. It performs a least square fitting where the model function is given by the convolution of the IRF with an exponential decay. The final output of the code is the function that minimizes the residuals.

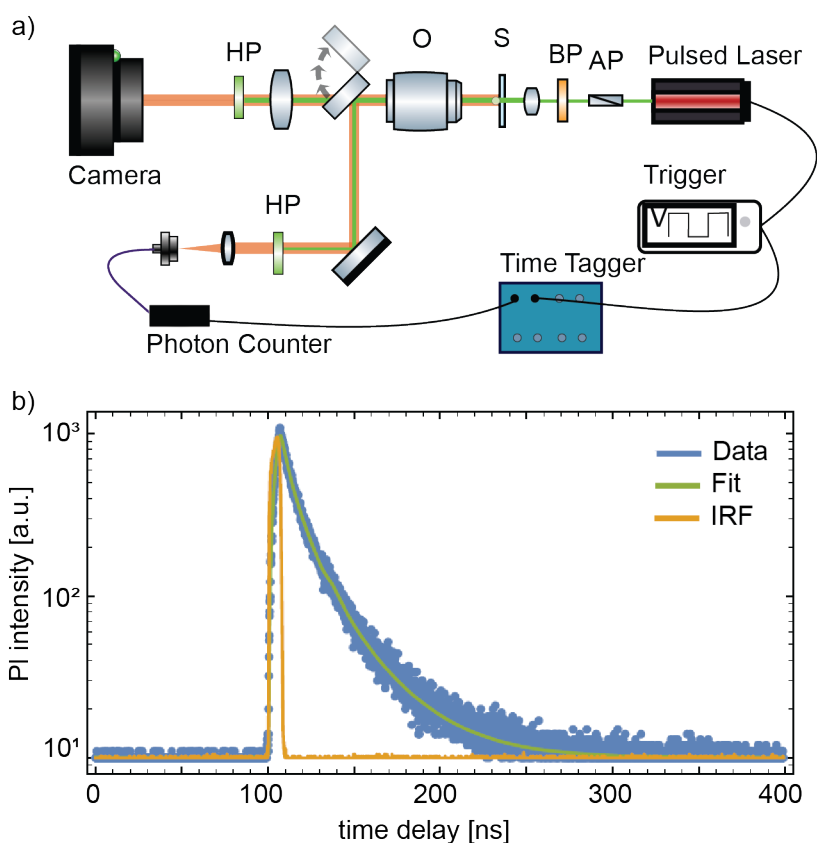


FIGURE 6.8: a) Setup for time correlated single photon counting. The laser source (NPL52C, 520nm, 6-120 ns pulse width, max 50 kHz, Thorlabs) is triggered with square voltage generator. The laser wavelength is filtered with long-pass filters and the signal is detected by single photon counting unit ((C14463-050GD, Hamamatsu). The time difference is measured via a time tagger (time tagger ultra, Swabian Instruments). b) Typical fluorescence decay measurement. The instrument response function in yellow was measured using TCSPC with the laser light itself heavily attenuated with neutral density filters.

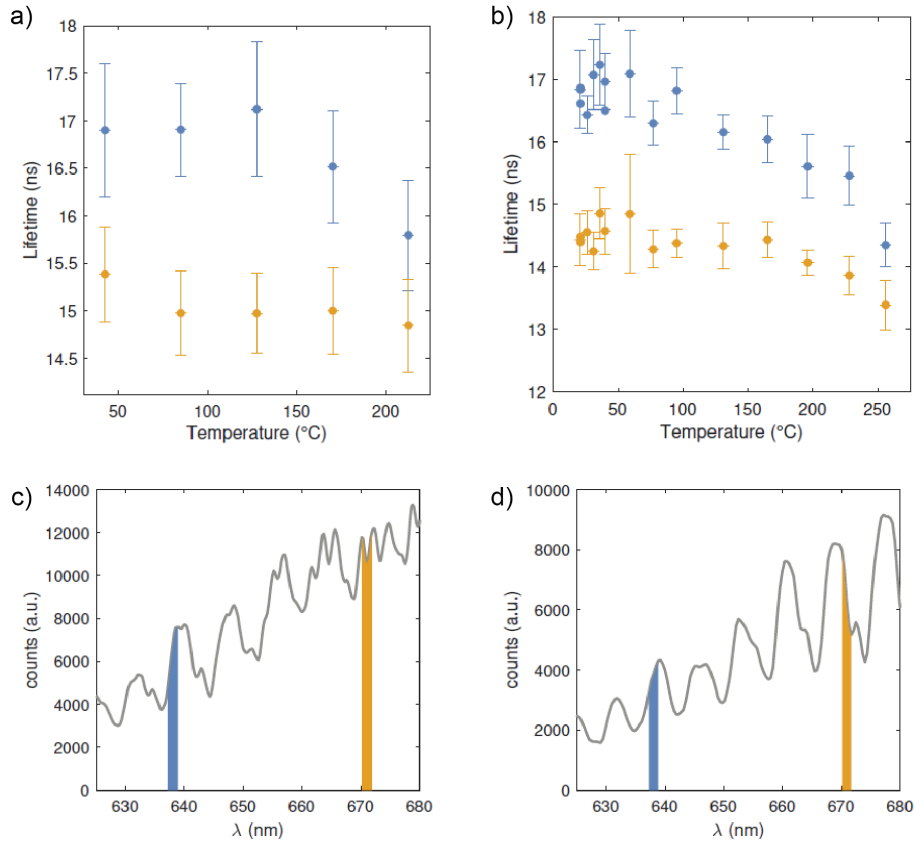


FIGURE 6.9: a,b) Fluorescence lifetime in the range 636 nm - 638 nm (in blue) and in the range 670 nm - 672 nm (in yellow) as a function of the applied temperature for two different spheres of diameter 10  $\mu\text{m}$ . The points in the upper plots are extracted from the fit of the lifetime. c,d) Fluorescence spectra of the two microspheres with a shaded area that highlights the collected wavelength range.

## 6.4.2 Temperature dependent lifetime

To check the effect of the temperature change on the lifetime we filtered the fluorescence of the hybrid microspheres with two narrow bandpass filters of central wavelength 637 nm and 671 nm with a FWHM of 2 nm. The filter at 637 nm was selected because it can select the photons emitted at the ZPL of the NV center, the most suitable candidate to generate single photons. The filter at 671 nm was chosen because it is located in the spot of the maximal emission from the microspheres. The idea is that, by means of the applied temperature, we can shift the peaks of the fluorescence. This for certain temperature should increase the emission rate thanks to the Purcell enhancement. Therefore, by recording the lifetime as a function of the temperature, we should see the modulation of the lifetime, i.e. fast emission on a peak of the resonance and slower emission elsewhere. We show these measurements for two spheres that displayed resonances in the wavelength range of the filters. The spectra

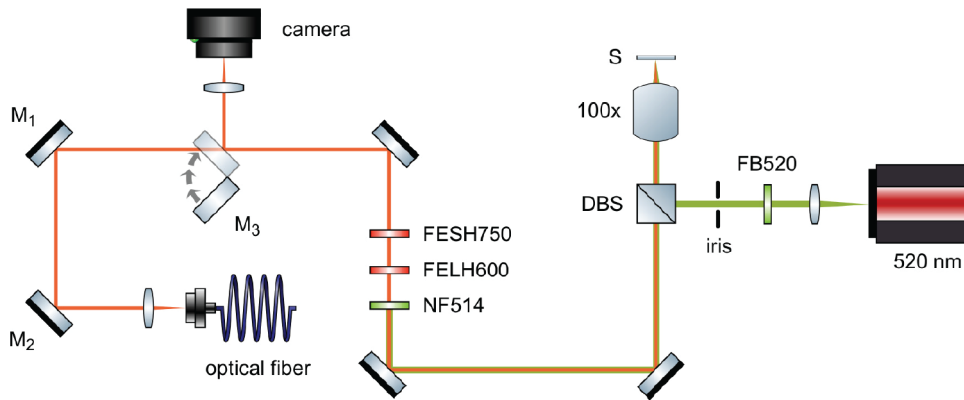


FIGURE 6.10: Hanbury-Brown-Twiss interferometer used to measure the second-order correlation function  $g^{(2)}$  for the emission of the nanodiamonds.

are plotted in Fig. 6.9c,d. From these spectra they demonstrate that with narrow band pass filter we are able to collect the signal from a single peak of the spectrum, if placed in correspondence of the center of the peak. In Fig. 6.9 we plotted the lifetime fitted with the iterative reconvolution method. The modulation lies within the error limits of our measurements, therefore we can not conclude that the lifetime is modulated by the different resonances of the assembly. We can see a clear descending trend that has to be attributed by different transition times in the electronic levels of the NV centers due to the temperature. However we do not detect a change in correspondence of the peaks in the spectra. This can be explained with the volume dependency of the Purcell factor of Eq. 6.3. In particular our modest Q factor is counterbalanced at the denominator by a volume that is too big for a sphere of several microns. The mode volume of our measured microspheres is not small enough to allow the Purcell effect to reduce the lifetime, we should repeat the measurement with spheres of sub-micron diameter or replace the NV center with SiV center that have a narrower emission line at room temperature.

## 6.5 Single photon emission

To measure the single photons from the nanodiamonds we spin coated some diamonds containing NV centers on a glass substrate. The spinning parameters and the choice of the specific nanodiamond is described in Chapter 3, the important parameter here is that the nanodiamonds have roughly size of 20 nm, and contain on average a single NV center. The new setup which works in reflection, was chosen in analogy to many setups reported in the literature. The sample with the spin coated nanodiamonds was placed face-down in the setup depicted in Fig. 6.10. This was done to prevent the losses due to the substrate, given that we were not working with an oil-immersion objective and a index matching liquid. One of the main advantages comes from the dichroic beam splitter that allows to remove efficiently the laser light after the excitation of the sample. The signal is then sent into a fiber with a built-in

50:50 beam splitter that directs the light to two single photon counting modules (SPCM). Contrary to what was done to measure the fluorescence with the TCSPC method, here we are measuring with the time tagger the difference of the arrival time of photons in the two ends of the fiber. The signal of single NV centers is too small to be able to image large area of the sample with a camera (that was use for alignment only). Instead, the scanning of the sample was done by measuring the counts in the SPCM moving laterally the samples with motorized stages. The spin coated sample with NV centers were coarsely scanned on the x and y axis and a multi-mode fiber (to collect more light). The result of one of these scans is displayed in Fig. 6.11a. The x-y position is plotted with the number of counts per second recorded in one of the two SPCM. They present a lot of brights spots that correspond to nanodiamonds or, more likely, clusters of nanodiamonds. However, the signal-to-noise ratio is very low due to collection from areas that presented several NV centers. For this reason, we replaced the multimode fiber with a single mode fiber, realizing a confocal microscope, in which the fiber core acted as a pinhole of the setup. With this upgrade it was possible to increase heavily the signal-to-noise ratio. The measurement with the upgraded setup is plotted in Fig. 6.11b where the collected area is the one in the white rectangle of Fig. 6.11a. The bright spots in the figure are candidate single photon sources. All the measurements were performed with 1.3 mW of average pump power. The area in Fig. 6.11b highlighted by a white circle contains the nanodiamond whose  $g^{(2)}$  function is reported in Fig. 6.11c. The antibunching dip is evident at zero delay between the arrival of the photons and provides evidence of nonclassical radiation.

To explain this dip we should start by using the following equation

$$g^{(2)}(\tau) = 1 - e^{-\tau/\tau_0} \quad (6.4)$$

which describes the dip at  $\tau = 0$ . This represents the fact that the single NV center can not emit two consecutive photons with a time delay smaller than  $\tau_0$ . This formula must be upgraded to account for background radiation. In fact our SPCMs can have a detection event also triggered by background radiation or electrical noise. We call  $p_s$  the probability that a certain detection is triggered by a photon from the diamonds, while  $p_b$  for the detection of noise. Therefore, the  $g^{(2)}$  of our HBT setup has to be expressed as

$$g_{exp}^{(2)}(\tau) = p_s^2 g_s^{(2)}(0) + 2p_s p_b + p_b^2 \quad (6.5)$$

where the first term represents a double detection of photons emitted by the NV centers, and the other terms are one count from the background and one from the sample, and finally two counts from the noise. Thanks to Eq. 6.4 and Eq. 6.4, we can write:

$$g_{exp}^{(2)}(\tau) = p_s^2 \left( 1 + \frac{1}{n} \left[ -c e^{-\tau/\tau_1} + (c-1) e^{-\tau/\tau_2} \right] \right) + 1 - p_s^2 \quad (6.6)$$

where the factor n was introduce to account for multiple NV centers. The fit of the data of Fig. 6.11c with the function from Eq. 6.6 returns

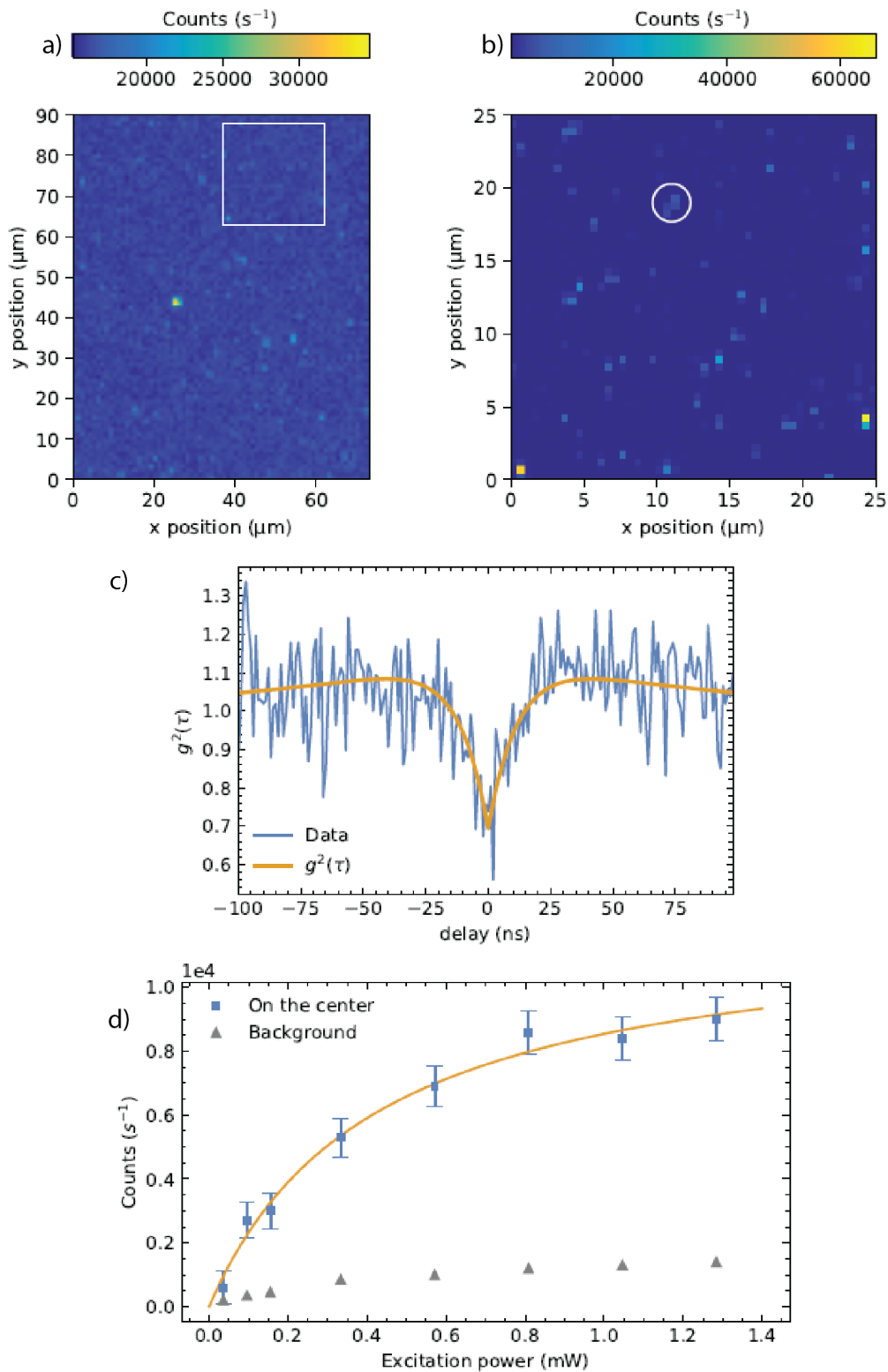


FIGURE 6.11: 2D fluorescent image of spin coated nanodiamonds on a glass substrate scanned over the lateral size. a) Scan performed with a multimode fiber. b) Scan done with a single mode fiber to increase the signal-to-noise ratio. The area highlighted with the white circle is the one investigated in the following plots. c) Experimental  $g^{(2)}(\tau)$  with the fit. d) Counts on the SPCM as a function of the excitation power, which displays the typical saturation behavior.

$g^{(2)}(0) = 0.69$  and  $n = 2.23 \pm 0.18$ . This means that, most likely, we are detecting the emission from a cluster of two nanodiamonds, or a single nanodiamond with two active NV centers. In Fig. 6.11d we investigated the saturation trend, measuring the emitted signal in comparison with the background while increasing the pump power.

## 6.6 Summary and perspectives

In this chapter we presented a novel approach that had the ambitious goal of producing scalable single photon sources. We have benefited from the emulsion-templated assembly developed for the BaTiO<sub>3</sub> and LiNbO<sub>3</sub> microspheres described in Chapter 4, 5. We used as a host matrix TiO<sub>2</sub> nanoparticles that, with their high refractive index and small size, allowed to fabricate sphere with high surface quality. We added in the fabrication a small proportion of nanodiamonds containing NV centers. The resulting hybrid microspheres displayed a fluorescence spectrum which was modulated by the Mie resonances stemming from the sphericity of the assemblies. Therefore the resonant properties of the assemblies are able to increase the intensity of the emission at certain wavelength. Since the targeted wavelength that we wanted to enhance was in correspondence of the ZPL at 637 nm, we studied how we could control the position of the Mie peaks to boost the emission at that wavelength. This was demonstrated thanks to the thermo-optics effect of TiO<sub>2</sub>. Therefore, our bottom-up microspheres are effectively an active resonator that can control the wavelength dependent emission with the temperature. Nevertheless, the key measurement of the modulation of the lifetime with the temperature did not succeed. In fact, with the data displayed in Fig. 6.9, it is not possible to identify a clear modulation of the lifetime with the temperature. The reason for this absence can be found in the big mode volume that suppresses the Purcell enhancement. In the final part we showed the set-up and the measurement on individual nanodiamonds with one NV center. This is a key step towards the measurement of  $g^{(2)}$  in NV centers coupled to the microspheres. We showed that our diamonds can be used to emit single photons and that our setup can be used to measure their second-order correlation function.

Some challenges are still to be faced, in particular one can be very harmful for the success of the project. That is a small fluorescence from the matrix of TiO<sub>2</sub> of the sphere. The origin of this fluorescence is still to be clarified, but for single photon measurement even a small background radiation can suppress the emission from the NV centers.

A possible route to use this bottom-up fabrication to enhance the emission rate of the single photons from the nanodiamond would be to fabricate small spheres (submicron radius) to increase the local density of states with the Purcell. This is similar to what was done in recent works [173][175]. The difference would be that in our case the fabrication is cheaper and scalable, and in principle allows to control fully the concentration of defects in the assemblies. Another interesting upgrade would be to replace the NV centers

with SiV vacancies that exhibit a sharper emission line at room temperature. A general upgrade would be to repeat the measurements at cryogenic temperature to suppress the emission in the phonon sidebands. There is another interesting aspect that we mentioned but did not elaborate further: the pump beam impinging on the microsphere, generates the photonic nanojet. This phenomenon concentrates the pump with high intensity in a small volume on the rear part of the microsphere. With an improved microfluidic fabrication, similarly to what it is done with Janus nanoparticles [181], it would be possible to position one nanodiamond exactly at the top of the microsphere, such that it could benefit the most from the resonant enhancement of the pump. In conclusion, further steps are needed to realize bottom-up scalable single photon sources and the potential of the assemblies that we conceived, fabricated and analyzed in this chapter has still to be fully unlocked.

## 6.7 Declaration of personal contribution

The work presented was done by different students under my supervision. Andrea Scheidegger implemented the fabrication (master thesis), Daniel Streiff the thermal measurements and the second-order correlation measurements (master thesis), Paolo Fischer the fluorescence spectra (bachelor thesis). I was mainly responsible for the conception of the project and supervised the optical setups and the measurements.





## Chapter 7

# Conclusion and Outlook

In this thesis we showed that bottom-up disordered assemblies of noncentrosymmetric nanocrystals can be used for broadband second-harmonic generation in the random quasi-phase-matching scheme. The material used,  $\text{BaTiO}_3$  and  $\text{LiNbO}_3$ , are chosen for their broad transparency windows in the visible and infrared part of the spectrum and high nonlinear coefficients. The assemblies constitute as well an ideal platform to study the interplay of nonlinearity and disorder. The core of the efforts of this thesis was to find a solution to compensate for the main challenge of second-harmonic generation through RQPM: the lower efficiency compared to SHG from phase-matched or quasi-phase-matched crystals. In Chapter 3 we described how it is possible to assemble microspheres of nanoparticles. The special feature of the templated emulsion assembly is that it produces well-formed microspheres while ensuring that the position and orientation of the nanocrystals are randomized. Another advantage of the fabrication used is that it can be applied to every material available in nanocrystals in solution, or even to mixtures. This flexibility allows to control the effective refractive index of the assemblies and to tune their optical property (for example embedding NV centers, quantum dots, rare-earth doped particles). The other benefit of the bottom-up fabrication is the large scale production of assemblies at a low cost. We presented as well how our manufacture can be upgraded thanks to microfluidics, to target specific sizes achieving a great control of the properties of the fabricated structures.

In Chapter 4 we presented the microspheres assembled with  $\text{BaTiO}_3$  nanoparticles. The goal of this project was to show that it is possible to enhance the SHG from a disordered material with the help of the Mie resonances. Interestingly, this requires exploiting the disorder of the distribution of domains in the spheres on one side, and on the other hand, the order of the geometry imposed on the assembly. We showed first that the spheres presented Mie resonances in the scattering cross section, to give evidence that they behaved as effective medium in the linear interaction. We supported this with numerical simulation with COMSOL and analytical simulation with a model combining effective medium approximation and Mie theory (EMM). We demonstrated the SHG with spectral and power measurements. More interesting is the scaling of the SHG with the volume of the microspheres, which showed a linear trend. The novelty of this result lies in the fact that until now this had been shown only for transparent polycrystals (tens of microns in domains size) in a slab geometry. By sweeping the pump wavelength we confirmed

that the emission is broadband and we matched the modes presented in the emission with our EMM model. Additionally, we compared the efficiency of the RQPM SHG coupled with Mie modes, with the nonlinear emission without the Mie modes. This evidences at least an order of magnitude of increase. When a pump beam impacts the assemblies, the spherical geometry generates two phenomena which are included in the Mie theory: the photonic nanojet and the wavelength-dependent Mie modes. This fact has a twofold impact on the energy of a pump: firstly, the nano-jet constitutes a self-focusing that concentrates much of the power in a smaller volume of the sample; secondly, at certain wavelengths, the pump power is more confined to the spheres. Both of these effects result in an enhanced non-linear emission from the microsphere.

In Chapter 5 the goal was to increase the efficiency of the SHG from a disordered material by increasing the size of the nonlinear domains (up to 100 nm - 400 nm). We used LiNbO<sub>3</sub> nanocubes that were previously characterized for their high scattering cross section and second-harmonic generation efficiency. In fact, the assemblies with the LiNbO<sub>3</sub> nanocubes displayed a very strong light scattering. Despite the fact that the microspheres of this chapter can look similar to the ones in the previous chapter, the physics within the assemblies is radically different. By increasing the size we also suppressed all the Mie modes from the whole assembly. To study the scattering properties, we also fabricated the slabs with the same nanocubes and similar filling fraction. Our measurements revealed a NDPM with a transport mean free path as short as  $l^*$  of  $476 \pm 6$  at 750nm of wavelength. The strength of the scattering was also qualitatively confirmed by the opaqueness of the samples that were completely white even when the thickness was only 1  $\mu$ m. We used the slabs and the spheres to show that the SHG with the random quasi-phase-matching is robust to scattering. Moreover, the law of the linear scaling with the thickness (or the volume) is preserved even in the presence of scattering. This linear scaling appears to be related to some more fundamental property of light generation in disordered material since it does not depend on the scattering strength or on the sample geometry. This can be seen by comparing the two scalings in Fig. 4.8 and Fig. 5.9.

Chapter 6 is a bit of a stand-alone in the broader scope of this thesis, since it does not involve second-harmonic generation from a disordered material. The link with the rest of the work is constituted by the same bottom-up fabrication and the idea to exploit the Mie resonances to enhance a certain optical performance. In this case, we used TiO<sub>2</sub> as a host matrix to create hybrid microspheres containing nanodiamonds. The intent was to use the nanojet to increase the intensity of the pump in a small area with a NV center and to exploit the Purcell effect to enhance the single photon emission rate. In the chapter we showed good fabrication results (also with the outlook given by the microfluidics approach), with microspheres with controlled concentration of the nanodiamonds. We gave evidence of heavily modulated fluorescence of the NV centers thanks to the Mie resonances and also that these modes could be tuned with temperature thanks to the thermo-optic effect. Therefore we achieved bottom-up resonators that emitted fluorescent light

that could be actively controlled with the temperature. Nonetheless, we measured spheres with a volume that was too big (sizes above  $5 \mu\text{m}$  in diameter) and this suppressed the Purcell effect. In fact, our lifetime measurements did not show a clear reduction in the lifetime (enhanced emission rate). In the end of the chapter, we demonstrated and characterized a setup to measure second-order correlation function  $g^{(2)}$  from single nanodiamonds. This was done to check the single photons from our NV centers prior to measuring the  $g^{(2)}$  from hybrid microspheres.

To conclude, in this thesis we contributed to show a part of the potential of the nonlinear properties of disordered materials. We illustrated the advantages of our platform based on noncentrosymmetric crystals and bottom-up fabrication. Other possibilities are illustrated in a recent perspective article [182]. Moreover, we presented and analyzed strategies to improve the efficiency of the SHG with the random quasi-phase-matching scheme. We believe that this topic presents promising prospects, some of which are briefly discussed in the next section.

## 7.1 Outlook

In this last section, I would like to examine the results presented in this thesis and highlight what the future challenges are and what can be improved. Afterwards, I will try to envision what could be some possible applications of this work and some future directions for disordered and nonlinear photonics. One of the main advantages of the bottom-up fabrication consists in the scalability of the production. However, most of the results presented here are hampered by the presence of the substrate. In fact, working with microspheres with effective refractive index smaller than 2, causes a lot of outcoupling in the substrate. Therefore one of the main challenges would be to decrease the refractive index of the substrate or to couple smartly selected modes in the spheres that would suffer less from the presence of the substrate (for example whispering gallery modes). In terms of fabrication of disordered and multiple scattering slabs, a big upgrade would be to fabricate thicker samples (both to increase the efficiency and, eventually, localization phenomena). Therefore our method has to be improved to become faster (now it requires a lot of hours for a  $5 \mu\text{m}$  thick sample). For the project of the microspheres of  $\text{TiO}_2$  with the nanodiamonds there are two clear possible improvements. One would be to measure smaller spheres to be able to see the Purcell effect, secondly, we could replace the NV centers with SiV to benefit from their narrow emission around the ZPL.

### 7.1.1 Disordered quantum sources

Noncentrosymmetric crystals, when illuminated with a pump beam, do not emit only SHG (which was the focus of this work), but also do spontaneous

parametric down-conversion (SPDC). This means that, similarly to the random quasi-phase-matching for the second-harmonic generation, the interference of the SPDC from a disordered crystals should emit a detectable signal. In my opinion, this hypothesis should be tested first in non-scattering disordered crystals, because the scattering introduces another layer of complication in this already intricate problem. This measurement (that we attempted but failed), has to fight with a very low efficiency of the SPDC that can be easily overtaken by fluorescence from impurities in the sample.

### 7.1.2 Nonlinear generation and localization

The long-lasting problem of 3D Anderson localization has been proven to be very elusive in the last decades. What can be added more on such a topic? In my opinion our nonlinear disordered photonic media can present some unexplored advantages. First of all, as is shown in Table 5.1, the inverse scattering efficiency of our LiNbO<sub>3</sub> slabs is short and it could present interesting values of  $kl^* \approx 1$  in the blue part of the spectrum. This would still be within the bandgap of LiNbO<sub>3</sub>, preventing in theory undesired subbandgap absorption. Moreover, the SHG can be used as a probe of the diffusive/localizing nature of a sample, given that the scattering strength of the material is heavily wavelength dependent [85].

### 7.1.3 Nonlinear generation and wavefront shaping

Wavefront shaping has proven to be a fertile field of research. The possibility to control the phase and the amplitude of a light profile can be used in many applications, from bioimaging to optical computing. On contrary, the wavefront shaping combined with the second-harmonic generation in multiple scattering and nonlinear materials is hardly explored. There is a practical reason for that, given that it requires the combination of nonlinear disordered crystals, spatial light modulators (SLMs) and pulsed lasers. However, on a practical standpoint the cross-contamination between these field can be very promising. First of all, wavefront shaping would be the primary tool to investigate the nonlinear generation in NDPM. Little is known, in fact, if and how transfer matrix theory can be applied to the nonlinear case. Secondly, with wavefront shaping it is possible to modify the emission pattern from a NDPM, converting a SHG speckle into a focal point or more complicated images [30]. This approach could be further used to increase the efficiency of the random quasi-phase-matching towards and "optimal" RQPM. The possibilities are actually broader. An SLM and a complex material can be used to perform optical calculation tasks such as random linear projections [36]. If the medium is nonlinear, it enables a host of possible optical computing operations, such as reservoir computing [38] or extreme machine learning [37]. Most of the works in these fields rely on nonlinearities in fibers or in waveguides, but no one so far harnessed the potential of fully nonlinear and disordered materials.

## Appendix A

# Modeling of random quasi-phase-matching

The vectorial model presented in this appendix is illustrated in depth in [143]. This model simulates the SHG in transparent media composed by an arbitrary configuration of crystalline domains. The problem is reduced to a one-dimensional calculation by dividing the three-dimensional structure in one-dimensional sticks and computing the SHG in each stick individually, as depicted in Fig. A.1a. This is similar to other models presented in literature [139, 149, 183]. In Fig. A.1b a single stick is shown. Each domain has a random orientation and a random size chosen from a Gaussian distribution. The second-harmonic field generated by each domain is computed analytically and added in phase with the SHG from all the domains in the stick. The result of this interference can be represented in the SHG complex plane reported in Fig A.1c. The incoming beam is defined as the plane wave

$$E(\omega) = (\hat{\mathbf{e}}^a e^{i\phi_a} \cos \beta + \hat{\mathbf{e}}^b e^{i\phi_b} \sin \beta) E_\omega e^{i(kc - \omega t)}$$

with amplitude  $E_\omega$ , frequency  $\omega$ , wavevector  $k$ , the starting phases  $\phi_a$  and  $\phi_b$ , and a polarization angle  $\beta$  in the lab frame. The vectors  $\hat{\mathbf{e}}^a$  and  $\hat{\mathbf{e}}^b$  are the unit vectors along the  $a$  and  $b$  axes. At the beginning of each domain, the electric fields in the lab frame  $E_{\text{lab}}$ , are transformed into the reference frame of the respective crystal  $E_{\text{cry}} = R \cdot E_{\text{lab}}$  (see Fig. A.1d). The domain orientation is defined by the rotation between the laboratory frame and the crystal frame as shown in Fig. A.1e. The beams are decomposed into their components along the  $o$  and  $e$  axes and each polarization combination of the pump ( $oo, eo, oe, ee$ ) generates a second-harmonic field  $E_{\text{gen}}^u(2\omega, X_n)$  along  $u \in \{o, e\}$ . At the end of the  $n^{\text{th}}$  single grain the field is given according to:

$$E_{\text{gen}}^u(2\omega, X_n) = \sum_{v,w} \frac{i(2\omega)^2}{2\epsilon_0 c^2 k_3^u} P^{u,vw} \left( \frac{e^{i\Delta k^{u,vw} X_n} - 1}{i\Delta k^{u,vw}} \right) e^{ik_3^u X_n} \quad (\text{A.1})$$

with the phase mismatch  $\Delta k^{u,vw} = k^v(\omega) + k^w(\omega) - k^u(2\omega)$ , the wave vector  $k_3^u$  of the second-harmonic along  $u$ , and  $P^{u,vw} = \langle \hat{\mathbf{e}}^u, P^{vw} \rangle$  the second-harmonic polarization along  $v, w \in \{o, e\}$  projected onto the  $o/e$ -axis ( $\hat{\mathbf{e}}^u$  unit vector along  $u \in \{o, e\}$ ), where  $P_i^{vw} = 2\epsilon_0 \sum_{jk} d_{ijk} E_j^v E_k^w$ . Further details are given in the supplementary information of [143].

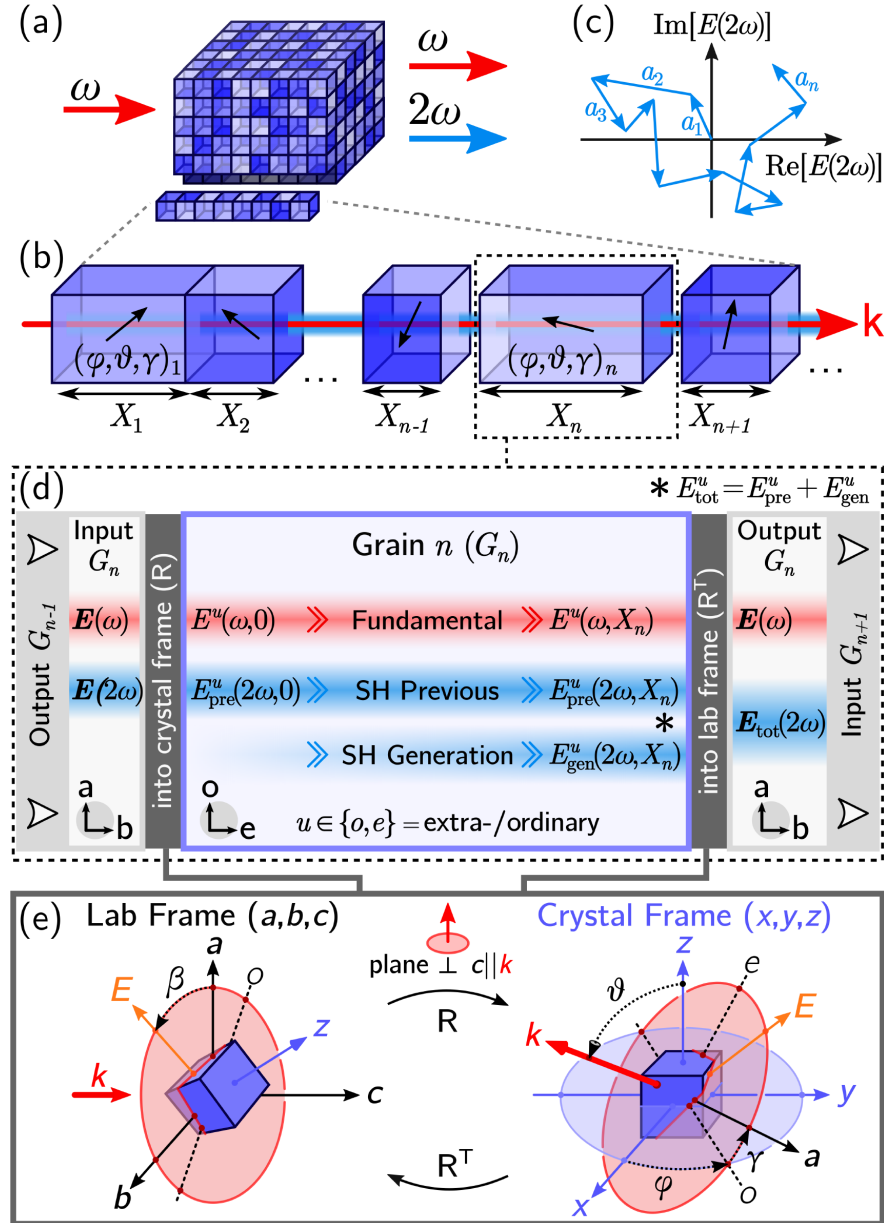


FIGURE A.1: a) Sketch of a disordered assembly of  $\chi^{(2)}$  domains composed by parallel sticks. b) Each stick is formed by domains of different size  $X_n$  and different orientation, represented by the arrows and the Euler angles. c) Representation of the SHG generated by each domain in a stick, in the complex plane. Each domain produces a phasor in the plane, each stick is a different random walk. d) Sketch of the angles between the crystal frame and the laboratory frame.  $\beta$  represents the polarization of the input beam. The ordinary axis is indicated with  $o$  and the extraordinary with  $e$ . e) Illustration of the propagation, generation and interference of the beams. Image taken from [143].

The pump and the SHG propagated in the domains take into consideration for each step the amplitude, the polarization and the phase of both the beams. Scattering in grain-to-grain propagation is neglected as well as walk-off angle of the generated SHG. In this model it is possible to replace the random distribution of the domains with specific orientations, such that it can be used to calculate bulk quasi-phase-matching, or perfect phase-matching. Moreover, it can be applied to any nonlinear crystal once the  $\chi^{(2)}$  tensor is provided. The output of the calculation is a nonlinear speckle pattern in which every speckle grain is generated by a single stick (in this simplified model one pixel corresponds to one speckle grain). At this moment there is no mixing between the sticks, therefore, this model is applicable only to transparent or weakly scattering materials.

One possible application of this code, to illustrate its working principle, is to study the dependency of the SHG on the input polarization. In Fig. A.2a we see the SHG speckle produced for different input polarizations from a 10x10x10 cuboids (i.e. 100 sticks in parallel, each of them composed by 10 domains). As expected, some speckle grains change heavily with the input polarization and some are not very affected. In Fig. A.2b,e there is a schematic of a 4x4x4 cuboid, to show how the model works. A single stick can have a strong polar dependency (as represented in Fig. A.2c), while many sticks in parallel have a more isotropic response as in Fig. A.2d. The polar dependency is obtained adding the contribution of all the sticks. Interestingly, in this model the thickness does not contribute on average on the polar dependency. This is shown in Fig. A.2f, where we can see that thicker cuboids (i.e. longer assemblies in the direction of the propagation of the fundamental beam) do not modify the polar dependency of the RQPM SHG.



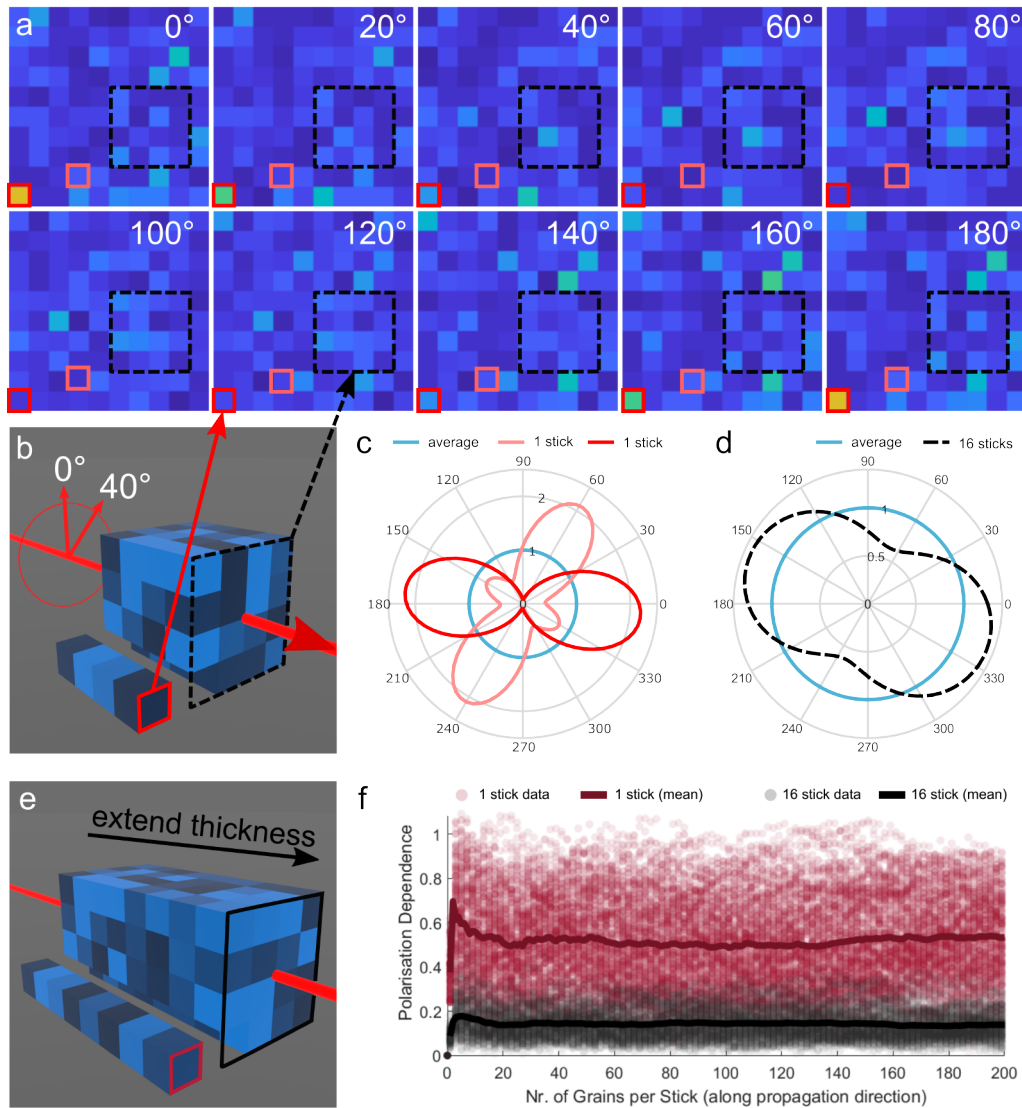


FIGURE A.2: Simulation of the polarization dependence of the random quasi-phase-matched SHG in a transparent disordered material. a) Nonlinear speckle pattern for for different input polarizations. b) Sketch of a  $4 \times 4 \times 4$  cube. c) Polar plot obtained for two different sticks of four domains. d) Polar plot obtained integrating over the speckle of the  $4 \times 4$  sticks, with a weaker polar dependence. e) Sketch of a  $4 \times 4 \times 8$  cuboid, composed by 16 sticks of length 8 domains. f) Simulation of cuboids of different length along the beam propagation. The solid lines are the average over 100 realization of disorder per different length. We can see that the polar dependence is not affected by the length of the disordered crystal in the direction of propagation of the fundamental beam. Image realized by J. Müller.

# Publications related to this dissertation

Articles in peer-reviewed journals:

- Romolo Savo, **Andrea Morandi**, Jolanda S. Müller, Fabian Kaufmann, Flavia Timpu, Marc Reig Escalé, Michele Zanini, Lucio Isa and Rachel Grange. "Broadband Mie driven random quasi-phase-matching". *Nature Photonics* (2020).
- Jolanda S. Müller, **Andrea Morandi**, Rachel Grange, and Romolo Savo. "Modeling of Random Quasi-Phase-Matching in Birefringent Disordered Media". *Physical Review Applied* (2021).
- **Andrea Morandi**, Romolo Savo, Jolanda S. Müller, Simeon Reichen and Rachel Grange. "Multiple Scattering and Random Quasi-Phase-Matching in Disordered Assemblies of LiNbO<sub>3</sub> Nanocubes". *ACS Photonics* (2022).
- Viola Valentina Vogler-Neuling, Artemios Karvounis,\* **Andrea Morandi**, Helena Weigand, Eric Dénervaud and Rachel Grange. "Photonic Assemblies of Randomly Oriented Nanocrystals for Engineered Nonlinear and Electro-Optic Effects". *ACS Photonics* (2022).

Selected participation to conferences:

- **Andrea Morandi**, Romolo Savo, Flavia Timpu and Rachel Grange. " $\chi(2)$  nanomaterials for complex assemblies and metasurfaces". *Fall PhD school 2018 on extreme electromagnetic matter interaction - EXEMI 2018*. Gif sur Yvette, France (2018). Poster.
- **Andrea Morandi**, Romolo Savo, Jolanda S. Müller, Fabian Kaufmann, Flavia Timpu, Marc Reig Escalé, Michele Zanini, Lucio Isa and Rachel Grange. "Random quasi-phase matching in bottom-up assemblies of nanoparticles into disordered microspheres" *Nanophotonics and micro/nano optics international conference - NANOP 2019*. Munich, Germany (2019). Contributed talk.
- **Andrea Morandi**, Romolo Savo, Jolanda S. Müller, Simeon Reichen and Rachel Grange. "Disordered LiNbO<sub>3</sub> assemblies for Second-Harmonic Generation in the multiple scattering regime". *Workshop on Complex Materials for Nonlinear Optics - CMNO 2020*. Zurich, Switzerland (2020). Poster.

- **Andrea Morandi**, Romolo Savo, Jolanda S. Müller, Simeon Reichen and Rachel Grange. "Multiple Scattering and Random Quasi-Phase-Matching in Disordered Assemblies of LiNbO<sub>3</sub> Nanocubes". *8th International Topical Meeting on Nanophotonics and Metamaterials - Nanometa 2022*. Seefeld im Tirol, Austria (2022). Poster.
- **Andrea Morandi**, Romolo Savo, Jolanda Simone Müller, Andrea Scheidegger, Paolo Fischer, Artemios Karvounis, Ngoc My Hanh Duoeng and Rachel Grange. "Linear and nonlinear photonics in bottom-up assemblies of nanoparticles". *12th International Conference on Metamaterials, Photonic Crystals and Plasmonics - META 2022*. Torremolinos, Spain (2022). Invited talk.

# Curriculum Vitae

**Name:** Andrea Morandi  
**Date of birth:** October 16, 1993 in Cremona, Italy  
**Place of birth:** Cremona, Italy  
Citizen of Italy

## *Education*

- 2018–2023** Ph.D. Candidate  
ETH Zürich, Switzerland  
Institute for Quantum Electronics,  
Optical Nanomaterial Group  
Prof. Dr. R. Grange  
*Current status:* Doctoral student
- 2015–2018** Master Degree in Physics - 110/110 cum Laude  
Univeristy of Pisa, Italy  
*Master thesis:* "Strain engineering of WS<sub>2</sub> with  
polimeric artificial micro-muscles"
- 2012–2015** Bachelor of Science in Physics - 108/110  
Univeristy of Pisa, Italy  
*Thesis:* "Quantum phenomena in  
conductance at the nanoscale"
- 2007–2012** High school degree - 100/100  
Liceo scientifico Aselli Cremona, Italy  
*Thesis:* "Spinoza's philosophy and string theory:  
the unification of the substance"



# Bibliography

- [1] P. A. Franken, A. E. Hill, C. W. Peters, and G. Weinreich, "Generation of optical harmonics", *Physical Review Letters*, vol. 7, no. 4, pp. 118–119, 1961, ISSN: 00319007. DOI: [10.1103/PhysRevLett.7.118](https://doi.org/10.1103/PhysRevLett.7.118).
- [2] T. Maiman, "Stimulated Optical Radiation in Ruby", *Nature*, no. 187, pp. 493–494, 1960.
- [3] G. Busch, "Early history of ferroelectricity", *Ferroelectrics*, vol. 74, no. 1, pp. 267–284, 1987, ISSN: 15635112. DOI: [10.1080/00150198708201307](https://doi.org/10.1080/00150198708201307).
- [4] J. G. Mayer, "Über Elementarakte mit zwei Quantenspruengen", *Annalen der Physik*, vol. Volume 401, no. 3, 1928.
- [5] A. Yariv and Y. Pochi, *Photonics. Optical electronics in modern communications*, 6th, O. U. Press, Ed. 2005.
- [6] E. Garmire, "Nonlinear optics in daily life", *Optics Express*, vol. 21, no. 25, p. 30 532, 2013, ISSN: 10944087. DOI: [10.1364/oe.21.030532](https://doi.org/10.1364/oe.21.030532).
- [7] J. L. O'Brien, A. Furusawa, and J. Vučković, "Photonic quantum technologies", *Nature Photonics*, vol. 3, no. 12, pp. 687–695, 2009, ISSN: 17494885. DOI: [10.1038/nphoton.2009.229](https://doi.org/10.1038/nphoton.2009.229). arXiv: [1003.3928](https://arxiv.org/abs/1003.3928).
- [8] M. Müller, S. Bounouar, K. D. Jöns, M. Glässl, and P. Michler, "On-demand generation of indistinguishable polarization-entangled photon pairs", *Nature Photonics*, vol. 8, no. 3, pp. 224–228, 2014, ISSN: 17494885. DOI: [10.1038/nphoton.2013.377](https://doi.org/10.1038/nphoton.2013.377). arXiv: [1308.4257](https://arxiv.org/abs/1308.4257).
- [9] Robert W. Boyd, *Nonlinear Optics*, 3rd. Elsevier, 2008, p. 613.
- [10] M. Houé and P. D. Townsend, "An introduction to methods of periodic poling for second-harmonic generation", *Journal of Physics D: Applied Physics*, vol. 28, no. 9, pp. 1747–1763, 1995, ISSN: 13616463. DOI: [10.1088/0022-3727/28/9/001](https://doi.org/10.1088/0022-3727/28/9/001).
- [11] A. A. Haim Suchowski, Barry D. Bruner and Y. Silberberg, "Frequency conversion", *OPN Optics Photonics News*, no. 9783662555439, pp. 165–227, 2018, ISSN: 18600840. DOI: [10.1007/978-3-662-55545-3\\_5](https://doi.org/10.1007/978-3-662-55545-3_5).
- [12] C. F. Bohren, "Absorption and scattering of light by small particles", *Absorption and scattering of light by small particles*, 1983, ISSN: 0031-9112. DOI: [10.1088/0031-9112/35/3/025](https://doi.org/10.1088/0031-9112/35/3/025).
- [13] L. Rayleigh, "On the transmission of light through an atmosphere containing small particles in suspension, and on the origin of the blue of the sky", *The London, Edinburgh, and Dublin Philosophical Magazine and Journal of Science*, vol. 47, no. 287, pp. 375–384, 1899, ISSN: 1941-5982. DOI: [10.1080/14786449908621276](https://doi.org/10.1080/14786449908621276).

- [14] D. S. Wiersma, "Disordered photonics", *Nature Photonics*, vol. 7, no. 3, pp. 188–196, 2013, ISSN: 17494885. DOI: [10.1038/nphoton.2013.29](https://doi.org/10.1038/nphoton.2013.29).
- [15] J. W. Goodman, "Some fundamental properties of speckle\*", *Journal of the Optical Society of America*, vol. 66, no. 11, p. 1145, 1976, ISSN: 0030-3941. DOI: [10.1364/josa.66.001145](https://doi.org/10.1364/josa.66.001145).
- [16] I. M. Vellekoop and A. P. Mosk, "Focusing coherent light through opaque strongly scattering media", *Optics Letters*, vol. 32, no. 16, p. 2309, 2007, ISSN: 0146-9592. DOI: [10.1364/ol.32.002309](https://doi.org/10.1364/ol.32.002309).
- [17] S. Popoff, G. Lerosey, M. Fink, A. C. Boccara, and S. Gigan, "Image transmission through an opaque material", *Nature Communications*, vol. 1, no. 6, pp. 6–10, 2010, ISSN: 20411723. DOI: [10.1038/ncomms1078](https://doi.org/10.1038/ncomms1078). arXiv: [1005.0532](https://arxiv.org/abs/1005.0532).
- [18] O. Katz, E. Small, and Y. Silberberg, "Looking around corners and through thin turbid layers in real time with scattered incoherent light", *Nature Photonics*, vol. 6, no. 8, pp. 549–553, 2012, ISSN: 17494885. DOI: [10.1038/nphoton.2012.150](https://doi.org/10.1038/nphoton.2012.150).
- [19] C. Moretti and S. Gigan, "Readout of fluorescence functional signals through highly scattering tissue", *Nature Photonics*, vol. 14, no. 6, pp. 361–364, 2020, ISSN: 17494893. DOI: [10.1038/s41566-020-0612-2](https://doi.org/10.1038/s41566-020-0612-2). arXiv: [1906.02604](https://arxiv.org/abs/1906.02604). [Online]. Available: <http://dx.doi.org/10.1038/s41566-020-0612-2>.
- [20] A. P. Mosk, A. Lagendijk, G. Lerosey, and M. Fink, "Controlling waves in space and time for imaging and focusing in complex media", *Nature Photonics*, vol. 6, no. 5, pp. 283–292, 2012, ISSN: 17494885. DOI: [10.1038/nphoton.2012.88](https://doi.org/10.1038/nphoton.2012.88).
- [21] E. S. Goerlitzer, R. N. Klupp Taylor, and N. Vogel, "Bioinspired Photonic Pigments from Colloidal Self-Assembly", *Advanced Materials*, vol. 30, no. 28, pp. 1–15, 2018, ISSN: 15214095. DOI: [10.1002/adma.201706654](https://doi.org/10.1002/adma.201706654).
- [22] G. Jacucci, S. Vignolini, and L. Schertel, "The limitations of extending nature's color palette in correlated, disordered systems", *Proceedings of the National Academy of Sciences of the United States of America*, vol. 117, no. 38, pp. 23 345–23 349, 2020, ISSN: 10916490. DOI: [10.1073/pnas.2010486117](https://doi.org/10.1073/pnas.2010486117).
- [23] H. Cao, Y. G. Zhao, S. T. Ho, E. W. Seelig, Q. H. Wang, and R. P. Chang, "Random laser action in semiconductor powder", *Physical Review Letters*, vol. 82, no. 11, pp. 2278–2281, 1999, ISSN: 10797114. DOI: [10.1103/PhysRevLett.82.2278](https://doi.org/10.1103/PhysRevLett.82.2278).
- [24] R. Sapienza, "Controlling random lasing action", *Nature Physics*, vol. 18, no. 9, pp. 976–979, 2022, ISSN: 17452481. DOI: [10.1038/s41567-022-01655-3](https://doi.org/10.1038/s41567-022-01655-3).
- [25] M. Segev, Y. Silberberg, and D. N. Christodoulides, "Anderson localization of light", *Nature Photonics*, vol. 7, no. 3, pp. 197–204, 2013, ISSN: 17494885. DOI: [10.1038/nphoton.2013.30](https://doi.org/10.1038/nphoton.2013.30).

- [26] D. S. Wiersma, P. Bartolini, A. Lagendijk, and R. Righini, "Localization of light in a disordered medium", *Nature*, vol. 390, no. 6661, pp. 671–673, 1997, ISSN: 00280836. DOI: [10.1038/37757](https://doi.org/10.1038/37757).
- [27] D. Jović and C. Denz, "Disorder-induced localization of light in one- and two-dimensional photonic lattices", *Physica Scripta*, no. T149, 2012, ISSN: 00318949. DOI: [10.1088/0031-8949/2012/T149/014042](https://doi.org/10.1088/0031-8949/2012/T149/014042).
- [28] S. E. Skipetrov and J. H. Page, "Red light for Anderson localization", *New Journal of Physics*, vol. 18, no. 2, pp. 13–15, 2016, ISSN: 13672630. DOI: [10.1088/1367-2630/18/2/021001](https://doi.org/10.1088/1367-2630/18/2/021001). arXiv: [1601.07848](https://arxiv.org/abs/1601.07848).
- [29] T. Sperling, L. Schertel, M. Ackermann, G. J. Aubry, C. M. Aegerter, and G. Maret, "Can 3D light localization be reached in 'white paint'?", *New Journal of Physics*, vol. 18, no. 1, 2016, ISSN: 13672630. DOI: [10.1088/1367-2630/18/1/013039](https://doi.org/10.1088/1367-2630/18/1/013039). arXiv: [1510.08092](https://arxiv.org/abs/1510.08092).
- [30] Y. Qiao, X. Chen, Y. Peng, and Y. Zheng, "Second-harmonic focusing by nonlinear turbid medium via feedback-based wavefront shaping", *2017 Conference on Lasers and Electro-Optics, CLEO 2017 - Proceedings*, vol. 2017-Janua, no. 10, pp. 1–2, 2017, ISSN: 0146-9592. DOI: [10.1364/OL.42.001895](https://doi.org/10.1364/OL.42.001895). arXiv: [1612.00566](https://arxiv.org/abs/1612.00566).
- [31] Y. Qiao, F. Ye, Y. Zheng, and X. Chen, "Cavity-enhanced second-harmonic generation in strongly scattering nonlinear media", *Physical Review A*, vol. 99, no. 4, p. 43 844, 2019, ISSN: 24699934. DOI: [10.1103/PhysRevA.99.043844](https://doi.org/10.1103/PhysRevA.99.043844). [Online]. Available: <https://doi.org/10.1103/PhysRevA.99.043844>.
- [32] R. Samanta and S. Mujumdar, "Intensity-dependent speckle contrast of second harmonic light in a nonlinear disordered medium", *Applied Optics*, vol. 59, no. 36, p. 11 266, 2020, ISSN: 1559-128X. DOI: [10.1364/ao.411505](https://doi.org/10.1364/ao.411505).
- [33] R. Samanta, R. Pierrat, R. Carminati, and S. Mujumdar, "Speckle decorrelation in fundamental and second-harmonic light scattered from nonlinear disorder", *Physical Review Applied*, vol. 10, no. 1, p. 1, 2021, ISSN: 23317019. DOI: [10.1103/PhysRevApplied.18.054047](https://doi.org/10.1103/PhysRevApplied.18.054047). arXiv: [2107.08736](https://arxiv.org/abs/2107.08736). [Online]. Available: <http://arxiv.org/abs/2107.08736>.
- [34] O. Sánchez-Dena, Z. Behel, E. Salmon, *et al.*, "Polarization-resolved second harmonic generation from LiNbO<sub>3</sub> powders", *Optical Materials*, vol. 107, no. July, pp. 1–6, 2020, ISSN: 09253467. DOI: [10.1016/j.optmat.2020.110169](https://doi.org/10.1016/j.optmat.2020.110169).
- [35] M. Mascheck, S. Schmidt, M. Silies, *et al.*, "Observing the localization of light in space and time by ultrafast second-harmonic microscopy", *Nature Photonics*, vol. 6, no. 5, pp. 293–298, 2012, ISSN: 17494885. DOI: [10.1038/nphoton.2012.69](https://doi.org/10.1038/nphoton.2012.69).
- [36] A Saade, F Caltagirone, I Carron, *et al.*, "Random projections through multiple optical scattering: approximating kernels at the speed of light", *Icassp 2016*, pp. 6215–6219, 2016.



- [37] U. Teğın, M. Yıldırım, I. Oğuz, C. Moser, and D. Psaltis, “Scalable optical learning operator”, *Nature Computational Science*, vol. 1, no. 8, pp. 542–549, 2021, ISSN: 26628457. DOI: [10.1038/s43588-021-00112-0](https://doi.org/10.1038/s43588-021-00112-0). arXiv: [2012.12404](https://arxiv.org/abs/2012.12404).
- [38] M. Yıldırım, I. Oğuz, F. Kaufmann, *et al.*, “Nonlinear Optical Data Transformer for Machine Learning”, no. Mvm, 2022. arXiv: [2208.09398](https://arxiv.org/abs/2208.09398). [Online]. Available: <http://arxiv.org/abs/2208.09398>.
- [39] M. Baudrier-Raybaut, R. Haïdar, P. Kupecek, P. Lemasson, and E. Rosencher, “Random quasi-phase-matching in bulk polycrystalline isotropic nonlinear materials”, *Nature*, vol. 432, no. 7015, pp. 374–376, 2004, ISSN: 00280836. DOI: [10.1038/nature03027](https://doi.org/10.1038/nature03027).
- [40] S. Vasilyev, I. Moskalev, M. Mirov, V. Smolski, S. Mirov, and V. Gapontsev, “Mid-IR Kerr-lens mode-locked polycrystalline Cr:ZnS and Cr:ZnSe lasers with intracavity frequency conversion via random quasi-phase-matching”, *Nonlinear Frequency Generation and Conversion: Materials, Devices, and Applications XV*, vol. 9731, no. March 2016, 97310B, 2016, ISSN: 1996756X. DOI: [10.1117/12.2218356](https://doi.org/10.1117/12.2218356).
- [41] Q. Ru, N. Lee, X. Chen, *et al.*, “Optical parametric oscillation in random polycrystalline  $\chi(2)$  medium”, *RAPID 2018 - 2018 IEEE Research and Applications of Photonics In Defense Conference*, vol. 4, no. 6, pp. 71–72, 2018. DOI: [10.1109/RAPID.2018.8508926](https://doi.org/10.1109/RAPID.2018.8508926).
- [42] G. Mie, “Contribution to the optics of turbid media, particularly of colloidal metal solutions”, *Annalen der Physik*, vol. IV, no. 25, 1908.
- [43] L. Rayleigh, “On the electromagnetic theory of light”, *The London, Edinburgh, and Dublin Philosophical Magazine and Journal of Science*, vol. 12, no. 73, pp. 81–101, 1881, ISSN: 1941-5982. DOI: [10.1080/14786448108627074](https://doi.org/10.1080/14786448108627074).
- [44] James Clerk Maxwell, *A dynamical theory of the electromagnetic field*. Royal Society, 1865, vol. 119, pp. 125–127. DOI: [10.1038/119125a0](https://doi.org/10.1038/119125a0).
- [45] C. Mätzler, “MATLAB Functions for Mie Scattering and Absorption”, *IAP Res Rep*, vol. 2002-08, no. July 2002, pp. 1139–1151, 2002, ISSN: 03060012. DOI: [10.1039/b811392k](https://doi.org/10.1039/b811392k). arXiv: [arXiv:1011.1669v3](https://arxiv.org/abs/1011.1669v3). [Online]. Available: [http://arcc.ou.edu/~sim\\$rockee/NRA\\_2007\\_website/Mie-scattering-Matlab.pdf](http://arcc.ou.edu/~sim$rockee/NRA_2007_website/Mie-scattering-Matlab.pdf).
- [46] L. Brillouin, “The scattering cross section of spheres for electromagnetic waves”, *Journal of Applied Physics*, vol. 20, no. 11, pp. 1110–1125, 1949, ISSN: 00218979. DOI: [10.1063/1.1698280](https://doi.org/10.1063/1.1698280).
- [47] D. Tzarouchis and A. Sihvola, “Light scattering by a dielectric sphere: Perspectives on the Mie resonances”, *Applied Sciences (Switzerland)*, vol. 8, no. 2, 2018, ISSN: 20763417. DOI: [10.3390/app8020184](https://doi.org/10.3390/app8020184).
- [48] H Chew, “Dielectric Particles”, *Physical Review A*, vol. 38, no. 7, pp. 3410–3416, 1988.

- [49] A. I. Kuznetsov, A. E. Miroschnichenko, M. L. Brongersma, Y. S. Kivshar, and B. Luk'yanchuk, "Optically resonant dielectric nanostructures", *Science*, vol. 354, no. 6314, 2016, ISSN: 10959203. DOI: [10.1126/science.aag2472](https://doi.org/10.1126/science.aag2472).
- [50] K. Koshelev and Y. Kivshar, "Dielectric Resonant Metaphotonics", *ACS Photonics*, vol. 8, no. 1, pp. 102–112, 2021, ISSN: 23304022. DOI: [10.1021/acsp Photonics.0c01315](https://doi.org/10.1021/acsp Photonics.0c01315).
- [51] L. Rayleigh, "CXII. The problem of the whispering gallery", *The London, Edinburgh, and Dublin Philosophical Magazine and Journal of Science*, vol. 20, no. 120, pp. 1001–1004, 1910, ISSN: 1941-5982. DOI: [10.1080/14786441008636993](https://doi.org/10.1080/14786441008636993).
- [52] J. E. Heebner, "Nonlinear optical whispering gallery microresonators for photonics", p. 273, 2003.
- [53] I. Breunig, "Three-wave mixing in whispering gallery resonators", *Laser and Photonics Reviews*, vol. 10, no. 4, pp. 569–587, 2016, ISSN: 18638899. DOI: [10.1002/lpor.201600038](https://doi.org/10.1002/lpor.201600038).
- [54] C. S. Werner, K. Buse, and I. Breunig, "Continuous-wave whispering-gallery optical parametric oscillator for high-resolution spectroscopy", *Optics Letters*, vol. 40, no. 5, p. 772, 2015, ISSN: 0146-9592. DOI: [10.1364/ol.40.000772](https://doi.org/10.1364/ol.40.000772).
- [55] Y. E. Geints, A. A. Zemlyanov, and E. K. Panina, "Photonic jets from resonantly excited transparent dielectric microspheres", *Journal of the Optical Society of America B*, vol. 29, no. 4, p. 758, 2012, ISSN: 0740-3224. DOI: [10.1364/josab.29.000758](https://doi.org/10.1364/josab.29.000758).
- [56] B. S. Luk'yanchuk, R. Paniagua-Domínguez, I. Minin, O. Minin, and Z. Wang, "Refractive index less than two: photonic nanojets yesterday, today and tomorrow", *Optical Materials Express*, vol. 7, no. 6, p. 1820, 2017, ISSN: 2159-3930. DOI: [10.1364/ome.7.001820](https://doi.org/10.1364/ome.7.001820).
- [57] P. Ferrand, J. Wenger, A. Devilez, *et al.*, "Direct imaging of photonic nanojets", *Optics Express*, vol. 16, no. 10, p. 6930, 2008, ISSN: 1094-4087. DOI: [10.1364/oe.16.006930](https://doi.org/10.1364/oe.16.006930).
- [58] J. Zhu and L. L. Goddard, "All-dielectric concentration of electromagnetic fields at the nanoscale: The role of photonic nanojets", *Nanoscale Advances*, vol. 1, no. 12, pp. 4615–4643, 2019, ISSN: 25160230. DOI: [10.1039/c9na00430k](https://doi.org/10.1039/c9na00430k).
- [59] V. I. Ovod, "Modeling of multiple scattering from an ensemble of spheres in a laser beam", *Particle and Particle Systems Characterization*, vol. 16, no. 3, pp. 106–112, 1999, ISSN: 09340866. DOI: [10.1002/\(SICI\)1521-4117\(199908\)16:3<106::AID-PPSC106>3.0.CO;2-H](https://doi.org/10.1002/(SICI)1521-4117(199908)16:3<106::AID-PPSC106>3.0.CO;2-H).
- [60] P. Sheng, *Introduction to Wave Scattering, Localization, and Mesoscopic Phenomena*. Springer, 2009, ISBN: 9780521855129.
- [61] E. Akkermans and G. Montambaux, "Mesoscopic physics of electrons and photons", *Mesoscopic Physics of Electrons and Photons*, vol. 9780521855, no. January 2007, pp. 1–588, 2007. DOI: [10.1017/CB09780511618833](https://doi.org/10.1017/CB09780511618833).

- [62] P. Yazhgur, G. J. Aubry, L. S. Froufe-Pérez, and F. Scheffold, "Light scattering from colloidal aggregates on a hierarchy of length scales", *Optics Express*, vol. 29, no. 10, p. 14 367, 2021, ISSN: 10944087. DOI: [10.1364/oe.418735](https://doi.org/10.1364/oe.418735).
- [63] F. J. Schuurmans, D. Vanmaekelbergh, J. Van De Lagemaat, and A. Lagendijk, "Strongly photonic macroporous gallium phosphide networks", *Science*, vol. 284, no. 5411, pp. 141–143, 1999, ISSN: 00368075. DOI: [10.1126/science.284.5411.141](https://doi.org/10.1126/science.284.5411.141).
- [64] N. Curry, P. Bondareff, M. Leclercq, *et al.*, "Direct determination of diffusion properties of random media from speckle contrast", *Optics Letters*, vol. 36, no. 17, p. 3332, 2011, ISSN: 0146-9592. DOI: [10.1364/ol.36.003332](https://doi.org/10.1364/ol.36.003332). arXiv: [1104.5554](https://arxiv.org/abs/1104.5554).
- [65] F. Scheffold and I. D. Block, "Rapid high resolution imaging of diffusive properties in turbid media", *Optics Express*, vol. 20, no. 1, p. 192, 2012, ISSN: 10944087. DOI: [10.1364/oe.20.000192](https://doi.org/10.1364/oe.20.000192).
- [66] B. Bret, *Multiple light scattering in porous gallium phosphide*, ISBN: 9036521963.
- [67] R. Carminati, "Waves in Complex Media Lecture notes", 2018.
- [68] N. Garcia, A. Z. Genack, and A. A. Lisyansky, "Measurement of the transport mean free path of diffusing photons", *Physical Review B*, vol. 46, no. 22, pp. 14 475–14 479, 1992, ISSN: 01631829. DOI: [10.1103/PhysRevB.46.14475](https://doi.org/10.1103/PhysRevB.46.14475).
- [69] J Bertolotti, "Light transport beyond diffusion", *Tel.Ccsd.Cnrs.Fr*, no. December, p. 113, 2008. [Online]. Available: [papers://8c08a1ea-d2f3-4bbe-a32d-fa8464707ca3/Paper/p5122](https://papers://8c08a1ea-d2f3-4bbe-a32d-fa8464707ca3/Paper/p5122).
- [70] a. Einstein, "Über die von der molekularinetschen Theorie der Warme geforderte Bewegung vov in ruhenden Flussikeiten suspendierten Teilchen.", *Ann. d. Phys.*, vol. 322, no. 8, pp. 549–560, 1905. [Online]. Available: <http://onlinelibrary.wiley.com/doi/10.1002/andp.19053220806/abstract>.
- [71] F. Martelli, D. Contini, A. Taddeucci, and G. Zaccanti, "Photon migration through a turbid slab described by a model based on diffusion approximation II Comparison with Monte Carlo results", *Applied Optics*, vol. 36, no. 19, p. 4600, 1997, ISSN: 0003-6935. DOI: [10.1364/ao.36.004600](https://doi.org/10.1364/ao.36.004600).
- [72] F. Martelli, D. Contini, A. Taddeucci, and G. Zaccanti, "Photon migration through a turbid slab described by a model based on diffusion approximation II Comparison with Monte Carlo results", *Applied Optics*, vol. 36, no. 19, p. 4600, 1997, ISSN: 0003-6935. DOI: [10.1364/ao.36.004600](https://doi.org/10.1364/ao.36.004600).
- [73] R. Sapienza, P. D. García, J. Bertolotti, *et al.*, "Observation of resonant behavior in the energy velocity of diffused light", *Physical Review Letters*, vol. 99, no. 23, pp. 1–4, 2007, ISSN: 00319007. DOI: [10.1103/PhysRevLett.99.233902](https://doi.org/10.1103/PhysRevLett.99.233902).

- [74] T. G. Mayerhöfer, S. Pahlow, and J. Popp, “The Bouguer-Beer-Lambert Law: Shining Light on the Obscure”, *ChemPhysChem*, pp. 2029–2046, 2020, ISSN: 14397641. DOI: [10.1002/cphc.202000464](https://doi.org/10.1002/cphc.202000464).
- [75] K. M. Yoo, F. Liu, and R. R. Alfano, “When does the diffusion approximation fail to describe photon transport in random media?”, *Physical Review Letters*, vol. 64, no. 22, pp. 2647–2650, 1990, ISSN: 00319007. DOI: [10.1103/PhysRevLett.64.2647](https://doi.org/10.1103/PhysRevLett.64.2647).
- [76] P. E. Wolf and G. Maret, “Weak localization and coherent backscattering of photons in disordered media”, *Physical Review Letters*, vol. 55, no. 24, pp. 2696–2699, 1985, ISSN: 00319007. DOI: [10.1103/PhysRevLett.55.2696](https://doi.org/10.1103/PhysRevLett.55.2696).
- [77] G. Jacucci, J. Bertolotti, and S. Vignolini, “Role of Anisotropy and Refractive Index in Scattering and Whiteness Optimization”, *Advanced Optical Materials*, vol. 7, no. 23, 2019, ISSN: 21951071. DOI: [10.1002/adom.201900980](https://doi.org/10.1002/adom.201900980).
- [78] F. Cottier, A. Cipris, R. Bachelard, and R. Kaiser, “Microscopic and Macroscopic Signatures of 3D Anderson Localization of Light”, *Physical Review Letters*, vol. 123, no. 8, p. 83401, 2019, ISSN: 10797114. DOI: [10.1103/PhysRevLett.123.083401](https://doi.org/10.1103/PhysRevLett.123.083401). [Online]. Available: <https://doi.org/10.1103/PhysRevLett.123.083401>.
- [79] P. W. Anderson, “Absence of diffusion in certain random lattices”, *Career In Theoretical Physics, A (2nd Edition)*, vol. 386, no. 1949, pp. 80–93, 1958. DOI: [10.1142/9789812567154\\_0007](https://doi.org/10.1142/9789812567154_0007).
- [80] A. Lagendijk, B. Van Tiggelen, and D. S. Wiersma, “Fifty years of Anderson localization”, *Physics Today*, vol. 62, no. 8, pp. 24–29, 2009, ISSN: 00319228. DOI: [10.1063/1.3206091](https://doi.org/10.1063/1.3206091).
- [81] Y. Lahini, A. Avidan, F. Pozzi, *et al.*, “Anderson localization and non-linearity in one-dimensional disordered photonic lattices”, *Physical Review Letters*, vol. 100, no. 1, pp. 1–4, 2008, ISSN: 00319007. DOI: [10.1103/PhysRevLett.100.013906](https://doi.org/10.1103/PhysRevLett.100.013906). arXiv: [0704.3788](https://arxiv.org/abs/0704.3788).
- [82] T. Schwartz, G. Bartal, S. Fishman, and M. Segev, “Transport and Anderson localization in disordered two-dimensional photonic lattices”, *Nature*, vol. 446, no. 7131, pp. 52–55, 2007, ISSN: 14764687. DOI: [10.1038/nature05623](https://doi.org/10.1038/nature05623).
- [83] L. S. Froufe-Pérez, M. Engel, J. J. Sáenz, and F. Scheffold, “Band gap formation and Anderson localization in disordered photonic materials with structural correlations”, *Proceedings of the National Academy of Sciences of the United States of America*, vol. 114, no. 36, pp. 9570–9574, 2017, ISSN: 10916490. DOI: [10.1073/pnas.1705130114](https://doi.org/10.1073/pnas.1705130114).
- [84] D. S. Wiersma, P. Bartolini, J. Gómez Rivas, A. Lagendijk, and R. Righini, “Reply: Localization or classical diffusion of light?”, *Nature*, vol. 398, no. 6724, p. 181, 1999, ISSN: 00280836. DOI: [10.1038/18350](https://doi.org/10.1038/18350).

- [85] S. E. Skipetrov and I. M. Sokolov, "Intensity of Waves Inside a Strongly Disordered Medium", *Physical Review Letters*, vol. 123, no. 23, p. 233 903, 2019, ISSN: 10797114. DOI: [10.1103/PhysRevLett.123.233903](https://doi.org/10.1103/PhysRevLett.123.233903). arXiv: [1907.05299](https://arxiv.org/abs/1907.05299). [Online]. Available: <https://doi.org/10.1103/PhysRevLett.123.233903>.
- [86] J. Haberko, L. S. Froufe-Pérez, and F. Scheffold, "Transition from light diffusion to localization in three-dimensional amorphous dielectric networks near the band edge", *Nature Communications*, vol. 11, no. 1, pp. 1–9, 2020, ISSN: 20411723. DOI: [10.1038/s41467-020-18571-w](https://doi.org/10.1038/s41467-020-18571-w). arXiv: [1812.02095](https://arxiv.org/abs/1812.02095). [Online]. Available: <http://dx.doi.org/10.1038/s41467-020-18571-w>.
- [87] X. Zhang, Q. T. Cao, Z. Wang, *et al.*, "Symmetry-breaking-induced nonlinear optics at a microcavity surface", *Nature Photonics*, vol. 13, no. 1, pp. 21–24, 2019, ISSN: 17494893. DOI: [10.1038/s41566-018-0297-y](https://doi.org/10.1038/s41566-018-0297-y). [Online]. Available: <http://dx.doi.org/10.1038/s41566-018-0297-y>.
- [88] S. K. Kurtz and T. T. Perry, "6F-9 A Powder Technique for the Evaluation of Nonlinear Optical Materials", *IEEE Journal of Quantum Electronics*, vol. 4, no. 5, p. 333, 1968, ISSN: 15581713. DOI: [10.1109/JQE.1968.1075108](https://doi.org/10.1109/JQE.1968.1075108).
- [89] Y. Wong, C., Teng, "Handbook of Optical Constants of Solids II", *Academic Press*, pp. 149–152, 1991. DOI: [10.1109/VPWJ.2008.4762238](https://doi.org/10.1109/VPWJ.2008.4762238).
- [90] E. Palik, "Handbook of Optical Constants of Solids", *Handbook of Optical Constants of Solids*, vol. 527, pp. 345–354, 1998. DOI: [10.1016/b978-0-08-055630-7.50020-1](https://doi.org/10.1016/b978-0-08-055630-7.50020-1).
- [91] S. Saravi, T. Pertsch, and F. Setzpfandt, "Lithium Niobate on Insulator: An Emerging Platform for Integrated Quantum Photonics", *Advanced Optical Materials*, vol. 9, no. 22, 2021, ISSN: 21951071. DOI: [10.1002/adom.202100789](https://doi.org/10.1002/adom.202100789).
- [92] D. Zhu, L. Shao, M. Yu, *et al.*, "Integrated photonics on thin-film lithium niobate", *Advances in Optics and Photonics*, vol. 13, no. 2, p. 242, 2021, ISSN: 19438206. DOI: [10.1364/aop.411024](https://doi.org/10.1364/aop.411024). arXiv: [2102.11956](https://arxiv.org/abs/2102.11956).
- [93] S. Abel, F. Eltes, J. E. Ortmann, *et al.*, "Large Pockels effect in micro- and nanostructured barium titanate integrated on silicon", *Nature Materials*, vol. 18, no. 1, pp. 42–47, 2019, ISSN: 14764660. DOI: [10.1038/s41563-018-0208-0](https://doi.org/10.1038/s41563-018-0208-0). [Online]. Available: <http://dx.doi.org/10.1038/s41563-018-0208-0>.
- [94] F. Timpu, M. Reig Escalé, M. Timofeeva, *et al.*, "Enhanced Nonlinear Yield from Barium Titanate Metasurface Down to the Near Ultraviolet", *Advanced Optical Materials*, vol. 7, no. 22, pp. 1–9, 2019, ISSN: 21951071. DOI: [10.1002/adom.201900936](https://doi.org/10.1002/adom.201900936).
- [95] E.-i.-c. M. J. Weber, A. V. Dotsenko, L. B. Glebov, and V. A. Tsekhomsky, *Handbook of optical materials*. 2003, vol. 40, pp. 40–4668–40–4668, ISBN: 0849335124. DOI: [10.5860/choice.40-4668](https://doi.org/10.5860/choice.40-4668).

- [96] L. Arizmendi, "Photonic applications of lithium niobate crystals", *Physica Status Solidi (A) Applied Research*, vol. 201, no. 2, pp. 253–283, 2004, ISSN: 00318965. DOI: [10.1002/pssa.200303911](https://doi.org/10.1002/pssa.200303911).
- [97] A. Karvounis, F. Timpu, V. V. Vogler-Neuling, R. Savo, and R. Grange, "Barium Titanate Nanostructures and Thin Films for Photonics", *Advanced Optical Materials*, vol. 8, no. 24, pp. 1–23, 2020, ISSN: 21951071. DOI: [10.1002/adom.202001249](https://doi.org/10.1002/adom.202001249).
- [98] V. V. Vogler-neuling, "Nonlinear Photonic Crystals and Metasurfaces in Soft-Nanoimprinted Barium Titanate Nanomaterials", *PhD thesis, ETH*, no. 28058, 2021.
- [99] Flavia Claudia Timpu, "Linear and nonlinear optics with metal oxides: from single nanoparticles to metasurfaces", *PhD thesis, ETH*, 2019.
- [100] F. Timpu, J. Sendra, C. Renaut, *et al.*, "Lithium Niobate Nanocubes as Linear and Nonlinear Ultraviolet Mie Resonators", *ACS Photonics*, vol. 6, no. 2, pp. 545–552, 2019, ISSN: 23304022. DOI: [10.1021/acsp Photonics.8b01594](https://doi.org/10.1021/acsp Photonics.8b01594).
- [101] Y. Li, "Microspherical photonics: Giant resonant light forces, spectrally resolved optical manipulation, and coupled modes of microcavity arrays", 2015. arXiv: [1509.01306](https://arxiv.org/abs/1509.01306). [Online]. Available: <http://arxiv.org/abs/1509.01306>.
- [102] J. Kim, M. J. Serpe, and L. A. Lyon, "Hydrogel microparticles as dynamically tunable microlenses", *Journal of the American Chemical Society*, vol. 126, no. 31, pp. 9512–9513, 2004, ISSN: 00027863. DOI: [10.1021/ja047274x](https://doi.org/10.1021/ja047274x).
- [103] L. Song, S. Ahn, and D. R. Walt, "Fiber-optic microsphere-based arrays for multiplexed biological warfare agent detection", *Analytical Chemistry*, vol. 78, no. 4, pp. 1023–1033, 2006, ISSN: 00032700. DOI: [10.1021/ac051417w](https://doi.org/10.1021/ac051417w).
- [104] S. H. Kim, Y. S. Cho, S. J. Jeon, T. H. Eun, G. R. Yi, and S. M. Yang, "Microspheres with tunable refractive index by controlled assembly of nanoparticles", *Advanced Materials*, vol. 20, no. 17, pp. 3268–3273, 2008, ISSN: 09359648. DOI: [10.1002/adma.200702622](https://doi.org/10.1002/adma.200702622).
- [105] H. Pham-Van, C. Tran-Manh, B. Do-Danh, T. Nguyen-Minh, and H. Luc-Huy, "Evaporation-induced assembly of colloidal clusters into superclusters with nonconvex deltahedral geometry", *AIP Advances*, vol. 8, no. 12, 2018, ISSN: 21583226. DOI: [10.1063/1.5055638](https://doi.org/10.1063/1.5055638). [Online]. Available: <http://dx.doi.org/10.1063/1.5055638>.
- [106] R. Savo, A. Morandi, J. S. Müller, *et al.*, "Broadband Mie driven random quasi-phase-matching", *Nature Photonics*, vol. 14, no. 12, pp. 740–747, 2020, ISSN: 17494893. DOI: [10.1038/s41566-020-00701-x](https://doi.org/10.1038/s41566-020-00701-x). arXiv: [2005.12609](https://arxiv.org/abs/2005.12609). [Online]. Available: <http://dx.doi.org/10.1038/s41566-020-00701-x>.

- [107] N. Vogel, S. Utech, G. T. England, *et al.*, “Color from hierarchy: Diverse optical properties of micron-sized spherical colloidal assemblies”, *Proceedings of the National Academy of Sciences of the United States of America*, vol. 112, no. 35, pp. 10 845–10 850, 2015, ISSN: 10916490. DOI: [10.1073/pnas.1506272112](https://doi.org/10.1073/pnas.1506272112).
- [108] S. H. Kim, S. Y. Lee, G. R. Yi, D. J. Pine, and S. M. Yang, “Microwave-assisted self-organization of colloidal particles in confining aqueous droplets”, *Journal of the American Chemical Society*, vol. 128, no. 33, pp. 10 897–10 904, 2006, ISSN: 00027863. DOI: [10.1021/ja063528y](https://doi.org/10.1021/ja063528y).
- [109] J. L. Parsons and L. Rimai, “Raman spectrum of BaTiO<sub>3</sub>”, *Solid State Communications*, vol. 5, no. 5, pp. 423–427, 1967, ISSN: 00381098. DOI: [10.1016/0038-1098\(67\)90790-9](https://doi.org/10.1016/0038-1098(67)90790-9).
- [110] D. J. P. Vinothan N. Manoharan, Mark T. Elsesser, “Dense Packing and Symmetry in Small Clusters of Microspheres”, *Science*, vol. 30, no. 12, pp. 483–488, 2003, ISSN: 00948276. DOI: [10.1029/2003GL016875](https://doi.org/10.1029/2003GL016875).
- [111] Y. Yuan, L. Liu, Y. Zhuang, W. Jin, and S. Li, “Coupling effects of particle size and shape on improving the density of disordered polydisperse packings”, *Physical Review E*, vol. 98, no. 4, p. 42 903, 2018, ISSN: 24700053. DOI: [10.1103/PhysRevE.98.042903](https://doi.org/10.1103/PhysRevE.98.042903). [Online]. Available: <https://doi.org/10.1103/PhysRevE.98.042903>.
- [112] Z. Chen, A. Taflove, and V. Backman, “Highly efficient optical coupling and transport phenomena in chains of dielectric microspheres”, *Optics Letters*, vol. 31, no. 3, p. 389, 2006, ISSN: 0146-9592. DOI: [10.1364/ol.31.000389](https://doi.org/10.1364/ol.31.000389).
- [113] A. Morandi, R. Savo, J. S. Müller, S. Reichen, and R. Grange, “Multiple Scattering and Random Quasi-Phase-Matching in Disordered Assemblies of LiNbO<sub>3</sub>Nanocubes”, *ACS Photonics*, vol. 9, no. 6, pp. 1882–1888, 2022, ISSN: 23304022. DOI: [10.1021/acsp Photonics.2c00210](https://doi.org/10.1021/acsp Photonics.2c00210).
- [114] I. Aharonovich and E. Neu, “Diamond nanophotonics”, *Advanced Optical Materials*, vol. 2, no. 10, pp. 911–928, 2014, ISSN: 21951071. DOI: [10.1002/adom.201400189](https://doi.org/10.1002/adom.201400189).
- [115] M. Radulaski, J. L. Zhang, Y. K. Tzeng, *et al.*, “Nanodiamond Integration with Photonic Devices”, *Laser and Photonics Reviews*, vol. 13, no. 8, pp. 1–14, 2019, ISSN: 18638899. DOI: [10.1002/lpor.201800316](https://doi.org/10.1002/lpor.201800316). arXiv: [1610.03183](https://arxiv.org/abs/1610.03183).
- [116] R. D. Deegan, “Pattern formation in drying drops”, *Physical Review E - Statistical Physics, Plasmas, Fluids, and Related Interdisciplinary Topics*, vol. 61, no. 1, pp. 475–485, 2000, ISSN: 1063651X. DOI: [10.1103/PhysRevE.61.475](https://doi.org/10.1103/PhysRevE.61.475).
- [117] Y. F. Li, Y. J. Sheng, and H. K. Tsao, “Evaporation stains: Suppressing the coffee-ring effect by contact angle hysteresis”, *Langmuir*, vol. 29, no. 25, pp. 7802–7811, 2013, ISSN: 07437463. DOI: [10.1021/la400948e](https://doi.org/10.1021/la400948e).

- [118] D. Mampallil and H. B. Eral, "A review on suppression and utilization of the coffee-ring effect", *Advances in Colloid and Interface Science*, vol. 252, pp. 38–54, 2018, ISSN: 00018686. DOI: [10.1016/j.cis.2017.12.008](https://doi.org/10.1016/j.cis.2017.12.008). [Online]. Available: <https://doi.org/10.1016/j.cis.2017.12.008>.
- [119] N. Otsu, P. L. Smith, D. B. Reid, *et al.*, "Otsu<sub>1979</sub>tsu<sub>m</sub>method", *IEEE Transactions on Systems, Man, and Cybernetics*, vol. C, no. 1, pp. 62–66, 1979, ISSN: 0018-9472.
- [120] K. W. Desmond and E. R. Weeks, "Influence of particle size distribution on random close packing of spheres", *Physical Review E - Statistical, Nonlinear, and Soft Matter Physics*, vol. 90, no. 2, pp. 1–6, 2014, ISSN: 15502376. DOI: [10.1103/PhysRevE.90.022204](https://doi.org/10.1103/PhysRevE.90.022204).
- [121] L. Liu, Z. Li, Y. Jiao, and S. Li, "Maximally dense random packings of cubes and cuboids via a novel inverse packing method", *Soft Matter*, vol. 13, no. 4, pp. 748–757, 2017, ISSN: 17446848. DOI: [10.1039/c6sm02065h](https://doi.org/10.1039/c6sm02065h).
- [122] M. I. Mishchenko, J. M. Dlugach, M. A. Yurkin, *et al.*, "First-principles modeling of electromagnetic scattering by discrete and discretely heterogeneous random media", *Physics Reports*, vol. 632, pp. 1–75, 2016, ISSN: 03701573. DOI: [10.1016/j.physrep.2016.04.002](https://doi.org/10.1016/j.physrep.2016.04.002). [Online]. Available: <http://dx.doi.org/10.1016/j.physrep.2016.04.002>.
- [123] O. Zhuromskyy, "Applicability of effective medium approximations to modelling of mesocrystal optical properties", *Crystals*, vol. 7, no. 1, pp. 1–12, 2017, ISSN: 20734352. DOI: [10.3390/cryst7010001](https://doi.org/10.3390/cryst7010001).
- [124] N. V. Voshchinnikov, G. Videen, and T. Henning, "Effective medium theories for irregular fluffy structures: Aggregation of small particles", *Applied Optics*, vol. 46, no. 19, pp. 4065–4072, 2007, ISSN: 15394522. DOI: [10.1364/AO.46.004065](https://doi.org/10.1364/AO.46.004065).
- [125] V. A. Markel, "Introduction to the Maxwell Garnett approximation: tutorial", *Journal of the Optical Society of America A*, vol. 33, no. 7, p. 1244, 2016, ISSN: 1084-7529. DOI: [10.1364/josaa.33.001244](https://doi.org/10.1364/josaa.33.001244).
- [126] P. G. Kwiat, K. Mattle, H. Weinfurter, A. Zeilinger, A. V. Sergienko, and Y. Shih, "New high-intensity source of polarization-entangled photon pairs", *Physical Review Letters*, vol. 75, no. 24, pp. 4337–4341, 1995, ISSN: 00319007. DOI: [10.1103/PhysRevLett.75.4337](https://doi.org/10.1103/PhysRevLett.75.4337).
- [127] Y. Wang, X. Y. Zhou, Z. Chen, *et al.*, "Synthesis of cubic LiNbO<sub>3</sub> nanoparticles and their application in vitro bioimaging", *Applied Physics A: Materials Science and Processing*, vol. 117, no. 4, pp. 2121–2126, 2014, ISSN: 14320630. DOI: [10.1007/s00339-014-8630-x](https://doi.org/10.1007/s00339-014-8630-x).
- [128] G. Malkinson, P. Mahou, É. Chaudan, *et al.*, "Fast in Vivo Imaging of SHG Nanoprobes with Multiphoton Light-Sheet Microscopy", *ACS Photonics*, vol. 7, no. 4, pp. 1036–1049, 2020, ISSN: 23304022. DOI: [10.1021/acsp Photonics.9b01749](https://doi.org/10.1021/acsp Photonics.9b01749).



- [129] G. Marino, A. S. Solntsev, L. Xu, *et al.*, “Spontaneous photon-pair generation from a dielectric nanoantenna”, *Optica*, vol. 6, no. 11, p. 1416, 2019, ISSN: 2334-2536. DOI: [10.1364/optica.6.001416](https://doi.org/10.1364/optica.6.001416).
- [130] N. M. H. Duong, G. Saerens, F. Timpu, *et al.*, “Spontaneous parametric down-conversion in bottom-up grown lithium niobate microcubes”, *2022 Conference on Lasers and Electro-Optics, CLEO 2022 - Proceedings*, vol. 12, no. 9, pp. 3696–3704, 2022, ISSN: 21593930. DOI: [10.1364/ome.462981](https://doi.org/10.1364/ome.462981).
- [131] T. Santiago-Cruz, S. D. Gennaro, O. Mitrofanov, *et al.*, “Resonant metasurfaces for generating complex quantum states”, *Science*, vol. 377, no. 6609, pp. 991–995, 2022, ISSN: 10959203. DOI: [10.1126/science.abq8684](https://doi.org/10.1126/science.abq8684).
- [132] S. V. Rao, K. Moutzouris, and M. Ebrahimzadeh, “Nonlinear frequency conversion in semiconductor optical waveguides using birefringent, modal and quasi-phase-matching techniques”, *Journal of Optics A: Pure and Applied Optics*, vol. 6, no. 6, pp. 569–584, 2004, ISSN: 14644258. DOI: [10.1088/1464-4258/6/6/013](https://doi.org/10.1088/1464-4258/6/6/013).
- [133] C. Wang, C. Langrock, A. Marandi, *et al.*, “Ultrahigh-efficiency wavelength conversion in nanophotonic periodically poled lithium niobate waveguides”, *Optica*, vol. 5, no. 11, p. 1438, 2018, ISSN: 23342536. DOI: [10.1364/optica.5.001438](https://doi.org/10.1364/optica.5.001438).
- [134] R. Luo, “Highly tunable efficient second-harmonic generation in a lithium niobate nanophotonic waveguide”, *Optica*, vol. 5, no. 8, 2018.
- [135] S. Buckley, K. Rivoire, and J. Vuckovic, “Multiply resonant photonic crystal cavities for nonlinear frequency conversion”, *Optics InfoBase Conference Papers*, vol. 19, no. 22, pp. 22 198–22 207, 2012, ISSN: 21622701. DOI: [10.1364/oe.19.022198](https://doi.org/10.1364/oe.19.022198).
- [136] Y. Pu, R. Grange, C. L. Hsieh, and D. Psaltis, “Nonlinear optical properties of core-shell nanocavities for enhanced second-harmonic generation”, *Physical Review Letters*, vol. 104, no. 20, pp. 1–4, 2010, ISSN: 00319007. DOI: [10.1103/PhysRevLett.104.207402](https://doi.org/10.1103/PhysRevLett.104.207402).
- [137] F. Timpu, N. R. Hendricks, M. Petrov, *et al.*, “Enhanced Second-Harmonic Generation from Sequential Capillarity-Assisted Particle Assembly of Hybrid Nanodimers”, *Nano Letters*, vol. 17, no. 9, pp. 5381–5388, 2017, ISSN: 15306992. DOI: [10.1021/acs.nanolett.7b01940](https://doi.org/10.1021/acs.nanolett.7b01940).
- [138] E. Y. Morozov and A. S. Chirkin, “Stochastic quasi-phase matching in nonlinear-optical crystals with an irregular domain structure”, *Kvantovaya Elektronika*, vol. 34, no. 3, pp. 227–233, 2004, ISSN: 03687147. DOI: [10.1070/qe2004v034n03abeh002617](https://doi.org/10.1070/qe2004v034n03abeh002617).
- [139] X. Chen and R. Gaume, “Non-stoichiometric grain-growth in ZnSe ceramics for  $\chi(2)$  interaction”, *Optical Materials Express*, vol. 9, no. 2, p. 400, 2019, ISSN: 2159-3930. DOI: [10.1364/ome.9.000400](https://doi.org/10.1364/ome.9.000400).

- [140] J. Bravo-Abad, X. Vidal, J. L. Domínguez Juárez, and J. Martorell, "Optical second-harmonic scattering from a non-diffusive random distribution of nonlinear domains", *Optics Express*, vol. 18, no. 13, p. 14 202, 2010, ISSN: 1094-4087. DOI: [10.1364/oe.18.014202](https://doi.org/10.1364/oe.18.014202).
- [141] T. Ito and M. Tomita, "Speckle correlation measurement in a disordered medium observed through second-harmonics generation", *Physical Review E - Statistical, Nonlinear, and Soft Matter Physics*, vol. 69, no. 3 2, pp. 1–7, 2004, ISSN: 1063651X. DOI: [10.1103/PhysRevE.69.036610](https://doi.org/10.1103/PhysRevE.69.036610).
- [142] J. Zhang, E. Cassan, and X. Zhang, "Enhanced mid-to-near-infrared second harmonic generation in silicon-organic hybrid plasmonic microring resonators", *Optics InfoBase Conference Papers*, vol. 2, no. 5, pp. 143–149, 2014, ISSN: 21622701. DOI: [10.1364/cleo\\_at.2014.jth2a.46](https://doi.org/10.1364/cleo_at.2014.jth2a.46).
- [143] J. S. Müller, A. Morandi, R. Grange, and R. Savo, "Modeling of Random Quasi-Phase-Matching in Birefringent Disordered Media", *Physical Review Applied*, vol. 15, no. 6, p. 1, 2021, ISSN: 23317019. DOI: [10.1103/PhysRevApplied.15.064070](https://doi.org/10.1103/PhysRevApplied.15.064070). arXiv: [2011.10429](https://arxiv.org/abs/2011.10429). [Online]. Available: <https://doi.org/10.1103/PhysRevApplied.15.064070>.
- [144] E. Kim, A. Steinbrück, M. T. Buscaglia, *et al.*, "Second-Harmonic Generation of Single Diameter", *ACS Nano*, vol. 7, no. 6, pp. 5343–5349, 2013, ISSN: 1936-0851. [Online]. Available: <http://dx.doi.org/10.1021/nn401198g> <http://pubs.acs.org/doi/abs/10.1021/nn401198g>.
- [145] P. J. Campagnola and L. M. Loew, "Second-harmonic imaging microscopy for visualizing biomolecular arrays in cells, tissues and organisms", *Nature Biotechnology*, vol. 21, no. 11, pp. 1356–1360, 2003, ISSN: 10870156. DOI: [10.1038/nbt894](https://doi.org/10.1038/nbt894).
- [146] K. R. Campbell and P. J. Campagnola, "Assessing local stromal alterations in human ovarian cancer subtypes via second harmonic generation microscopy and analysis", *Journal of Biomedical Optics*, vol. 22, no. 11, p. 1, 2017, ISSN: 1560-2281. DOI: [10.1117/1.jbo.22.11.116008](https://doi.org/10.1117/1.jbo.22.11.116008).
- [147] K. B. Tilbury, K. R. Campbell, K. W. Eliceiri, S. M. Salih, M. Patankar, and P. J. Campagnola, "Stromal alterations in ovarian cancers via wavelength dependent Second Harmonic Generation microscopy and optical scattering", *BMC Cancer*, vol. 17, no. 1, pp. 1–11, 2017, ISSN: 14712407. DOI: [10.1186/s12885-017-3090-2](https://doi.org/10.1186/s12885-017-3090-2).
- [148] I. Aramburu, J. Ortega, C. L. Folcia, and J. Etxebarria, "Second harmonic generation by micropowders: A revision of the Kurtz-Perry method and its practical application", *Applied Physics B: Lasers and Optics*, vol. 116, no. 1, pp. 211–233, 2014, ISSN: 09462171. DOI: [10.1007/s00340-013-5678-9](https://doi.org/10.1007/s00340-013-5678-9).

- [149] T. Kawamori, Q. Ru, and K. L. Vodopyanov, “Comprehensive Model for Randomly Phase-Matched Frequency Conversion in Zinc-Blende Polycrystals and Experimental Results for ZnSe”, *Physical Review Applied*, vol. 11, no. 5, p. 1, 2019, ISSN: 23317019. DOI: [10.1103/PhysRevApplied.11.054015](https://doi.org/10.1103/PhysRevApplied.11.054015). [Online]. Available: <https://doi.org/10.1103/PhysRevApplied.11.054015>.
- [150] P. Barthelemy, J. Bertolotti, and D. S. Wiersma, “A Lévy flight for light”, *Nature*, vol. 453, no. 7194, pp. 495–498, 2008, ISSN: 14764687. DOI: [10.1038/nature06948](https://doi.org/10.1038/nature06948).
- [151] R. Savo, R. Pierrat, U. Najar, R. Carminati, S. Rotter, and S. Gigan, “Mean path length invariance in multiple light scattering”, *Science*, vol. 768, no. November, pp. 765–768, 2017, ISSN: 23318422. DOI: [10.1126/science.aan4054](https://doi.org/10.1126/science.aan4054). arXiv: [1703.07114](https://arxiv.org/abs/1703.07114).
- [152] D. S. Wiersma, “The physics and applications of random lasers”, *Nature Physics*, vol. 4, no. 5, pp. 359–367, 2008, ISSN: 17452481. DOI: [10.1038/nphys971](https://doi.org/10.1038/nphys971).
- [153] T. Van Der Beek, P. Barthelemy, P. M. Johnson, D. S. Wiersma, and A. Lagendijk, “Light transport through disordered layers of dense gallium arsenide submicron particles”, *Physical Review B - Condensed Matter and Materials Physics*, vol. 85, no. 11, pp. 1–11, 2012, ISSN: 10980121. DOI: [10.1103/PhysRevB.85.115401](https://doi.org/10.1103/PhysRevB.85.115401).
- [154] O. Sánchez-Dena, C. D. Fierro-Ruiz, S. D. Villalobos-Mendoza, D. M. C. Flores, J. T. Elizalde-Galindo, and R. Farías, “Lithium niobate single crystals and powders reviewed—part i”, *Crystals*, vol. 10, no. 11, pp. 1–32, 2020, ISSN: 20734352. DOI: [10.3390/cryst10110973](https://doi.org/10.3390/cryst10110973).
- [155] I. M. Tiginyanu, I. V. Kravetsky, J. Monecke, W. Cordts, G. Marowsky, and H. L. Hartnagel, “Semiconductor sieves as nonlinear optical materials”, *Applied Physics Letters*, vol. 77, no. 15, pp. 2415–2417, 2000, ISSN: 00036951. DOI: [10.1063/1.1316770](https://doi.org/10.1063/1.1316770).
- [156] V. A. Mel’nikov, L. A. Golovan, S. O. Konorov, *et al.*, “Second-harmonic generation in strongly scattering porous gallium phosphide”, *Applied Physics B: Lasers and Optics*, vol. 79, no. 2, pp. 225–228, 2004, ISSN: 09462171. DOI: [10.1007/s00340-004-1530-6](https://doi.org/10.1007/s00340-004-1530-6).
- [157] S. Faez, P. M. Johnson, D. A. Mazurenko, and A. Lagendijk, “Generation and Diffusion Inside Random Media”, vol. 26, no. 2, pp. 235–243, 2009.
- [158] E. V. Makeev and S. E. Skipetrov, “Second harmonic generation in suspensions of spherical particles”, *Optics Communications*, vol. 224, no. 1-3, pp. 139–147, 2003, ISSN: 00304018. DOI: [10.1016/S0030-4018\(03\)01756-5](https://doi.org/10.1016/S0030-4018(03)01756-5).
- [159] M. D. Torelli, N. A. Nunn, and O. A. Shenderova, “A Perspective on Fluorescent Nanodiamond Bioimaging”, *Small*, vol. 15, no. 48, pp. 1–20, 2019, ISSN: 16136829. DOI: [10.1002/smll.201902151](https://doi.org/10.1002/smll.201902151).

- [160] B. J. J. Hamlin and B. B. Zhou, "Extreme diamond-based quantum sensors", *Science*, vol. 366, no. 647, pp. 1312–1314, 2019.
- [161] N. Savage, "Quantum diamond sensors", *Nature*, vol. 591, no. 7851, S37, 2021, ISSN: 14764687. DOI: [10.1038/d41586-021-00742-4](https://doi.org/10.1038/d41586-021-00742-4).
- [162] J. L. O'Brien, "Optical quantum computing", *Science*, vol. 318, no. 5856, pp. 1567–1570, 2007, ISSN: 00368075. DOI: [10.1126/science.1142892](https://doi.org/10.1126/science.1142892). arXiv: [0803.1554](https://arxiv.org/abs/0803.1554).
- [163] H. R. Phillip and E. A. Taft, "Kramers-Kronig Analysis of Reflectance Data for Diamond", *Physical Review*, vol. 136, no. 5A, 1964, ISSN: 0031899X. DOI: [10.1103/PhysRev.136.A1445](https://doi.org/10.1103/PhysRev.136.A1445).
- [164] I. Aharonovich, A. D. Greentree, and S. Prawer, "Diamond photonics", *Nature Photonics*, vol. 5, no. 7, pp. 397–405, 2011, ISSN: 17494885. DOI: [10.1038/nphoton.2011.54](https://doi.org/10.1038/nphoton.2011.54).
- [165] G. Balasubramanian, P. Neumann, D. Twitchen, *et al.*, "Ultralong spin coherence time in isotopically engineered diamond", *Nature Materials*, vol. 8, no. 5, pp. 383–387, 2009, ISSN: 14764660. DOI: [10.1038/nmat2420](https://doi.org/10.1038/nmat2420).
- [166] L. Rondin, J. P. Tetienne, T. Hingant, J. F. Roch, P. Maletinsky, and V. Jacques, "Magnetometry with nitrogen-vacancy defects in diamond", *Reports on Progress in Physics*, vol. 77, no. 5, 2014, ISSN: 00344885. DOI: [10.1088/0034-4885/77/5/056503](https://doi.org/10.1088/0034-4885/77/5/056503). arXiv: [1311.5214](https://arxiv.org/abs/1311.5214).
- [167] T. D. Merson, S. Castelletto, I. Aharonovich, A. Turbic, T. J. Kilpatrick, and A. M. Turnley, "Nanodiamonds with silicon vacancy defects for nontoxic photostable fluorescent labeling of neural precursor cells", *Optics Letters*, vol. 38, no. 20, p. 4170, 2013, ISSN: 0146-9592. DOI: [10.1364/ol.38.004170](https://doi.org/10.1364/ol.38.004170).
- [168] C. Santori, P. E. Barclay, K. M. Fu, R. G. Beausoleil, S. Spillane, and M. Fisch, "Nanophotonics for quantum optics using nitrogen-vacancy centers in diamond", *Nanotechnology*, vol. 21, no. 27, 2010, ISSN: 09574484. DOI: [10.1088/0957-4484/21/27/274008](https://doi.org/10.1088/0957-4484/21/27/274008).
- [169] M. W. Doherty, N. B. Manson, P. Delaney, F. Jelezko, J. Wrachtrup, and L. C. Hollenberg, "The nitrogen-vacancy colour centre in diamond", *Physics Reports*, vol. 528, no. 1, pp. 1–45, 2013, ISSN: 03701573. DOI: [10.1016/j.physrep.2013.02.001](https://doi.org/10.1016/j.physrep.2013.02.001). arXiv: [1302.3288](https://arxiv.org/abs/1302.3288). [Online]. Available: <http://dx.doi.org/10.1016/j.physrep.2013.02.001>.
- [170] C. Kurtsiefer, S. Mayer, P. Zarda, and H. Weinfurter, "Stable solid-state source of single photons", *Physical Review Letters*, vol. 85, no. 2, pp. 290–293, 2000, ISSN: 00319007. DOI: [10.1103/PhysRevLett.85.290](https://doi.org/10.1103/PhysRevLett.85.290).
- [171] L. Novotny and Bert Hecht, *Principles of Nano-Optics*. Cambridge University Press, 2012, ISBN: 9780521832243. DOI: [10.1017/CB09780511813535](https://doi.org/10.1017/CB09780511813535).
- [172] A. F. Koenderink, "Single-Photon Nanoantennas", *ACS Photonics*, vol. 4, no. 4, pp. 710–722, 2017, ISSN: 23304022. DOI: [10.1021/acsp Photonics.7b00061](https://doi.org/10.1021/acsp Photonics.7b00061).

- [173] A. S. Zalogina, R. S. Savelev, E. V. Ushakova, *et al.*, “Purcell effect in active diamond nanoantennas”, *Nanoscale*, vol. 10, no. 18, pp. 8721–8727, 2018, ISSN: 20403372. DOI: [10.1039/c7nr07953b](https://doi.org/10.1039/c7nr07953b).
- [174] S. I. Bogdanov, M. Y. Shalaginov, A. S. Lagutchev, *et al.*, “Ultrabright Room-Temperature Sub-Nanosecond Emission from Single Nitrogen-Vacancy Centers Coupled to Nanopatch Antennas”, *Nano Letters*, vol. 18, no. 8, pp. 4837–4844, 2018, ISSN: 15306992. DOI: [10.1021/acs.nanolett.8b01415](https://doi.org/10.1021/acs.nanolett.8b01415).
- [175] D. V. Obydenov, D. A. Shilkin, E. I. Elyas, *et al.*, “Spontaneous Light Emission Assisted by Mie Resonances in Diamond Nanoparticles”, *Nano Letters*, vol. 21, no. 23, pp. 10 127–10 132, 2021, ISSN: 15306992. DOI: [10.1021/acs.nanolett.1c02616](https://doi.org/10.1021/acs.nanolett.1c02616).
- [176] S. Schietinger, T. Schröder, and O. Benson, “One-by-one coupling of single defect centers in nanodiamonds to high-Q modes of an optical microresonator”, *Nano Letters*, vol. 8, no. 11, pp. 3911–3915, 2008, ISSN: 15306984. DOI: [10.1021/nl8023627](https://doi.org/10.1021/nl8023627).
- [177] Y. M. Evtushenko, S. V. Romashkin, N. S. Trofimov, and T. K. Chekhlova, “Optical Properties of TiO<sub>2</sub> Thin Films”, *Physics Procedia*, vol. 73, pp. 100–107, 2015, ISSN: 18753892. DOI: [10.1016/j.phpro.2015.09.128](https://doi.org/10.1016/j.phpro.2015.09.128).
- [178] F. Zhang, R. J. Zhang, D. X. Zhang, *et al.*, “Temperature-dependent optical properties of titanium oxide thin films studied by spectroscopic ellipsometry”, *Applied Physics Express*, vol. 6, no. 12, 2013, ISSN: 18820778. DOI: [10.7567/APEX.6.121101](https://doi.org/10.7567/APEX.6.121101).
- [179] G. Boas, “Time-correlated single-photon counting on a chip”, *Biophotonics International*, vol. 14, no. 11, pp. 15–16, 2007, ISSN: 10818693.
- [180] H. Lami and E. Piémont, “Fluorescence decay analysis by iterative reconvolution based on the estimated covariance matrix”, *Chemical Physics*, vol. 163, no. 1, pp. 149–159, 1992, ISSN: 03010104. DOI: [10.1016/0301-0104\(92\)80148-0](https://doi.org/10.1016/0301-0104(92)80148-0).
- [181] S. J. Jeon, G. R. Yi, and S. M. Yang, “Cooperative assembly of block copolymers with deformable interfaces: Toward nanostructured particles”, *Advanced Materials*, vol. 20, no. 21, pp. 4103–4108, 2008, ISSN: 09359648. DOI: [10.1002/adma.200801377](https://doi.org/10.1002/adma.200801377).
- [182] V. V. Vogler-Neuling, A. Karvounis, A. Morandi, H. Weigand, E. Dénervaud, and R. Grange, “Photonic Assemblies of Randomly Oriented Nanocrystals for Engineered Nonlinear and Electro-Optic Effects”, *ACS Photonics*, vol. 9, no. 7, pp. 2193–2203, 2022, ISSN: 23304022. DOI: [10.1021/acsp Photonics.2c00081](https://doi.org/10.1021/acsp Photonics.2c00081).
- [183] X. Vidal and J. Martorell, “Generation of light in media with a random distribution of nonlinear domains”, *Physical Review Letters*, vol. 97, no. 1, pp. 1–4, 2006, ISSN: 00319007. DOI: [10.1103/PhysRevLett.97.013902](https://doi.org/10.1103/PhysRevLett.97.013902).